TÉCNICO LISBOA

Natural ventilation in office buildings – an experimental study of a reduced scale model

Océane Marie Gabrielle Hayot

Thesis to obtain the Master of Science Degree in

Mechanical Engineering

Supervisors: Prof. Pedro Jorge Martins Coelho
Dr. João Carlos Godinho Viegas

Examination Committee

Chairperson: Prof. Carlos Frederico Neves Bettencourt da Silva
Supervisor: Prof. Pedro Jorge Martins Coelho
Member of the Committee: Prof. António Luís Nobre Moreira
Dr. João Carlos Godinho Viegas

October 2019

Acknowledgements

First of all, I would like to express my gratitude to my supervisors Mr. João Viegas and Prof. Pedro Coelho. They have been very supportive, understanding and encouraging throughout the project. I would also like to thank Mr. Miguel Lança who created the reduced scale model. He was also very patient and available to answering my many questions, despite his personal work. The realization of this Master Thesis would not have been possible without their advice and guidance. They were all very present and helped me a lot to stay the course and to remove my doubts during the frequent meetings.

In addition, during the calibration process of my experimental equipment, I had to take the help and guidance of Mr. Luis Martins and Mr. Ricardo Mendes who deserve my deepest thanks for their patience and perseverance. More generally, I would like to acknowledge the LNEC for providing laboratory were the reduced scale model was set. I am also thankful to all the people working at LNEC for their warm welcome, especially Mrs. Francelina Lopes who helped me to print regularly my results, Mr. José Martins and Mr. Carlos Saldanha who were always there when I had doubts about the instrumentation, and Mrs. Ducle Franco for her kindness.

I also wanted to leave a huge word of gratitude and affection to my family and friends for their advices and endless support. To my mother, my deep thanks for her corrections, dedication and presence. Last but not least, a special thanks to Jules, unconditionally present every time I needed him.

Abstract

In Mediterranean climates, instead of using mechanical systems to cool the service buildings, a passive ventilation technique benefits from the fresh ambient air, during nighttime, to ventilate the offices and, thus, reduces their overall energy consumption. However, modern constructions are often equipped with decorative components, like the suspended ceilings (SCs), which are obstacles to the desired thermal exchange between the occupation zone and the slab.

This constructive solution, called Night Ventilation (NV), motivates the goal of the present thesis: to experimentally investigate the optimization of the use of a SC that does not totally cover the slab. More precisely, the problem is explored by running experiments in a reduced scale model of an office building, analyzing results for the heating and the cooling phases.

The results confirm that, as it was found in previous works, implementing SCs with peripheral gaps, in the reduced scale office, is an effective use of NV on reducing the next day temperature peak. The contribution of this thesis is the analysis of the cooling pattern in the model. Indeed, results indicate that the size of the peripheral gap between the side walls and the SC does not influence drastically the cooling pattern of the room. As a matter of fact, in all the tested configurations, the areas closer to the supply and exhaust air openings cool down faster than the others. However, it has been found that SCs with peripheral gaps induce a more homogenized cooling than the complete SC.

Key words: Natural Ventilation, Nocturnal free cooling, Suspended Ceiling, Thermal Comfort

Table of Contents

List of Figures

List of Tables

List of Acronyms

ACH	Air Change rate per Hour
ACS	Adaptive Comfort Standard
CCR	Ceiling Coverage Ratio
CFD	Computational Fluid Dynamics
CHTC	Convective Heat Transfer Coefficient
CP	Cooling Period
CRCP	Ceiling Radiant Cooling Panel
DCV	Diffuse Ceiling Ventilation
HP	Heating Period
HVAC	Heating, Ventilation and Air Conditioning
IAQ	Indoor Air Quality
IEQ	Indoor Environmental Quality
LNEC	Laboratório Nacional de Engenharia Civil
NV	Night Ventilation
O1	Opening above the SC
PMCs	Phase Change Materials
SC	Suspended Ceiling
TCs	Thermocouples
VPC	Vinyl Perforated Ceiling
XPS	Extruded Polystyrene

Nomenclature

Roman Characters

$\boldsymbol{A}$	Area of the slot cross section, ie., area of the cardboard duct	$[m^2]$
$\boldsymbol{D_H}$	Hydraulic diameter	$[m]$
$\boldsymbol{g}$	Gravitational acceleration	$[m^2/s]$
$\boldsymbol{Gr}$	Grashof number	[-]
$\boldsymbol{k}$	Thermal conductivity of the air	$[W/m.°C]$
$\boldsymbol{k}$	Coverage factor used to calculate expanded uncertainty	[-]
$\boldsymbol{\ell}$	Characteristic length	$[m]$
$\boldsymbol{L_x, L_y, L_z}$	Model dimensions in x, y and z directions	$[m]$
$\boldsymbol{l_y, l_z}$	Cardboard duct dimensions in y and z directions	$[m]$
$\boldsymbol{q'}$	Heat flux rate per unit length	$[W/m]$
$\boldsymbol{Q}$	Volumetric flow rate	$[m^3/s\,]$
$\boldsymbol{Re}$	Reynolds number	[-]
$\boldsymbol{r(a, b)}$	Correlation coefficient of a linear regression $y = ax + b$	[-]
$\boldsymbol{S^2(Q)}$	Experimental variance of the volumetric flow rate	$[m^6/s^2\,]$
$\boldsymbol{S^2(l_y), S^2(l_z)}$	Experimental variances of the cardboard duct dimensions	$[m^2]$
$\boldsymbol{S^2(A)}$	Experimental variance of the area of the cardboard duct	$[m^4]$
$\boldsymbol{S^2(a)}$	Experimental variance of the slope a	$[(m^3/h)^2/(m/s)^2]$
$\boldsymbol{S(a)}$	Standard-deviation of the slope a	$[(m^3/h)/(m/s)]$
$\boldsymbol{S^2(b)}$	Experimental variance of the intercept b	$[m^6/h^2]$
$\boldsymbol{S(b)}$	Standard-deviation of the intercept b	$[m^3/h]$
$\boldsymbol{T_{lab}}$	Laboratory temperature, i.e., ambient temperature	$[°C]$
$\boldsymbol{T_{TC}}$	Temperature read by a thermocouple	$[°C]$
$\boldsymbol{T_R}$	Temperature of the electrical resistance	$[°C]$
$\boldsymbol{U_{H95}}$	Expanded uncertainty[1] for the heat flux	$[W/m^2]$
$\boldsymbol{U_{P95}}$	Expanded uncertainty[1] for the electrical power	$[W]$

[1] Considering a 95% confidence interval.

$\boldsymbol{U_{Q95}}$	Expanded uncertainty[1] of the volumetric flow rate	$[m^3/h]$
$\boldsymbol{U_{T95}}$	Expanded uncertainty[1] for the temperature	$[°C]$
$\boldsymbol{U_{u_{ref}95}}$	Expanded uncertainty[1] for the air velocity	$[m/s]$
$\boldsymbol{u_c^2(Q)}$	Estimated variance of the volumetric flow rate	$[m^6/h^2]$
$\boldsymbol{u_c(Q)}$	Combined standard uncertainty for the volumetric flow rate	$[m^3/h]$
$\boldsymbol{u}$	Velocity component in x direction	$[m/s]$
$\boldsymbol{u_m}$	Mean air velocity at the supply and extraction slots	$[m/s]$
$\boldsymbol{u_Q}$	Velocity used to calculate Re	$[m/s]$
$\boldsymbol{u_{ref}}$	Velocity component in x direction measured in the reference point	$[m/s]$
$\boldsymbol{V}$	Volume of the reduced scale model	$[m^3]$

Greek Characters

$\boldsymbol{\beta}$	Thermal expansion coefficient	$[K^{-1}]$
ΔT	Temperature difference	$[°C]$
$\boldsymbol{\Delta\overline{T}_{HC}}$	Average temperature difference between heating and cooling periods	$[°C]$
$\boldsymbol{\vartheta}$	Kinematic viscosity	$[m^2/s]$
$\boldsymbol{\rho}$	Air density	$[kg/m^3]$

1. Introduction

1.1. Motivation

Since the energy crisis of the 70s, people are aware that the available resources are limited. Nowadays, the development of our societies and the growth of the population cause the world's energy demand to rise constantly and raise concerns over heavy environmental impacts [1]. The public awareness of this issue leads to the creation of conventions on climate change like the Kyoto Protocol where, in 1997, countries around the world agreed to cut in greenhouse-gas emissions [2].

Statistics from the work of Pérez-Lombard et al. [1] indicate that the global contribution from buildings accounts for a 20 to 40% of the total final energy consumption, surpassing the other major sectors, which are industry and transport. This is due to the increase of the time spent indoor, the necessity to satisfy the comfort levels, the enhancement of building services, mainly with the arrival of computers, and lighting needs. In Portugal, the energy share of buildings on national energy consumption balance is around 30% [3], which is less important than other European countries because the pleasant climatic conditions induce less needs of cooling or heating.

According to the Energy Information Administration in the United-States [4], among building services, space heating, ventilation and cooling represent more than 40% of the overall energy use in commercial buildings. This, along with rising cost of energy, results in the issue of reducing the energy consumption of buildings being, now, one of the main concerns of architects and building engineers. The challenge lies in maintaining satisfactory indoor air quality (IAQ) and thermal comfort for large space building in an energy efficient way [5].

Before going further, it is worthwhile giving a definition of thermal comfort. It is usually characterized by an ambient temperature between 18 and $25°C$ and a relative humidity between 30 and 60%. Solgi et al. [6] explain that people reaction to thermal indoor environment depends, of course, on the indoor environment (air temperature and velocity, relative humidity, etc.), but also on personal parameters such as metabolism, activity level and clothing. The most accepted definition of the term thermal comfort is the "the state of mind that expresses satisfaction with the thermal environment" [7]. Accordingly, the concept not only involves physiologic, but also subjective considerations. In other words, it varies from person to person. For that reason, it can be problematic to find a temperature satisfying all the room's occupants, and the temperature range suiting more people should be chosen. Zhai et al. [8] found that the acceptable thermal comfort range for natural ventilated buildings is larger than for buildings with standard mechanical heating, ventilation and air conditioning (HVAC) systems. This represents a significant advantage in favor of natural ventilation. However, the concept of thermal comfort presents several problems when translated into physical parameters. Al Horr et al. [7] recommend the use of four physical parameters, namely radiant

temperature, relative humidity, air temperature and velocity, which can be measured using sensors, with occupant survey to better understand their perception. In brief, as mentioned by Breesch and Janssens [9], thermal comfort is a suitable criterion to evaluate the performance of natural ventilation.

Through the media, people became more aware of the effect of the indoor environment on health and now know that building related sickness (BRS) and the sick building syndrome (SBS) exist [10]. Besides, the literature review made by Al Horr et al. [7] allows us to understand the relationship between indoor environmental quality (IEQ) and occupant productivity in office environment. Lots of studies about Green buildings and occupant productivity were publicized from 2000 to 2009. It is now a well-known fact that in addition to affecting occupants' health, indoor air quality influences the worker's performance in office tasks [11]. Despite the subjectivity of thermal comfort and the complexity to measure IAQ, Al Horr et al. [7] succeeded in identifying the main physical parameters in IAQ study: the ventilation rate, the indoor pollutant levels, and the outdoor air monitoring, thanks to occupant survey and other measurement methods, as already mentioned. To sum up, buildings occupants now expect good standards of IAQ and thermal comfort which implicates bringing fresh air to the occupants, and removing heat, gases and particles from the building.

1.2. State-of-the-Art

In order to find a solution to reduce the energy consumption of buildings, and more precisely the energy requirements of air-conditioning plants, while maintaining an acceptable indoor environment, many studies have been performed, in full and reduced-scale buildings, witnessing a growing consensus. This section will briefly review studies that were done in ventilation and are relevant to the present work.

In most cases, ventilation is seen as an efficient technique to guarantee the healthy condition of air in a low-cost way [12]. So, it appeared as a key component to undertake this challenge. The aim is to intentionally provide clean air to a space and remove indoor air. According to Zhigang [10], it is essential for meeting the metabolic needs of occupants and for diluting and removing pollutants emitted by indoor sources. It can be implemented using natural ventilation, mechanical ventilation, or hybrid ventilation, which is the combination of the first two methods. As the denominations suggest, natural ventilation is due to the wind flow through the building openings and due to buoyancy driven flows, caused by temperature differences between indoor and outdoor, whereas mechanical ventilation uses exhaust and (many times) supply fans to maintain a constant flow of clear outdoor air. The next paragraph details the natural ventilation phenomena, as it is used in the experiments of the present work.

1.2.1. Natural ventilation and thermal buoyancy

To begin with, an obvious advantage of natural ventilation is that it is a more economical solution than mechanical ventilation, since the latter system runs with electricity and requires additional maintenance, thus increasing the installation final cost. Consequently, as a sustainable, energy-efficient and clean technology that is well accepted by occupants, natural ventilation has been employed in many energy policies.

It is important to mention that the main driving force that causes natural ventilation through buildings is the pressure differential across the building envelope. Zhigang [10] explained in detail that these pressure differences are produced by two main effects, which are the action of thermally generated pressures and wind:

- Wind-induced ventilation

  The wind creates an overpressure at the windward side of the building and an underpressure at the leeward side and the parallel sides of the building. Consequently, it drives a flow through the openings in the building envelope.

- Buoyancy-induced ventilation

  In a buoyancy driven flow, the pressure differences are generated by the temperature differences, hence density differences between the outdoor and indoor air. For example, higher indoor temperatures can be caused by heat sources, such as occupants and equipment. This pressure difference drives a flow known as stack effect or chimney effect, because of the natural tendency of the hot air to rise and accumulate in the upper part of the space, leading to a stable stratification.

It is of course possible that these two effects act simultaneously on a building. The combination of stack and wind pressure determines the airflow through building openings. The total driving force is the sum of the driving forces induced by both phenomena.

In addition, the determining factor of the vertical stratification is the location of the openings [13]. Two different cases maybe distinguished:

- Mixing ventilation occurs when a single opening is located at the top of the space (Figure 1.1 a). The latter allows the exchange of warm air outwards and cool air inwards, when the temperature of the enclosure is higher that of the ambient one. The incoming cool air descends as a turbulent plume and tends to mix with the air within the space. This leads to a relatively uniform interior temperature distribution.

● Displacement ventilation takes place when there are two openings. One of them is located near the top of the space and the second one near the bottom (Figure 1.1 b). In this way, cool air enters through the lower opening and warm air comes out from above. In contrast to mixing ventilation, it induces large temperature variations within the space, since a vertical temperature gradient in the room is created. It is said that, for the same temperature difference and the openings areas, displacement ventilation leads to more rapid ventilation than mixing ventilation [13]. This illustrates how important is the flow patterns to the efficiency of the ventilation system. The ventilation effectiveness is described as the capacity of an air distribution system in removing internally generated heat or pollutants from the enclosure. The displacement ventilation was analyzed and described by Linden [13], for one, two or multiple sources of buoyancy.

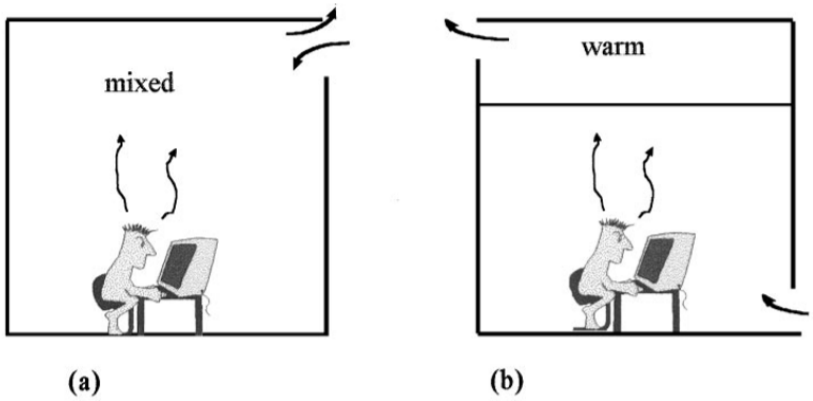

Figure 1.1 - Schematics of mixing ventilation (a) and displacement ventilation (b) from [13].

Displacement ventilation takes advantage when a fluid, adjacent to a hot surface (e.g. occupants and electrical equipment), ascends towards the ceiling level, forming a thermal plume. Then, this plume reaches the ceiling, and spreads out horizontally before flowing out through vents. This is how this system takes advantage of the buoyancy forces to remove contaminants and heat from the occupied zone.

Furthermore, there are two major types of natural ventilation: cross and single-sided ventilation.

● Ventilation is said to be single-sided when the building has one or several openings with the outdoor located on the same wall. It may take the form of either mixing or displacement ventilation depending on the position of the openings.

● Cross ventilation allows a more effective distribution of fresh air since it passes through the room.

For a more detailed discussion about those types of ventilation or about different flow regimes observed, works of Linden [13] and Leenknegt et al. [14] can be consulted.

On the experimental front, tests were made to better understand the underlying principles and characteristics of natural ventilation. Numerous studies have used small-scale models to validate computational fluid dynamics (CFD) models. An often encountered issue in reduced experimental models is maintaining geometric, kinematic and thermal similarity in order to draw reliable conclusions at full scale [13, 15-17]. Geometric similarity is clearly the easiest criterion to meet, since a simple scaling is sufficient. For the other criteria, the similarity theory states that, for a scale model with buoyancy-driven natural ventilation, some dimensionless flow parameters, such as Reynolds number and Grashof number, must remain in the same regime (laminar or turbulent). Nevertheless, with air as working fluid, it is not possible to satisfy the latter condition. According to several authors, such as Etheridge and Sandberg [17], the substitute criterion is to guarantee a fully turbulent flow. As reported by Chen [15], a solution to simulate the actual flow generated by thermal buoyancy in buildings is to use a liquid like salted water. Linden [13] explained that, in this case, the salinity differences within the fluid produce the buoyancy forces. Despite this problem, small-scale models often provide good flow visualization. On the other hand, CFD models encounter difficulties in modeling simultaneously inertial and buoyancy forces and in incorporating some details of the physical model, such as heat transfer through envelope and floors. Actually, there are various limitations in both CFD simulations and scaled models.

Walker et al. [16] investigated buoyancy-driven natural ventilation, with air or water as working fluid, thanks to a reduced-scale building model combined with a numerical study. The prototype building was a commercial office one, with three floors and an open floor plan connected to an atrium. It is worth mentioning that experimental and computational results match. Walker et al. found that buoyancy driven natural ventilation can be enhanced by using stack vents, which can have an important impact on the internal temperatures, and the airflow. They also pointed out that using air as working fluid generates relatively higher indoor air temperature distribution, which increases heat loss through models envelope.

Li et al. [18] examined, by both theoretical analysis and CFD simulation, the buoyancy-driven natural ventilation in a room with large lower and higher level openings. They proved that the assumption for buildings with small openings, saying that the heights of the openings are negligible and thus only displacement ventilation can happen in the space, is not appropriate when large openings are concerned. Moreover, it was shown in the CFD simulation that, in order to increase the airflow rate, increasing the area of the lower opening is more efficient than increasing the upper opening.

Guo et al. [5] evaluated the buoyancy-driven ventilation performance in a large space building through a reduced-scale experimental model and full-scale numerical simulation. Their results indicate that pure buoyancy-driven ventilation cannot keep people thermally comfortable when the ambient temperature is high, in a building with a large glass ceiling. Therefore, in this case, mechanical ventilation is needed.

Furthermore, it is not surprising that the efficiency of ventilation by natural means depends on the environmental conditions. Imessad et al. [19] focused their study on Mediterranean climate characterized by rainy and relatively mild winters and hot-humid summers. They concluded that in these environmental conditions, passive cooling techniques, such as natural ventilation and insulation, offer a significant potential for energy savings.

1.2.2. Night cooling ventilation principle

Taking advantage of the relatively low ambient outside air temperature to cool down buildings and provide clean air is called cooling. This method distinguishes two techniques: the direct and the indirect cooling. Blondeau et al. [12] explained that, on one hand, the direct cooling effect has been used for years and relies on increasing the indoor speeds, by opening windows or using fans. On the other hand, the indirect technique or night ventilation (NV) consists in ventilating the building during nighttime. NV or nocturnal convective cooling is an efficient passive way to cool buildings and presents a significant alternative to traditional air conditioning system [20]. The incoming cool air decreases the indoor air temperature together with the structural elements temperature. So, the building structure is used as thermal energy storage in the cooling period (CP): during nighttime it is cooled down thanks to the wind. The following day, it absorbs the heat generated by humans and devices during what is called the heating period (HP). In that respect, heat transfer occurs twice in this strategy: from building elements (e.g. ceiling, floor, walls) to circulating air during CP, and the reverse transfer happens in the HP, see Figure 1.2. Consequently, NV is particularly appropriate for office buildings, since they are unoccupied at night, unlike households.

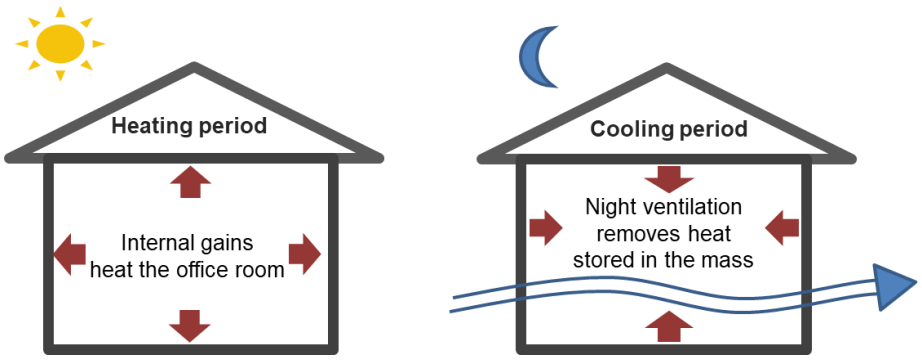

Figure 1.2 - Basic principle of night cooling.

Researches related to NV [12, 20-22], undertaken worldwide since 1997, and reported by Solgi et al. [6], have globally covered the key parameters. The goal is to determine the aspects that give the greatest potential for NV. Mathematical models succeeded in defining which factors play a significant role in the efficiency of the night cooling technique. They are classified into three different groups, namely climate, building and technical parameters. However, the applicability of analytical calculations

is limited, since they assume a lot of simplifications and they cannot take into account the singularities of a case, for example the building shape. Besides, experimental studies and computational studies focus on checking the influence of the previously defined parameters. For instance, Artmann et al. [22] studied the most influential parameters on the effect of the performance of NV which are the climatic ambient conditions effect, the air flow rate entering in the room during nighttime and the thermal capacity of the building or heat gains. The parameters are briefly outlined below:

- Temperature differentials

Shaviv et al. [21] performed a series of time dependent simulations with different climatological conditions and demonstrated that the maximum indoor temperature depends linearly on site temperature swing, i.e., the temperature difference between day and night. Their results indicate a reduction of the indoor temperature of 3 to $6\,K$, in the case of a heavy mass construction type building, in the hot humid climate of Israel, without operating an air conditioning unit.

Geros et al. [20] specifies that when the daily amplitude of the ambient temperature is high, NV technique can be very effective, especially if the minimum ambient temperature is low.

Moreover, the relative difference between indoor and outdoor temperatures during the night period also impacts the effectiveness of NV. In fact, as explained before, the heat transfer occurring between the building's elements and the air is due to cool air coming from outside. Hence, the greater the temperature difference, the greater the heat flux and the efficiency of NV.

- Air flow parameters

As all ventilation techniques, NV relies in transferring an air volume into/out of a building and so the effect of the velocity at which the air moves must be considered. Shaviv et al. [21] performed simulations with different levels of NV: from 2 air changes per hour (ACH) to 30 ACH. They clearly established that even moderate air change rates improve the effectiveness of the technique. In fact, during the CP, increasing the air flow rate results in the indoor air temperature decreasing faster i.e. a higher heat transfer induces a higher efficiency. In short, as suggested by Kolokotroni and Aronis [2], higher NV rates lead to increased energy savings for all the considered ventilation configurations (single sided, cross and stack ventilation). However, Artmann et al. [22] and Kalogirou et al. [23] underlined that this enhancement has a limit, since a critical flow rate exists. This means that above a certain level of ventilation, depending on the building construction and, of course, in the internal heat gains, it is not possible anymore to reduce the overheating degree hours (number of hours in the operating room with a temperature above 26 ºC, [22]).

- Thermal capacity of the building

The thermal mass of a building is defined by the ability of materials to absorb heat during the day, and release it at a later time. High thermal mass means that the building materials induce high resistance to change the temperature. Consequently, an essential requirement to NV effectiveness is having structural elements with a high thermal capacity in order to store the heat produced during the HP. According to the results of Geros et al. [20], the effectiveness of coupling thermal mass and NV is

clearly observed in indoor temperature profiles of the following day. In fact, the internal temperature is lower and its peak is delayed by about three hours. This time lag is actually desirable because the peak now occurs at the end of the workday, when fewer occupants are present in the building. Kolokotroni and Aronis [2] underlined that even a lightweight construction could benefit from natural NV with energy savings of almost 5%. Note that, as Solgi et al. [6] detailed, NV depends on many other parameters like the cooling load, the building shape (dimensions), location (exposure by solar radiation), function and interior arrangement, and the convective heat transfer coefficients (CHTC). Kolokotroni and Aronis [2] also introduced some other variables, such as internal gains, orientation, glazing ratio and operation time for nocturnal ventilation. They demonstrated that the lower the solar and internal gains, the more effective the NV strategy. According to their scenario, increasing the duration of the CP (7:00 pm to 7:00 am instead of 12:00 am to 7:00 am), improves only 2% energy savings. Landsman et al. [24] studied NV performance regarding indoor environmental conditions, adaptive comfort and heat removed. Regarding the indoor thermal conditions, the results indicated that a building, equipped with NV technique, located in a mild climate was able to keep the indoor operative temperature below the upper 80% acceptability comfort limit. However, it happened that the same NV strategies were cooling too much the buildings, being a source of discomfort for the occupants. In addition, a building located in a hot and humid climate was able to keep the operative temperature within the comfort bounds during 88% of the year. But, in the hottest days, the temperatures exceeded the upper 80% comfort limit. Note that they compared their data set with the Adaptive Comfort Standard (ACS) for naturally ventilated buildings from de dear and Brager [25]. Landsman et al. [24] also demonstrated that the NV efficiency of buildings varies mainly due to the differences in their typology and functionality.

To sum up, the exact contribution of NV for a specific building is a function of several parameters. These include the building structural and design characteristics, the climatic conditions and the building's site layout, the applied air flow rate, the efficient coupling of air flow with the thermal mass of the building and the assumed operational conditions [20]. The challenge that emerges here is taking into account all the factors constituting the uniqueness of the building, in addition to the global key parameters and the optimization of the whole procedure.

Kolokotroni and Aronis [2] and Ren and Wright [26] agree to say that four ways in which NV can affect the internal conditions of the building during the day are:

- reducing peak air-temperatures;
- reducing air temperatures throughout the day, and in particular during the morning hours;
- reducing slab temperatures; and
- creating a time lag between the occurrence of external and internal maximum temperatures.

As already pointed out, the purpose of using NV is to reduce the energy demand of office buildings for air conditioning without reducing comfort. Kolokotroni and Aronis [2] based their study on a reference building which is representative of a "typical" air-conditioned office. Under this assumption,

they found that application of NV is beneficial and would result in an energy saving of about 5% and an installed capacity saving of about 6%.

Nevertheless, as a result of the effect of climate change, in the future it is expected higher summer temperatures and longer heat waves periods. Jimenez-Bescos [27] was concerned about that and investigated it for a foreseen scenario. He concluded that the beneficial effect of exposing the thermal mass coupled with NV is very much reduced in simulations for 2030s, 2050s and 2080s of buildings with long life, due to an increase in outdoor temperatures. He also highlighted that these results should be taken into account in the design of new buildings and refurbishment work.

Furthermore, the developed NV strategies can be optimized. For instance, Pfafferott et al. [28] carried out experiments in an office building to ascertain the efficiency of different NV strategies. They established a strategy called “optimized night ventilation” by controlling when the vents are opened with flaps, and by closing automatically the windows when the ambient temperature exceeds $26°C$. This is how, without mechanical ventilation nor change in the shading control, they succeeded in halving the number of hours with $T > 25°C$. This is due to the fact that the heat gains are reduced and the building is cooled down stepwise and effectively.

Despite of all the recognized benefits of NV and the simplicity of the concept, some building scientists are still hesitant to apply this technique. In fact, as discussed before, the effectiveness of the nighttime cooling is affected by many parameters. It results in uncertainties in prediction of thermal comfort in buildings and this is a real issue for this practice. Hence, researchers continue to simulate different cases of NV in order to mature the list of influencing input parameters to increase the reliability of the design of natural NV. For example, Breesch and Janssens [9] highlighted that wind is a highly variable and irregular physical phenomenon and causes a relatively low level of control compared with mechanical ventilation systems. The goal is to acquire profound knowledge to predict accurately the air flow and the heat transfer in order to quantify the naturally driven ventilation rates, as well as the associated effects on building space temperatures.

1.2.3. Use of a suspended ceiling in night ventilation

As it was mentioned before, the interior arrangement of the studied room plays an important role in the effective use of structural thermal mass. In fact, physical characteristics of the office building, like carpeting, ceiling plenums, interior partitions and furnishings, influence the flow of air through the room, and consequently affect its ventilation effectiveness.

Several investigations [27, 29-36] converge in the sense that the greater the thermal mass of the building exposed to the airflow, the greater is the night cooling efficiency. Nevertheless, modern

constructions were not designed to use efficiently their thermal mass. Actually, it is common to find components, among the furniture, acting as insulators. In fact, they prevent the thermal mass to be exposed to the occupied zone, leading to an inefficient heat exchange. For instance, a suspended ceiling (SC) below the slab exhibits an incorrect exposure of the slab for cooling purposes. As a matter of fact, the results of Høseggen et al. [29] confirm that the SC decreases the potential of NV significantly and also increases the number of hours with excessive temperature considerably.

Similarly, Domínguez et al. [30] quantified the effect of acoustic panels on the performance of thermally activated building systems. Ceiling coverage ratios (CCR), i.e., ratios of total panel area to ceiling area of 43%, 60% and 80% were studied. The system cooling was reduced by 11%, 23% and 36% for 43%, 60% and 80% ceiling coverage, respectively. They concluded that cold air stagnation in the plenum and the consequent decrease in convective heat exchange between the occupied zone and the plenum was the major cause of the reduction in cooling performance. In this study, the cooling of the building was not intended to be carried out by night cooling or by natural means, but by active systems.

Jimenez-Bescos [27] simulated scenarios in which the model was equipped either with or without SC. The results indicate that the effect of blocking the slab with a SC increased the percentage of overheating hours.

Fortunately, since this issue emerged, efforts have been done on using this structural element as part of a thermal storage system. Consequently, studies looking for a way to conjugate SCs with satisfactory levels of indoor comfort were carried out.

Jantana and Pukdum [31] compared two scaled models with respect to the impact of the air permeability of a SC on internal heat gains. The models were equipped either with a SC without gap or with a perforated SC in which the air was allowed to pass through. In the latter case, called vinyl perforated ceiling (VPC), the flow is originated by a chimney effect. They demonstrated that a VPC can reduce the room temperature and ceiling heat gain significantly. The study also compared different ratios of the perforated to non-perforated areas −0,01, 0,02 and 0,03 (vinyl perforated area/ solid vinyl area). The experimental results indicated that when the vinyl ceiling area ratio increased, the room temperature decreased. Finally, they concluded that VPC is able to achieve air circulation without any mechanical devices.

Wu et al. [32] investigated the use of a diffuse ceiling ventilation system and established that it has an important energy saving potential. This is due in part to the use of the thermal mass of the diffuse ceiling to improve night cooling efficiency.

In addition, the use of the plenum between the upper surface of the SC and the lower surface of the slab above it for air transport was studied by Hviid and Svendsen [33]. They made several experiments in a full-scale model of a densely occupied room with two perforated SCs made of aluminum and gypsum. They found no local discomfort in the occupied zone, and an air change efficiency comparable with perfect mixing ventilation. So, the concept is adequate for low-energy ventilation systems.

Koschenz and Lehmann [34] equipped the SC of a full-scale office room with a phase change material (PCM). Here, they chose to achieve the control of the thermal storage by using integrated water capillary tube system, so no air ventilation took place. Their results showed that PCMs can maintain good comfort levels in an office room. They also underlined that using pure PCM arose fire precaution considerations. Weinläder et al. [15] also used a SC with PCM, but this time it was ventilated by introducing air in the space between the SC and the slab during nighttime. They obtained a reduction of indoor temperature up to $4°C$.

Jeong and Mumma [35] carried out experiments with free hanging metal ceiling radiant cooling panels (CRCPs) suspended, by wire hangers, under the ceiling of a mechanically ventilated space. In this system, both the top and the bottom surface of the panel are used as heat transfer surfaces. Therefore, the total cooling capacity per unit panel area is higher than that of a top insulated panel. The CCR is usually less than 50% in most spaces where free hanging panels are installed. This ratio affects the panel cooling capacity. Tests showed that higher panel cooling capacity was obtained at lower CCR. This comes from increased free air movement around the panels and increased radiation heat flux per unit panel area with decreased CCR. Their results also indicate that this system has a cooling capacity enhancement of over 17% at normal operation, under mixed convection.

In short, according to the articles previously mentioned, an air permeable SC may have some advantages since it allows mixing between the air below and above it and a SC without full coverage improves thermal cooling.

1.3. Objectives

The previous section points out that using SC with peripheral gaps is a solution to enhance the NV strategy in modern buildings. However, the SC configuration optimizing the efficiency of the cooling technique is not clearly identified yet.

This experimental study is a follow up of the work of Lança et al. [37] that aims to characterize the effectiveness of a SC that does not totally cover the slab, thus allowing the air flow and the direct heat exchanges in the space between the SC and the slab, called plenum. For this purpose, the same reduced scale model of an office building, already available and equipped with the instrumentation, was employed in the present work. So, the particularities of the night cooling strategy in [37] are the use of a SC with gaps and the openings for ventilation located above it, see Figure 1.3.

More precisely, the first goal of the present thesis is to confirm the conclusions of Lança et al. [37] regarding the heating period. To do so, the present work investigates the performance of several designs of a SC in the model. Secondly, it is important to focus on the cooling period and analyze the influence of the SC since it is the lack of knowledge on this phase that motivates this work. In fact, during their experiments, Lança et al. [37] used relatively high air velocities, about 6 m/s, to ensure a fully turbulent flow. As a consequence, the cooling period turned out to be short and the steady state was achieved rapidly. Due to this, no distinction could be made between the results from the experiments conducted with the different SC configurations and this prevented detailed analysis of the CP. Thus, the tests are now made with two lower air speeds, which still guarantee a turbulent flow, as explained in chapter 2.

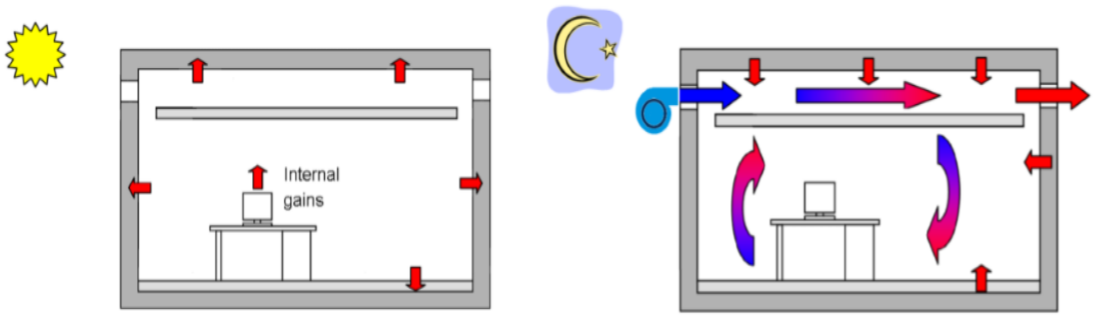

Figure 1.3 - Schematic of the night cooling strategy used in [37].

1.4. Outline of the thesis

The thesis is organized into five chapters:

1 – Introduction

This first chapter gives a brief description of the problem and the reasons justifying its investigation. Then, a literature review presents the subject of buoyancy driven ventilation and night cooling principle in enclosures, as well as previous experimental and computational studies done using suspended ceilings. It also outlines the main objectives that were set for this thesis. Finally, the document structure is detailed.

2 – Methodology

The second chapter is divided into two parts. It describes in detail the characteristics of the experimental setup and the procedure used to perform all the tests, together with the instrumentation and the similitudes between the real office and the reduced scale model. This chapter also contains the computation of the experimental uncertainties of the measurements and specifies the procedures used in the case of the air velocity and the temperature.

3 – Experimental results and analysis

The results obtained for the experimental cases and their discussion are described in this chapter, which is subdivided into three sections. The first part describes all the results obtained from one case, as a complete example. The second part points out the changes that are found when one of the parameters, namely the type of SC, the power of the electrical resistance or the air speed, is changed. So, it compares the results obtained for different experiments for the heating period with the ones from Lança et al. [37] and also analyzes the cooling period. The third part draws conclusions from the results previously presented.

4 – Conclusions and future work

The last chapter summarizes and concludes the conducted work. Besides, recommendations for future work to improve the energy efficiency of the buildings are presented.

5 – Appendix

This chapter is devoted to the additional results.

2. Methodology

2.1. Experimental set-up

In order to confirm the results from Lança et al. [37] and complete the analysis on the optimization of the night cooling phenomenon by using a SC with a peripheral gap, the same experimental set-up was used. It is installed in a building belonging to the Civil Engineering National Laboratory (LNEC - Laboratório Nacional de Engenharia Civil), located in Lisbon. The real compartment taken into consideration is located in Coimbra, Portugal, and is simply composed of one room with two identical cross night-ventilation openings. The 1/7 reduced scale model of the real office room has an interior with dimensions of $Lx \times Ly \times Lz = 0{,}75m \times 1{,}25m \times 0{,}43m$. In Figure 2.1, it is possible to see the walls, the floor, the ceiling and the SC composing the model. The materials of the model's elements are presented in Table 2.1.

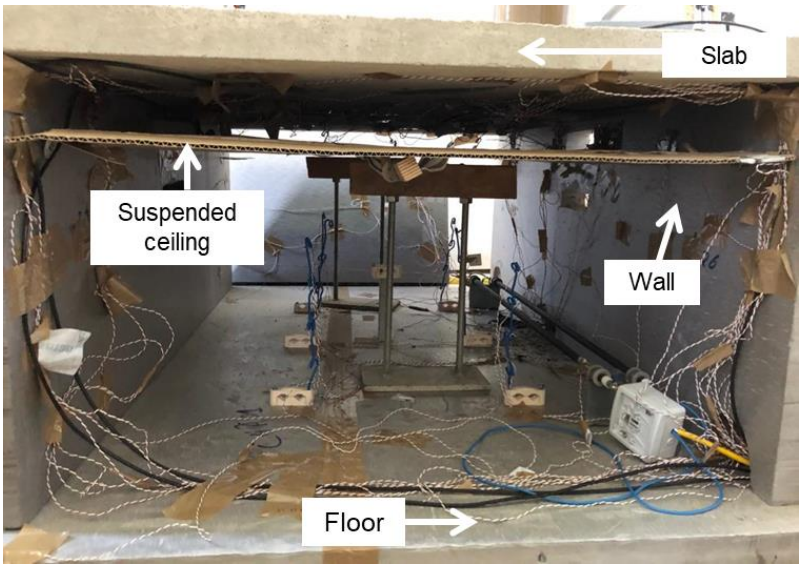

Figure 2.1 - Inside view of the reduced scale model with its components.

Table 2.1 - Materials of the elements of the experimental model.

Element of the model	Material	Thickness
Walls and floor	Extruded polystyrene (XPS) insulation panels	$50\ mm$
Ceiling	Concrete slab	$40\ mm$
SC	Cardboard	$4\ mm$

Some experiments are conducted with a variable peripheral gap between the SC and the surrounding walls, aiming to enhance the night cooling technique. This space allows the air to circulate between the plenum, which is the area between the concrete slab and the SC, and the occupation

zone, which is the area below the SC, shown in Figure 2.2. In this thesis, three different SCs are used and experiments without SC are also conducted, for comparison purposes. The sizes of the gaps in directions x and y, defined by percentages of the longest dimension of the room ($1{,}25\ m$), are presented in Table 2.2. The reason for the use of SCs with peripheral gaps in the present work is twofold. First, the SC is still hiding the technical components that can be found in buildings (cables and pipes, for example) from the occupants view because it partly covers the ceiling. Secondly, those gaps promote heat and mass transfer between the zones above and below. In this way, the heat exchange with the concrete slab is more efficient.

Table 2.2 - Dimensions of the gaps between the SC and the surrounding walls for the different cases.

	A	**B**	**C**	**D**
Gap size in percentage	0%	2,5% x 2,5%	7,5% x 10%	100%
Length in direction x (mm)	0	32	90	No SC
Length in direction y (mm)	0	32	125	

In order to simulate the internal heat gains (heat dissipated in the office by its occupants and the electrical equipment, producing together a thermal plume), a cylindrical electrical resistance is turned on during the occupation period, which is assumed to be from 8 a.m. to 8 p.m. So, the heating period (HP) lasts 12 hours during which a heat load of 62 or 100 Watts (W) is released from two pipe-type resistances, of 1 meter long, situated horizontally, on the floor, close to the wall of the air inlet side. This positioning near a wall has been chosen because it originates an asymmetric plume. In fact, the air in the vicinity of the electrical resistance is heated and ascends, due to buoyancy, to the top of the room, passing through the peripheral gap of the SC. It eases the heat exchanges with the slab.

The model is cross-ventilated because it has two identical openings located at opposite walls so the cool incoming air passes through the enclosure. The supply and the extraction rectangular shaped slots are located above the SC, which is $120\ mm$ below the lower surface of the concrete slab. This configuration, called “Opening 1” or “O1”, originates a wall jet along the slab [37]. The experimental set-up is also equipped with two openings (supply and extraction), identical to those mentioned above, but located below the SC and called “O2”. Those extraction slots were used in Lança et al. [37] study, but not in this thesis, i.e., they remain closed.

In order to simulate the wind mostly blowing from North to South, in Lisbon, during the night, the air supply slot is passive, whereas the extraction slot is equipped with a fan. From 8 p.m. to 8 a.m. of the following day, the fan extracts air from the plenum to the exterior and allows admission of ambient cool air from the supply slot. So, the cooling period (CP) also lasts 12 hours during which an airflow of $1{,}1$ or $2{,}05\ m/s$ cools down the enclosure. The fan is located at the extraction slot, rather than at the supply one, to avoid the heat dissipated by the motor to be transferred by convection to the interior of the model, modifying the temperatures. According to Lança et al. [37], this is supposed to reproduce

the strategy adopted in buildings that has the purpose of minimizing the heat gains from outdoors. As Figure 2.3 (a) indicates, the air outlet opening, where the fan is mounted, is connected to a plenum. This allows the pressure at the extraction slot to be approximately uniform and minimizes flow disturbances [37].

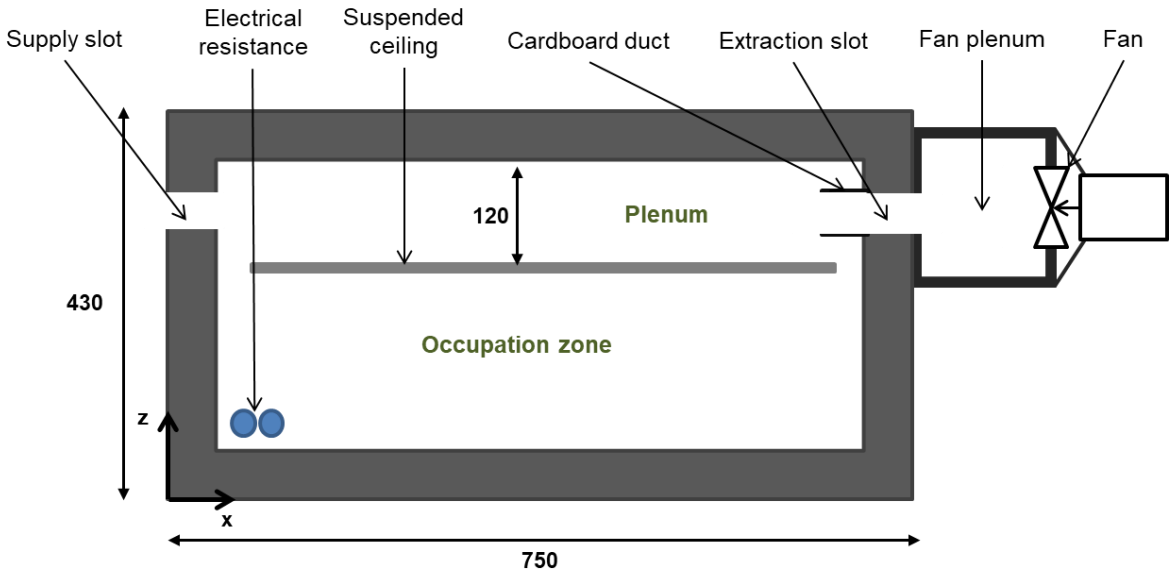

Figure 2.2 - Schematic of the experimental set-up (dimensions in millimeters).

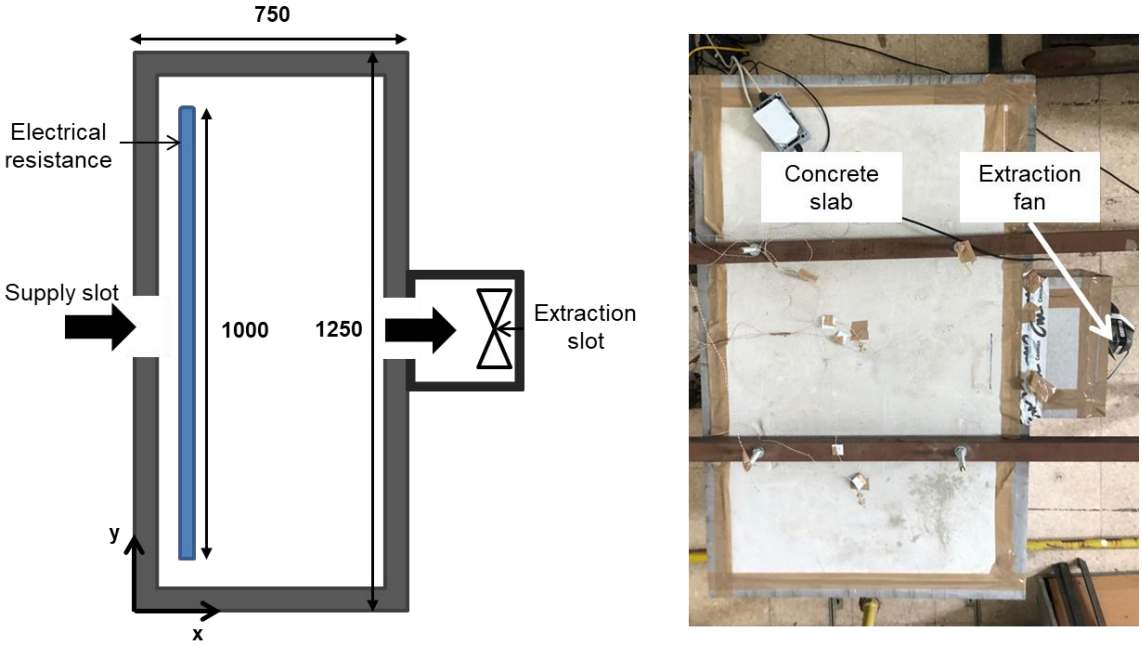

(a) (b)

Figure 2.3 - Top view of the experimental set-up. (a) Schematic (dimensions in millimeters). (b) Photo.

The electrical resistance and the fan are regulated by a control post, shown in Figure 2.4. The whole current provided to the experiment is turned on and off thanks to the circuit breaker. The heat load is controlled by a dimmer, previously calibrated, which regulates the power delivered to the

electrical resistance. In the same way, the air velocity is determined by another dimmer that controls the electric motor speed of the fan. A programmed clock is used to automatically turn on and off the electrical resistance and the fan at the requested hours. For example, at 8 a.m. the fan is stopped and the electrical resistance starts to heat the enclosure with the programmed power.

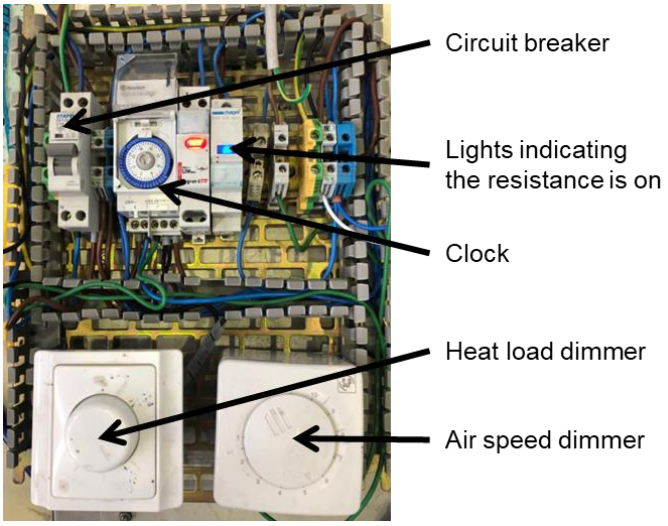

Figure 2.4 - Control post with its components.

In order to calibrate the air speed dimmer, an accurate determination of the volumetric flow rate is required. In that respect, a short rectangular duct made of thin cardboard is attached to the inner side of the extraction slot, as shown in Figure 2.2. In fact, without this cardboard duct, the velocity that was being measured at the extraction slot was not uniform. Note that the cardboard duct was kept during all the tests.

2.2. Similitude between full scale and reduced scale rooms

As mentioned before in chapter 1, geometric, kinematic and thermal similarities between the full scale room and the reduced scale model should be preserved to be able to make trustworthy conclusions at full scale from reduced scale experiments.

While building the reduced scale model of the real office room, Lança et al. [37] managed to keep the geometrical similarity between the system being simulated and the experiments. Moreover, in the case of the experiments, the internal flow is dominated by mixed (i.e., free and forced) convective heat transfer, and radiative transfer at the boundaries is not significant. In general, it is convenient to use dimensionless numbers to describe a physical phenomenon. In this respect, during the HP, the electrical resistance is on, and the internal flow is dominated by the heat source thermal plume and, consequently, the Grashof number, noted Gr, is the relevant dimensionless parameter. Whereas

during the CP, the fan is extracting air from the enclosure, and the internal flow is dominated by the forced convection due to wind cross ventilation and, therefore, the Reynolds number, noted Re, is the key nondimensional parameter. However, it is not feasible to keep those dimensionless numbers equal in both cases with air as working fluid [13, 15-16]. What matters the most is to ensure a fully turbulent flow and this was guaranteed in the present work, as discussed below.

Lança et al. [37] used the modified Grashof number defined by Noto et al. [38], in the case of a thermal plume originated by a line heat source, to compute the one corresponding to the real office room. The calculation was made for the lowest heating power, assumed to be $1{,}4\ kW$, dissipated into the real office during the day, using the following equation:

$$Gr = \frac{g\ \beta\ q' l^3}{\vartheta^2\ k} \tag{2.1}$$

where g is the gravitational acceleration in m/s^2, β is the thermal expansion coefficient in K^{-1}, q' is the heat flux rate per unit length in W/m, ϑ represents the kinematic viscosity in m^2/s and k stands for the thermal conductivity of the air in $W/m \cdot °C$. The distance from the heat source to the SC is taken as the characteristic length, noted l. So, the order of magnitude of the modified Grashof number of the real office room is 10^{12}. Then, they compared it to the critical modified Grashof number for the end of the transition to turbulence which is 2×10^9, according to Noto et al. [38] and concluded that the flow is turbulent in the real office room, even for the lowest heating power. What changes for the calculation of the modified Grashof number in the reduced scale model is the mathematical product $q' l^3$. Yet, since the characteristic dimension of the model is much smaller than that of the room, the heat rate per unit length would need to be much greater in the model, to maintain the same Grashof number, and this is not feasible. Therefore, the same heating power per unit area of the floor was considered, yielding a modified Grashof number of 5×10^9 in the reduced scale model, which allows the flow to be fully turbulent.

Concerning the evaluation of the Reynolds number, the mean velocity at the supply opening is taken as the characteristic velocity, and the hydraulic diameter, noted D_H, as the characteristic dimension. In fact, the latter is generally used in the case of a three-dimensional free jet issuing from a rectangular cross-section nozzle, and was used by Lança et al. [37], even though the jet is confined. The Reynolds number is equal to $3{,}4 \times 10^4$ for the real office, which is greater than the critical Reynolds number above which the flow is fully turbulent, which ranges between 10^4 and 2×10^4, according to Dimotakis [39]. In order to maintain the same Reynolds number in the office room and in the reduced scale model, Lança et al. [37] used a mean velocity u_m seven times greater in the model than in the full scale office room. However, this high air speed leads to the enclosure being cooled down very fast, which makes difficult to analyze the CP. Consequently, in the present thesis, lower velocities, namely $1{,}1$ and $2{,}05\ m/s$, are used, as explained in section 2.4.

2.3. Instrumentation

During all the tests, three different types of measurements were performed using specific equipment described in Table 2.3.

Table 2.3 - Instrumentation description.

Measurement	Instrument	Brand
Air, slab and resistance temperatures	66 T type thermocouples	
Air velocity of the entry plane of the cardboard duct	1 air velocity transducer	TSI, model 8455
Heat fluxes on the lower surface of the slab	2 heat flux sensors	Hukseflux, model HFP01

The data acquisition was made thanks to two data loggers (Datataker, models DT 515) and one channel expansion module (Datataker, CEM). At the end of each experiment, the data gathered by the data loggers was retrieved with the software DeLogger to be treated. An overall view of the installation with the instrumentation is shown in Figure 2.5.

As described in the Table 2.3, one anemometer was always evaluating the air velocity at the same location of the entry plane of the cardboard duct during the experiments. The latter point is called the reference point, see Figures 2.5 and 2.11, and its velocity is named u_{ref}. This anemometer is located above the SC.

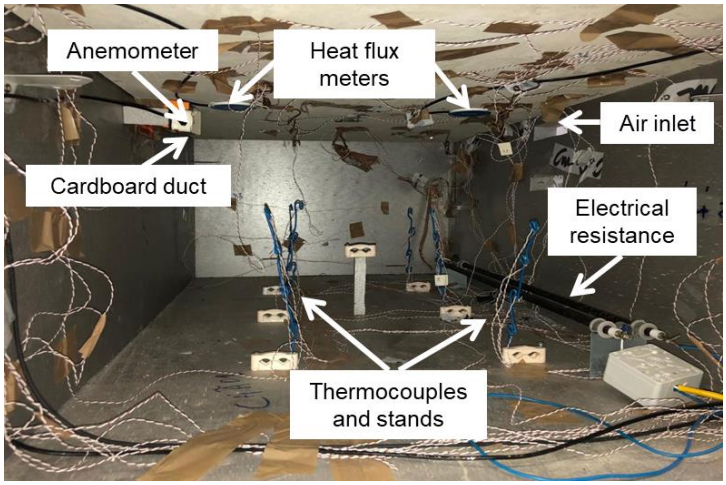

Figure 2.5 - Inside view of the reduced scale model with its equipment.

Two heat flux sensors attached to the lower surface of the slab, F1 and F2, measured the heat flux transferred by conduction through the slab, which is equal to the sum of the net radiative

component (difference between flux emitted and absorbed by the slab) and the convective flux component. F1 is located at $x = L_x/6$, $y = L_y/2$, i.e., just downstream of the supply slot, and F2 at $x = 5L_x/6$, $y = L_y/2$, i.e., next to the extraction slot.

Six vertical columns, of seven thermocouples (TCs) each, measured the air temperature inside the room, as illustrated in Figures 2.6 and 2.7. Each TC is referenced by two digits. The first digit identifies the position of the column in the enclosure. Thus, TCs 11 to 17 and 61 to 67 are located at $y = 3L_y/4$, TCs 21 to 27 and 51 to 57 at $y = L_y/2$, and TCs 31 to 37 and 41 to 47 at $y = L_y/4$. TCs 11 to 17, 21 to 27 and 34 to 37 are positioned at $x = L_x/3$, and the others are at $x = 2L_x/3$, with the exception of TCs 31, 32, 33 which are at $x = 0{,}18\ m$ and TCs 41, 42 and 43 which are at $x = 0{,}43\ m$. The second digit is related to the height at which the TC is located in its own column. So, TCs referenced with a second digit being 1, 2 or 3 are occupying the plenum, while 4, 5, 6 and 7, designate the TCs placed in the occupation zone.

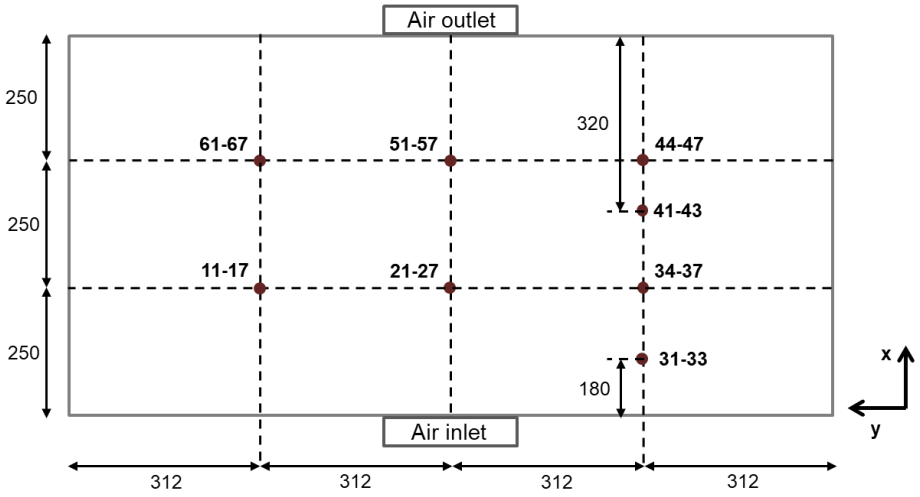

Figure 2.6 - Location of the columns of thermocouples (dimensions in millimeters).

Moreover, fourteen TCs are attached to the lower surface of the slab and eight others are measuring the temperature of the concrete slab at different depths, as shown by Figures 2.8 and 2.9. Only some of the results coming from all those TCs are presented. Two of the TCs placed in the slab core were used by Lança et al. [37] to present the results and compare the slab's behavior in the different cases. TC S8 is attached to the lower surface of the slab at $x = L_x/2$ and $y = L_y/2$, and TC S17 is located at a distance of $26\ mm$ from TC S8 along z direction, so it is embedded in the core of the slab.

In addition, one TC is always attached to the resistance to measure its temperature noted T_R. Finally, the laboratory temperature T_{lab} is measured by a TC far away from the heat released by the instrumentation.

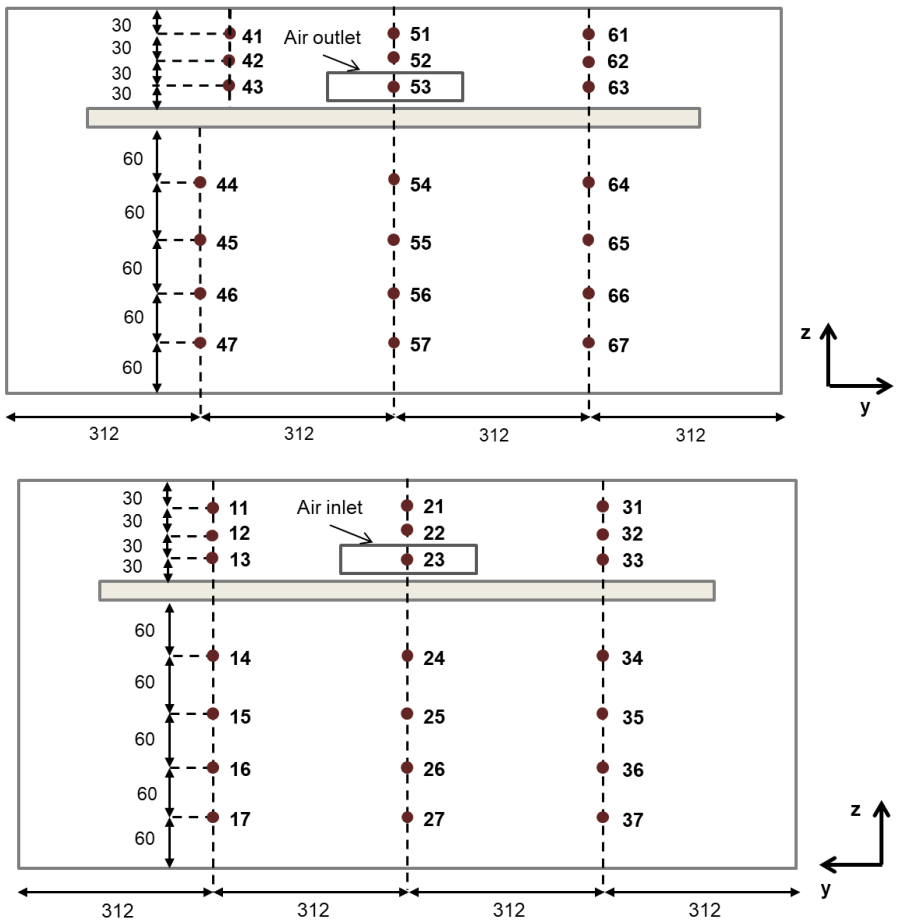

Figure 2.7 - Front and back view of the model geometry and location of the thermocouples with the corresponding dimensions in millimeters.

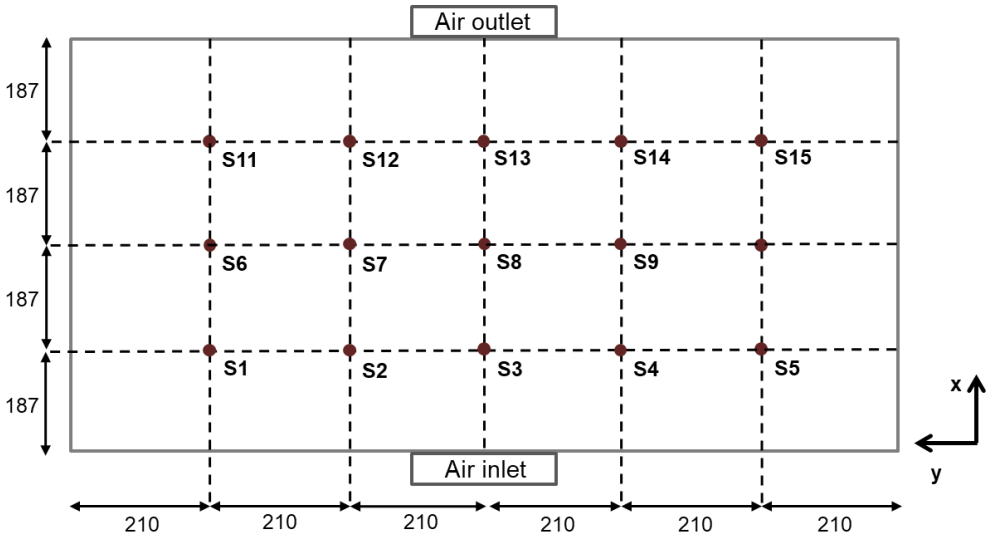

Figure 2.8 - Inner surface of the slab and the numbering of the thermocouples attached to it (dimensions in millimeters).

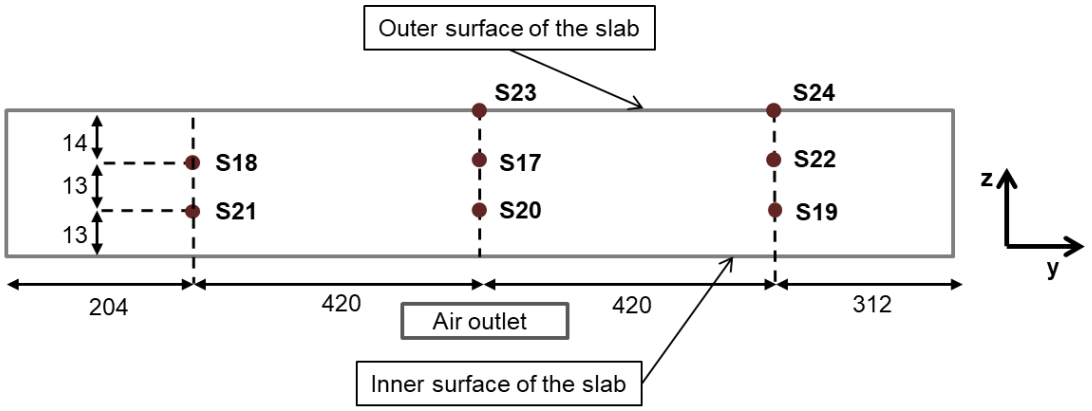

Figure 2.9 - Numbering of the thermocouples placed in the slab core (dimensions in millimeters).

2.4. Uncertainty of the measurements

There are two methods to evaluate the uncertainty of the measurements [41]: a Type B uncertainty is estimated thanks to manufacturer's specifications, whereas a type A uncertainty is evaluated from the experimental standard deviation that characterizes the measurement. In the present work, both methods are employed, as explain in the sections below.

2.4.1. Type B evaluation of uncertainty

According to Lança et al. [37], uncertainties in the measurement of the electrical power measurement (multimeter) and the heat flux are mainly due to calibration, inherent stochastic variability of the measurement process and the overall effects of environmental factors, such as temperature, humidity and pressure. For those measurements, the uncertainty analysis relied on the calibration certificates of each instrument that is provided by its manufacturer. Considering a 95% confidence interval, the following expanded uncertainties were estimated: $U_{P95} = \pm 0{,}99W$ for the electrical power and $U_{H95} = 0{,}108\, W/m^2$ for the heat flux. These values are the same as those reported by Lança et al. [37] because the measuring instruments are the same.

2.4.2. Type A evaluation of uncertainty

In the case of the temperature (thermocouples) and air velocity (anemometer), the expanded uncertainty was estimated using data from a set of tests done by an accredited laboratory. In general, the accuracy of the temperature measurement is essentially influenced by the calibration, the voltage

the measurement of the data logger, the reference temperature, and the composition of the thermocouple alloys [40]. The methodology for these calculations followed the procedures of the Guide to the expression of uncertainty in measurement [41]. The measurement chain used in the experiments was calibrated and the following expanded uncertainties were estimated, considering a 95% confidence interval: $U_{T95} = \pm 0{,}16\,°C$ for the temperature and $U_{u_{ref}95} = \pm 0{,}21\,m/s$ for the air velocity. The procedure followed is detailed in the next paragraphs.

2.4.2.1. *Air velocity*

Before conducting the three day experiments, a preliminary calibration of the speed of the air flow crossing the room was made. As already mentioned in chapters 1 and 2, the main goal is to ensure a turbulent flow and to be able to draw conclusions for the real office room with the results from the model. To do so, firstly the dimmer controlling the electric motor speed of the fan had to be calibrated. In other words, it is necessary for the experiments to know what air velocity (in m/s) corresponds to which position of this dimmer. Secondly, the volumetric flow rate, exiting by the cardboard duct, had to be accurately determined for four air speeds. These tested velocities, $u = [1{,}41\,;\ 1{,}57\,;\ 2{,}26\,;\ 2{,}74]\,m/s$, were chosen much lower than $6\,m/s$, the one used by Lança et al. [37]. Finally, the linearity of the relationship between the flow rates and their reference velocity had to be verified in order to allow the linear interpolation for intermediate values.

Measurements of the air velocity were performed inside the reduced scale model. A grid at the scale of the rectangular cardboard, drawn in the Cartesian coordinate system (y, z), was used to locate the different points of measurement. To do so, the instrumentation consisted of:

- one hot wire anemometer (Airflow; TA5), measuring successively the speed at each point of the grid of the entry plane of the cardboard duct. This anemometer was hold by a support and was moved after each measurement to a new point;
- one air velocity transducer (TSI; model 8455), wired to a power supply. This anemometer is the one described in section 2.3. It kept measuring the reference velocity, called u_{ref}, see Figures 2.5 and 2.11;
- one data logger (Datataker, model DT 515) to store the velocities measured at the reference point.

In order to plot dimensionless velocity profiles at the extraction slot, the velocity was measured along the four straight lines drawn in the grid, using the hot wire anemometer. Two lines having the y coordinate value fixed and different z coordinate, numbered 1 and 2, and the other two with the z coordinate fixed and different y coordinate, numbered 3 and 4, visible in Figure 2.10. More measurements were made close to the edges of the cardboard duct to allow a more precise calculation of the flow rate. For each of the speeds, this quantification was made and a mean velocity, called u_m, was calculated with an arithmetic average of the measurements made the lines 1 to 4 drawn in the grid. Note the distinction between the reference velocities, which are the ones measured by the reference anemometer (see Figure 2.11), and the mean velocities, which are calculated with the measurements made in the lines 1 to 4 of the grid. Finally, the values of the velocities measured

by the hot wire anemometer were divided by the mean one in order to plot the dimensionless velocity profiles at the extraction slot, see Figure 2.12 for the results for the higher speed, and Figure A.1 in Appendix A for the others.

Figure 2.12 shows that the cardboard duct plays its role since the velocity is approximately constant all along the duct's inlet cross section, in directions y and z, with the exception of the edges. In fact, the peaks of velocity between the boundary layer and the constant velocity profile are due to the flow acceleration caused by the obstruction created by the thickness of the cardboard. The velocities in the boundary layer, close to the vicinity of the inner surface of the duct, are quasi null because of the no slip condition at the surface of the duct.

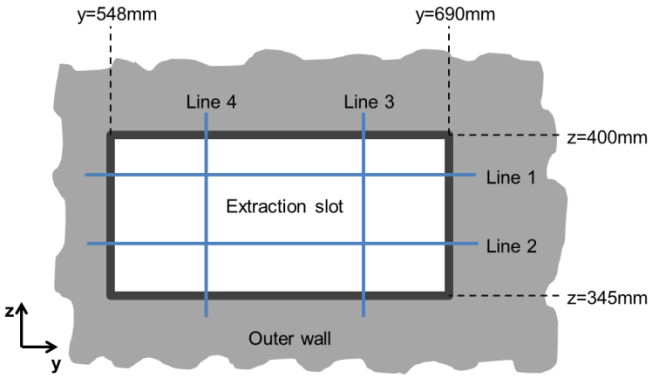

Figure 2.10 - Vertical cross section of the extraction slot (view from the exterior of the reduced scale model).

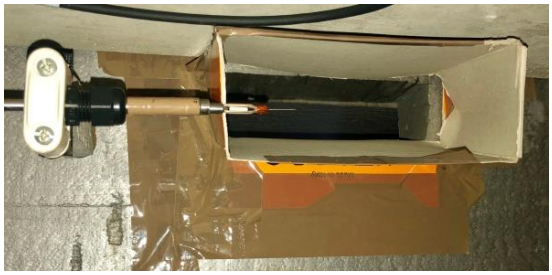

Figure 2.11 - Picture of the reference anemometer in front of the cardboard duct.

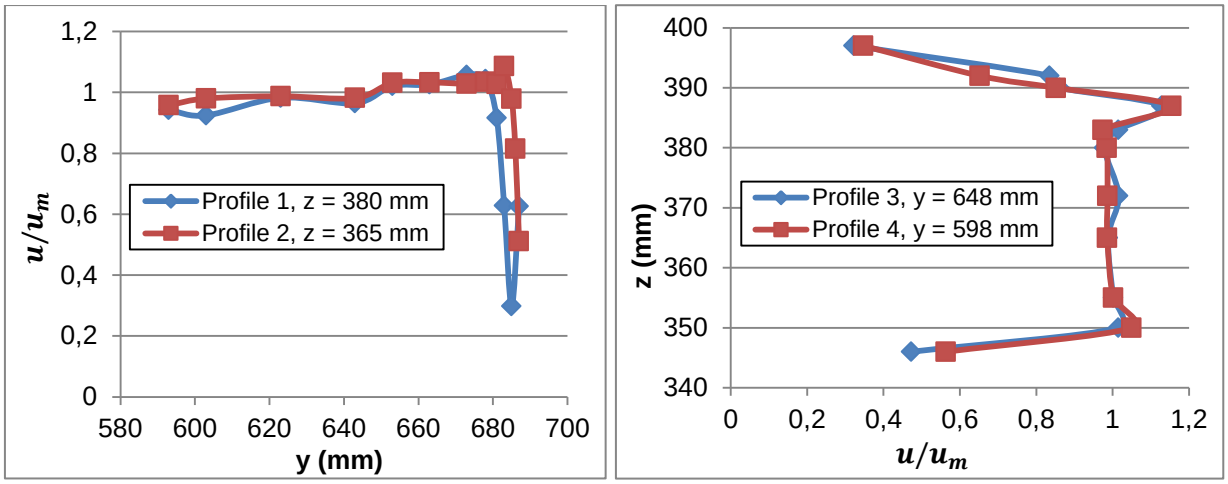

Figure 2.12 - Measured nondimensional velocity profiles at the extraction slot for the requested velocity $u = 2{,}74\ m/s$.

Furthermore, it is assumed that the reduced scale model has low air permeability through the joints of the walls [37]. That is why we consider that the inlet mass flow rate is equal to the extraction one, for the steady state condition. In addition, the supply and extraction slots have the same dimensions and the air density remains nearly unchanged because the range of temperature variation is small. For these reasons, it is considered that the mean air velocity at the supply and extraction slots is equal.

To conduct the experiments, the selected air speeds are: $u_1 = 1{,}4\ m/s$ corresponding to the dimmer positioned at 1, and $u_2 = 2{,}3\ m/s$ corresponding to the dimmer positioned at $5{,}5$.

Once all the measurements on all the profiles were made, for the requested speeds, the corresponding volumetric flow rates, noted Q, were calculated using the following formula:

$$Q = \sum_i u_i A_i \tag{2.2}$$

where subscript i identifies the measurement made at point i, u_i denotes the velocity at point i, and A_i stands for the area of the rectangle represented by point i.
It was assumed that each velocity was constant in the small area around its location. In the vicinity of the inner surface of the duct, only one velocity measurement was used, whereas for the rest of the inlet cross section, far from the boundary layer, an average of two velocities was taken. The results are presented in Table 2.4.

The measurements of the reference velocity, taken by the air velocity transducer, were unloaded from the data logger. An average and a standard-deviation were computed for each requested speed. A curve of the volumetric flow rates versus the corresponding reference velocities was plotted in Figure 2.13.

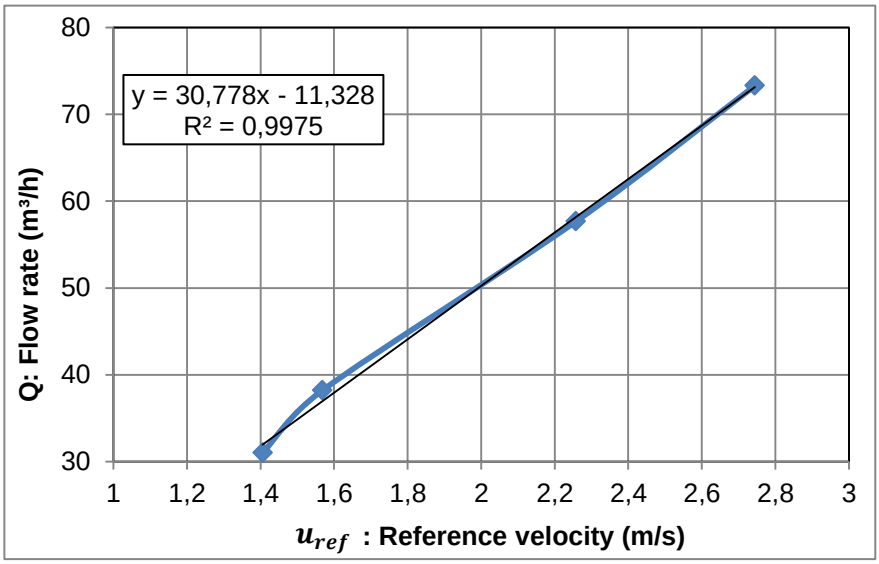

Figure 2.13 - Volumetric flow rates versus the corresponding reference velocities.

In order to calculate the Reynolds number of the reduced scale model corresponding to each of the four requested velocities, air speeds, denoted by u_Q, were computed from each volumetric flow rate, Q, and the area of the card box's entry plane, A, with Equation (2.3). The results are presented in the Table 2.4.

$$u_Q = \frac{Q}{A} \ (m/s) \tag{2.3}$$

The Reynolds numbers are computed using the previously calculated velocities:

$$Re = \frac{u_Q \ D_H}{\vartheta} \tag{2.4}$$

where ϑ is the kinematic viscosity in m^2/s, and the hydraulic diameter noted D_H, in m, calculated with l_y and l_z, the cardboard duct dimensions in y and z directions:

$$D_H = \frac{4\ (l_y\ l_z)}{2\ (l_y + \ l_z)} \tag{2.5}$$

As Figure 2.13 shows, there is a linear relationship between the flow rate and the reference velocity, for almost all the range of tested velocities. In fact, a correlation coefficient of $0{,}9975$ was obtained from the linear regression analysis, but a deviation is observed for the lower velocities, i.e., for lower Reynolds numbers. Moreover, the significant uncertainties on the velocity measurement prevent to affirm that the flow is fully turbulent. This is why, in addition to using the velocity profiles tool, the calculation of the Reynolds numbers has been done. According to the results from Table 2.4, velocities which are greater than $2\,m/s$ have Reynolds numbers higher than the critical Reynolds number, which ranges between 10^4 and 2×10^4 [39]. Above this critical number the flow is considered fully turbulent. Nevertheless, air speeds which are lower than $2\,m/s$ present Reynolds numbers lower than 10^4, but higher than $3\,000$ indicating that the flow would be turbulent. In fact, as illustrated in the Moody Diagram, $Re = 3\,000$ marks the end of the transition region between the laminar flow and the turbulent one. This is in agreement with the deviation that can be seen in Figure 2.13 for the reference velocity of $1{,}41\ m/s$.

To estimate the uncertainty on the volumetric flow rate, the methodology used follows the procedure of the Guide to the expression of uncertainty in measurement [41]. Equation (2.2) is a function relating the magnitude, here Q the flow rate, with the input quantities, noted x_j, which in this case are the velocity at point i, and the area represented by point i. In addition, these input quantities are not correlated. So, the variance of Q is given by the following expression, [41] which uses a first order approximation of the Taylor series:

$$S^2(Q) = \sum_{j=1}^{2} \left(\frac{dQ}{dx_j}\right)^2 S^2(x_j) = \left(\frac{dQ}{dx_1}\right)^2 S^2(x_1) + \left(\frac{dQ}{dx_2}\right)^2 S^2(x_2) \tag{2.6}$$

where *j* denotes the input quantities, which are two in this case, and $S^2(x_j)$ their variance.

Here, because the area and the velocity at each point of the grid node are not correlated, Equation (2.6) can be derived and developed and the following expressions are obtained:

$$S^2(Q) = \left(\frac{dQ}{du_i}\right)^2 S^2(u_i) + \left(\frac{dQ}{dA_i}\right)^2 S^2(A_i) = \sum_i {A_i}^2 S^2(u_i) + {u_i}^2 S^2(A_i) \quad (2.7)$$

where i represents points measurements of the grid, u_i the velocity at point i, and A_i the area represented by point i.

Moreover, the sum of all the small areas A_i is the cardboard duct's area noted by A, so:

$$\sum_i A_i = A = l_y l_z \quad (2.8)$$

where l_y , l_z are the cardboard duct dimensions in y and z directions. These values were read with a ruler, so reference [41] indicates that their variance is calculated as follows:

$$S^2(l_y) = S^2(l_z) = \frac{1}{3}\varepsilon^2 = \frac{1}{3}(\frac{1}{2} \times 1 \times 10^{-3})^2 = 8{,}33^{-8}\ m^2 \quad (2.9)$$

So, with the Equation (2.8) defining a function, it is also possible to calculate the area's variance:

$$S^2(A_i) = {l_z}^2 S^2(l_y) + {l_y}^2 S^2(l_z) = 1{,}92^{-9}\ (m^2)^2 \quad (2.10)$$

In order to calculate the variance of the velocities measured at the grid nodes, nine readings were made at each node. These values were corrected by a calibration equation plot from a calibration certificate (Appendix B, Table B.1), Then the Excel function "VAR.P.N", which calculates the variance based on the entire population, is used to calculate the variance of each of the four requested velocities, noted $S^2(u_i)$.

Now all the previous elements are used in the numerical evaluation of the variances of the volumetric flow rates. For example, considering the highest velocity, it is obtained:

$$S^2(Q) = \sum_i {A_i}^2 S^2(u_i) + {u_i}^2 S^2(A_i) = 5{,}15 \times 10^{-7}\ (m^3/s)^2 \quad (2.11)$$

Finally, the combined uncertainty of the flow rate Q is obtained, considering a 95% confidence interval, from the respective standard-deviation $S(Q)$ multiplied by a coverage factor $k = 1{,}96$, [41]. Note that the latter factor varies according to the chosen confidence interval. Thus, the range enclosing 95% of the population, called the global uncertainty U_Q, is calculated for each velocity and the results are presented in Table 2.4. For example, the computation of the global uncertainty, corresponding to the highest velocity, uses the result from Equation (2.11) and is expressed as follow:

$$U_{Q95} = \pm\, 1{,}96\sqrt{S^2(Q)} = \pm\, 5{,}06\ m^3/h \quad (2.12)$$

Table 2.4 - Volumetric flow rates, mean velocities and Reynolds numbers for the reference velocities.

Reference velocity	**Flow rate**	**Global uncertainty for the flow rate**	**Velocity used to calculate Re**	**Reynolds number**
$u_{ref}\ (m/s)$	$Q\ (m^3/h)$	$U_{Q95}(m^3/h)$	$u_Q\ (m/s)$	Re
2,74	73,3	5,06	2,61	13 725
2,26	57,67	4,36	2,05	10 800
1,57	38,18	3,92	1,36	7 150
1,41	31,01	1,26	1,1	5 807

Similarly to the calculation of the uncertainty made for the velocities measured in the grid nodes, one variance for each reference velocity was computed thanks to the measurements acquired with the data logger. The obtained global uncertainty for the reference velocities, considering a 95% confidence interval, is:

$$U_{u_{ref}95} = \pm 1{,}96\sqrt{S^2(u_{ref})} = \pm 0{,}21\ m/s \tag{2.13}$$

To estimate the uncertainty on the intercept and the slope from the curve Q VS u_{ref} in Figure 2.13, the methodology used also follows the procedure of Guide to the expression of uncertainty in measurement [41]. According to this methodology, for linear regression, it is possible to obtain the experimental variance of the intercept b and the slope a, and their estimated correlation coefficient r with the following formulas:

$$S^2(b) = \frac{S^2 \sum_i Q_i}{D} = 4{,}997\ (m^3/h)^2 \leftrightarrow S(b) = 2{,}24\ m^3/h \tag{2.14}$$

So, the intercept is $b = -11{,}33 \pm 2{,}24\ m^3/h$.

$$S^2(a) = n\frac{S^2}{D} = 1{,}171\frac{(m^3/h)^2}{(m/s)^2} \leftrightarrow S(a) = 1{,}08\ \frac{(m^3/h)}{(m/s)} \tag{2.15}$$

So, the slope is $a = 30{,}78\ \pm 1{,}08\ (m^3/h)/(m/s)$.

$$r(a,b) = -\frac{\sum_i Q_i}{\sqrt{n\sum_i {Q_i}^2}} = -0{,}95 \tag{2.16}$$

with

$$S^2 = \frac{\sum_i \left[Q_i - Q_i({u_{ref}}_i)\right]^2}{n-2}\ (m^3/h)^2 \tag{2.17}$$

and

$$D = n\sum_i {u_{ref}}_i^{\,2} - \left(\sum_i {u_{ref}}_i\right)^2 (m/s)^2 \tag{2.18}$$

where n stands for the number of observations, i.e. the number of points of the curve, here $n = 4$.

An application of the law of propagation of uncertainty gives the expression for the estimated variance of the predicted value of a correction:

$$u_c^2\left(Q(u_{ref})\right) = S^2(b) + {u_{ref}}^2\, S^2(a) + 2 \times u_{ref} S(a)\, S(b)\, r(a,b) \quad (m^3/h)^2 \tag{2.19}$$

$$\leftrightarrow\ u_c^2\left(Q(u_{ref})\right) = 4{,}997 + 1{,}171 \times {u_{ref}}^2 - 4{,}593 \times u_{ref} \quad (m^3/h)^2$$

The combined standard uncertainty of Q is equal to the positive square root of the combined variance. The numerical results are calculated for each flow rate and therefore for each speed and are presented in Table 2.5.

Table 2.5 - Reference velocities, the corresponding volumetric flow rates and their combined standard uncertainties.

Reference velocity	**Volumetric flow rate**	**Combined standard uncertainty**
$u_{ref}\ (m/s)$	$Q\ (m^3/h)$	$u_c(Q)\ (m^3/h)$
2,74	73,3	1,1
2,26	57,67	0,77
1,57	38,18	0,82
1,41	31,01	0,92

The function “LINEST”, which returns the parameters of a linear trend, was used in *Excel* to confirm the precedent results.

The determination of the uncertainty of the slope enables to plot the maximum and the minimum slope of the curve Q VS u_{ref} presented in Figure 2.14.

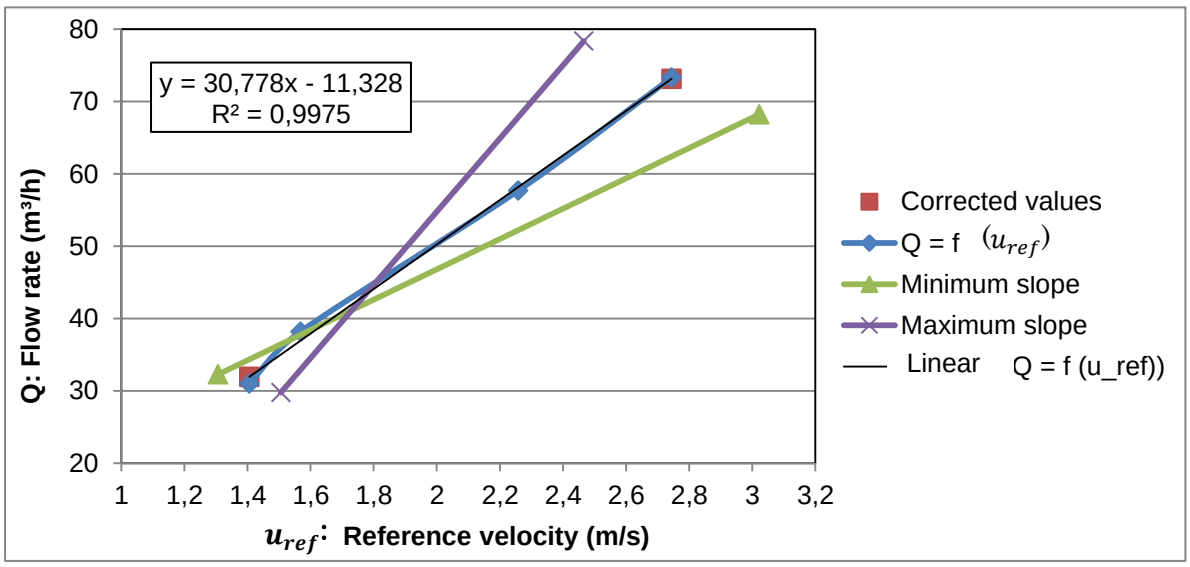

Figure 2.14 - Maximum and minimum slopes of the flow rate as a function of the reference velocity.

2.4.2.2. *Temperatures*

The calibration of the thermocouples was made with the help of LNEC's Applied Metrology Laboratory. All the thermocouples and the data loggers were uninstalled from the reduced scale model and installed in a calibration room, see Figure 2.15. Based on the temperature measurement interval of the three-day experiments, three calibration points ($10°C, 25\,°C, 40°C$) were defined. The automatic procedure lasted two days, during which the thermocouples measurements were recorded every 10 minutes together with the measurements from the reference equipment.

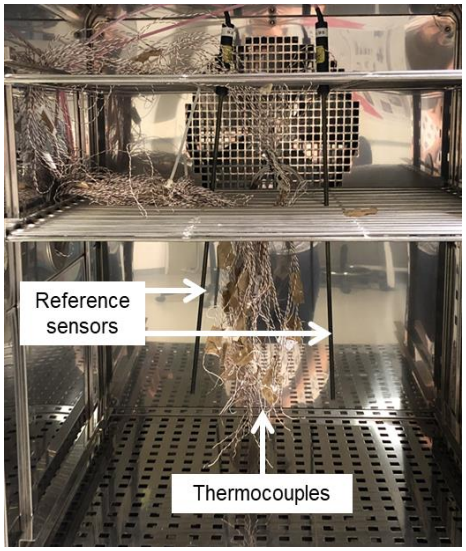

Figure 2.15 - Picture of the calibration room with the thermocouples and the reference sensors.

The laboratory provided a calibration certificate (see Appendix B, Table B.1) with a calibration curve for each thermocouple, which was used to correct the experimental temperature values and improve the measurements accuracy. The laboratory also delivered a plot of the calibration deviations of the TCs without corrections and a plot of the linearity deviations of the TCs after applying the calibration curves. Note that four TCs did not provide any temperature reading, so no correction has been found for them. In addition, it is important to point out that a non-linear effect is observed for the TCs related to one of the data loggers.

Finally, the global 95% expanded measurement uncertainty is close to $0{,}16\,°C$. It includes the following uncertainty components: instrumental uncertainty and drift of the temperature measurement standards (Pt $100\,ohms$ resistance thermometers; thermal uniformity and stability inside the climatic chamber; TC linearity).

2.5. Experimental procedure

The experiments were performed on the simple one-zone building model described before, with periodic outdoor air temperature variations:

- daytime, heat load from the electrical resistance simulating human and devices heat release,
- nighttime, the fan is on and the model is ventilated at a constant ventilation rate.

During a two month period, various NV schemes were tested in order to determine the optimal working conditions: sixteen different experiences of three days (72 hours) each were conducted. For each test, data of three cycles of one HP followed by one CP was acquired by the equipment presented above and stored by the data loggers. The time interval between two measurements was 10 minutes. One of the advantages of the reduced scale model is that it allows to easily change the

size of the SC and to regulate both the intake air speed and the heaters capacity. The test conditions are identified in Table 2.6.

Table 2.6 - Summary of the test cases.

Case	Opening's placement	Heat load (W)	Gap	Mean velocity (m/s)	Re
O1-62-A-1	Above the SC	62	0%	1,1	5 807
O1-62-B-1	Above the SC	62	2,5% x 2,5%	1,1	5 807
O1-62-C-1	Above the SC	62	7,5% x 10%	1,1	5 807
O1-62-D-1	Above the SC	62	No SC	1,1	5 807
O1-100-A-1	Above the SC	100	0%	1,1	5 807
O1-100-B-1	Above the SC	100	2,5% x 2,5%	1,1	5 807
O1-100-C-1	Above the SC	100	7,5% x 10%	1,1	5 807
O1-100-D-1	Above the SC	100	No SC	1,1	5 807
O1-62-A-2	Above the SC	62	0%	2,05	10 800
O1-62-B-2	Above the SC	62	2,5% x 2,5%	2,05	10 800
O1-62-C-2	Above the SC	62	7,5% x 10%	2,05	10 800
O1-62-D-2	Above the SC	62	No SC	2,05	10 800
O1-100-A-2	Above the SC	100	0%	2,05	10 800
O1-100-B-2	Above the SC	100	2,5% x 2,5%	2,05	10 800
O1-100-C-2	Above the SC	100	7,5% x 10%	2,05	10 800
O1-100-D-2	Above the SC	100	No SC	2,05	10 800

In this thesis, the different cases are referenced with an identification number. All the test codes begin with “O1” which means that they were carried out with the supply and extraction slots located above the SC. Then, the number in the identification represents the value of the heat load that was used, 62 or $100\,W$. After that, the letter refers to the peripheral gap between the SC and the side wall. As already explained in Table 2.2, the letter is A when there is no gap, B and C when the size of the gap increases, and is set to D in the case of a room without SC, which was also tested for comparison purposes. Finally, the last number in the identification case corresponds to the air velocity during nighttime, 1 is for a mean velocity at the entry plane of the cardboard duct of $1{,}1\,m/s$ and 2 corresponds to $2{,}05\,m/s$.

The temperature of the laboratory fluctuates following, mainly, the weather and the seasons. That is to say, it varies according to the change of the external atmospheric temperature. It is important to note that this variation of the temperature of the laboratory where the tests were conducted influences the temperature of the air in the reduced scale model. This problem was overcome by defining a temperature difference variable for each TC as $\Delta T = T_{TC} - T_{lab}$ where T_{TC} is the temperature measured by the thermocouple and T_{lab} the temperature of the laboratory. This solution allows to minimize the impact of the laboratory temperature variation, and to compare the temperatures between tests even with different experimental conditions, and made at different times of the year.

3. Experimental results and analysis

This chapter is devoted to the presentation of the results from the tests and their discussion. Experiments were carried out based on the concepts and methodologies (reduced-scale model, equipment, uncertainties, experimental procedure, etc.) described in the previous chapters. The tests are characterized by two types of ventilation: buoyancy-driven (daytime) and mechanical driven flows (nighttime).

In the first part, all the results obtained from one experiment will be completely detailed. The outcome of the chosen test will be presented in terms of air and slab temperatures together with an analysis of the recovered heat fluxes. The second part analyzes the results of the sixteen cases for the HP, to confirm the conclusions of Lança et al. [37], and for the CP, to draw conclusion about the efficiency of the NV strategy. The goal is also to point out the changes that are found when one of the parameters, namely the type of SC, the heat load or the air speed, changes. The ultimate goal is to determine which SC configuration is the best one to improve the performance in lowering ambient temperatures during the occupation period of the office building.

3.1. Complete description of the results from one experimental case

This section depicts all the results obtained from one out of the sixteen tests, which is referenced by the identification number O1-100-C-1. So, the heat load used is $100\ W$, the peripheral gap is defined by 7,5% x 10% of the length L_y, and the mean air velocity during the CP is $1{,}1\ m/s$, as Table 2.6 indicates. Of course, the same type of results is collected for the other fifteen tests.

3.1.1. Evolution of the air temperature during the experiments

The experiments were conducted with the reduced scale mode, situated in one of the buildings of LNEC, from March to June. Obviously, the climatic conditions are considerably changing along this period and the variation of the outside air temperature has an effect on the measurements made in the model. Therefore, data taken at different days may be hard to compare. As explained before in chapter 2, it is the temperature difference, ΔT, between the air temperature measured by the TCs and the laboratory temperature, which will be analyzed for each experiment, which lasted three days. As an example, Figure 3.1 shows the temperature of the laboratory and the difference between the latter and the temperature measured by TC 64, for the test O1-100-C-1. This TC was chosen because it is located at a height corresponding to that of a worker's head in a full-scale office room, since what matters is to keep a comfort temperature for the occupants of the room. This TC is placed at a distance of $60\ mm$ below the SC at point $x = 2L_x/3$ and $y = 3L_y/4$ (see Figures 2.6 and 2.7).

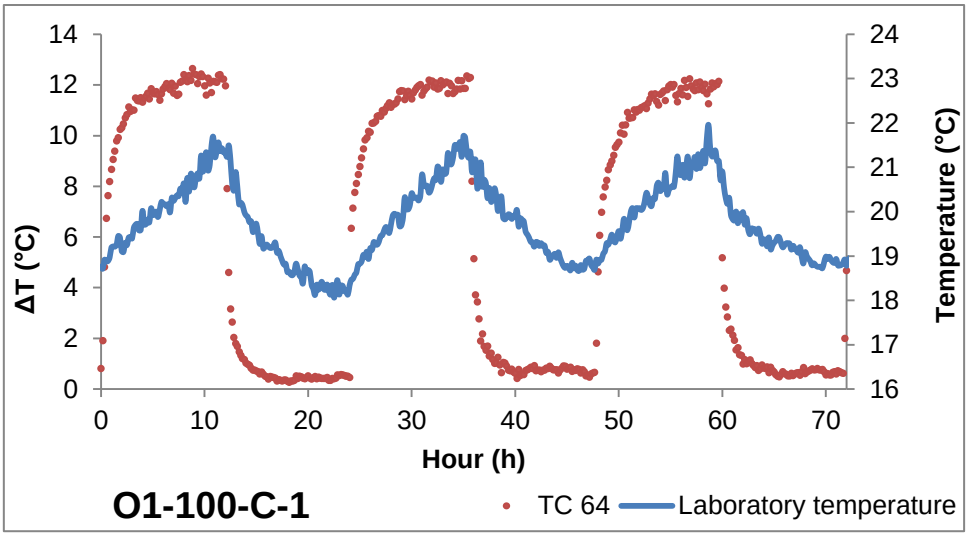

Figure 3.1 - Evolution of the difference between the temperature from thermocouple 64 and the temperature of the laboratory during the three days of the experiment O1-100-C-1.

Figure 3.1 shows that, as expected, the temperature of the laboratory varies daily: it increases and reaches a peak before decreasing during the afternoon and the night. Regarding ΔT variation, a reasonable level of similarity between the three days can be identified in the present case, with the highest temperature differences around $12°C$. Moreover, the disparity between the different days for the temperature of the laboratory does not influence TC 64 measurements. Thus, the values of ΔT measured by the TCs are fairly independent of the laboratory temperature variations. Therefore, in the analysis of the results, the use of ΔT, instead of the temperature measured by the thermocouples, largely reduces the effect of the fluctuation of the laboratory air ambient temperature. More importantly, it allows the comparison between experiments made in different days.

3.1.2. Air temperatures

First of all, it is worth mentioning that among all the data acquired during the three days of each experiment, the period between 24 and 48h after the beginning is chosen for the analysis of temperatures and the heat fluxes in this thesis. This duration of 24 hours corresponds to the second day of each experiment. As a matter of fact, the first day is considered as the time lapse needed to reduce the impact of the initial conditions on the experiments (e.g., the temperature of the model envelope, especially the massive element, i.e. the slab). Moreover, the temperatures seem to be homogenized in the second day because the variation of the temperature in the room during days 2 and 3 is quite similar, as Figure 3.1 shows. Finally, in order to have results assessing the cooling potential of the different studied cases and to compare them with the results of Lança et al. [37], data from the three days of the experiments will be used, as discussed later.

The evolution of the difference between the temperature of the air and the temperature of the laboratory measured by all the TCs from the six columns is plotted in Figure 3.2. Instant “0” in Figure 3.2 refers to the beginning of the HP, i.e., 8:00 a.m., when the electrical resistance is turned on,

while “12” corresponds to the end of the HP and the beginning of the CP, i.e., 8:00 p.m., when the fan is turned on. Finally, “24” represents the end of the CP. With the exception of the deficient ones, all the TCs from the six columns were reported. Indeed, there are six graphs in Figure 3.2, one for each column. For the record, the first digit of a TC reference number identifies the column to which it belongs, while the second digit is related to the height at which a TC is located in its own column.

Firstly, the 24-hour period of Figure 3.2 allows visualizing that the values of the slopes of the curves are higher during the first 2 hours of the HP. Then, during the 10 following hours, the rate of increase of temperatures slows down progressively as steady state conditions approach. At 8 p.m., the electrical resistance is switched off and the fan starts to apply a forced ventilation to the previously heated reduced model. This marks the end of the HP and the beginning of a 12-hour CP, which manifests itself in an abrupt fall of temperatures at instant “12” in Figure 3.2.

Secondly, in all the graphs, the end of the HP is visible with approximately constant values of ΔT, and in general TCs situated above the SC have reached higher values of ΔT than the ones below the SC. This is clearly visible in columns n°1, 4, 5 and 6. This means that the peripheral gap between the SC and the walls is large enough to let the plume passing through it and rising until it reaches the plenum. Results from column n°2 show that TCs 22 and 23 achieve lower temperatures than other TCs placed at the same height in different columns. This might be explained by the fact that those two TCs are positioned just in front of the air inlet opening, so, even when the fan is not turned off, ambient air can enter the enclosure and cool them.

Thirdly, during the first 1,5 hours of the CP, differences about the curves can be observed. For example, in the column n°1 it is possible to see that TCs 11 and 12 have lower ΔT values, meaning that they are cooling faster. Similarly, the two columns, n°2 and 5, situated in the middle of the reduced scale model, are cooling down faster above the SC than below it. This is probably due to their position just in front of the air flow, see Figure 3.3. They benefit directly from the cool ambient air. In short, this analysis shows which zone of the model - below the SC, i.e., the occupation zone, or above the SC, i.e., the plenum - is warmer during the day and is cooling faster during the night, for each column. Moreover, after approximately 3,5 hours of NV, all the TCs have a ΔT lower than $1°C$. At the end of an entire cycle, i.e., when 24 hours have passed, the temperatures of the enclosure, whether they are from the plenum or the occupation zone, and of the laboratory are almost the same (ΔT≈0). This indicates that an effective cooling mechanism has occurred.

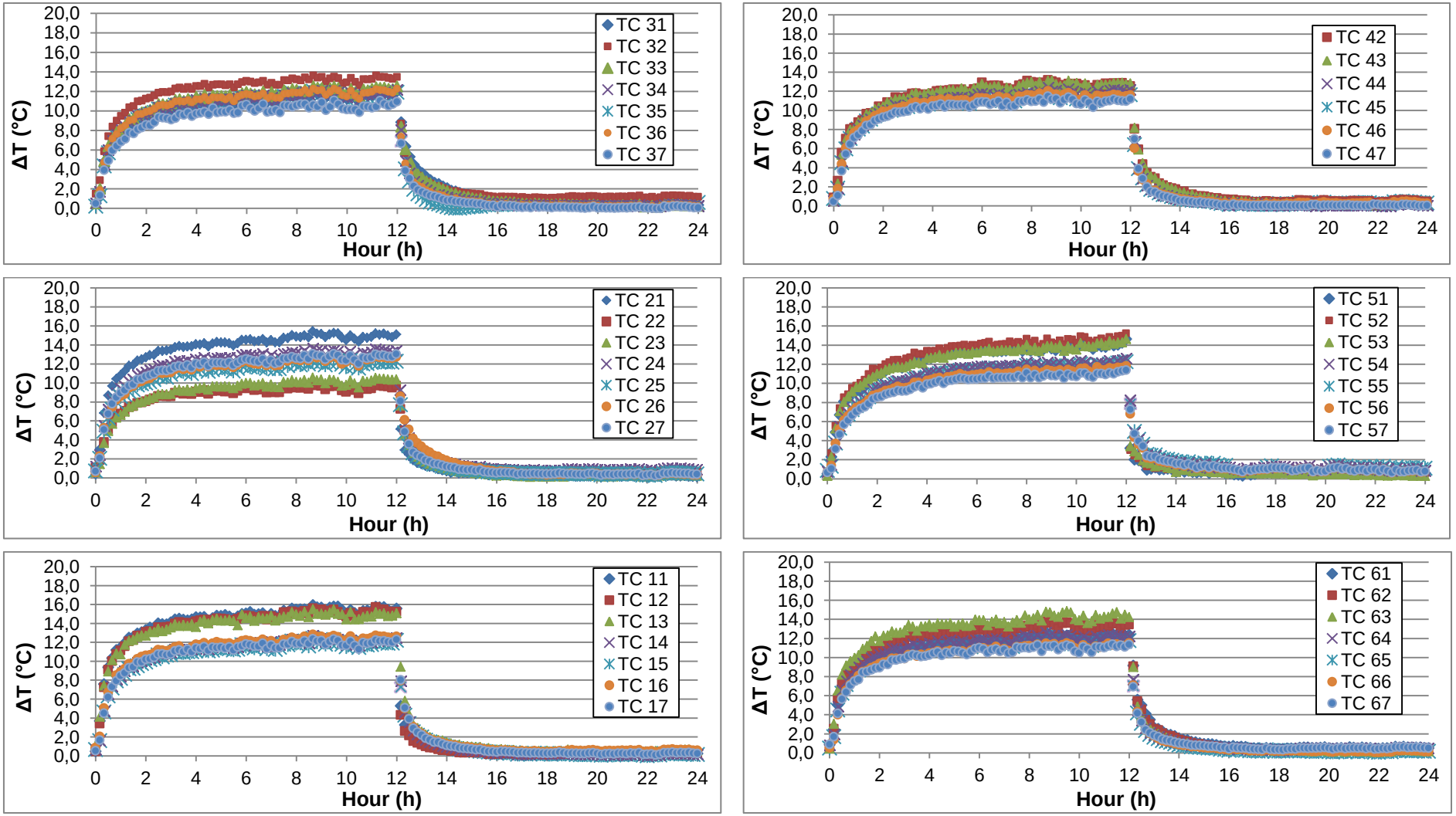

Figure 3.2 - Evolution of the difference between the temperature of the air temperatures from thermocouples positioned in the six columns and the temperature of the laboratory, during the second day of the experiment O1-100-C-1.

In order to process the data more easily, the evolution of the difference between the temperature of the air and the temperature of the laboratory, measured by only four TCs during the second day of the test, was plotted in Figure 3.4. Out of the four TCs, two are placed above the SC, TCs 42 and 43, and the others are in the occupation zone, TC 44 and 47. As a reminder, the column n°4 is located at $x = 2L_x/3$ and $y = L_y/4$, see Figure 3.3.

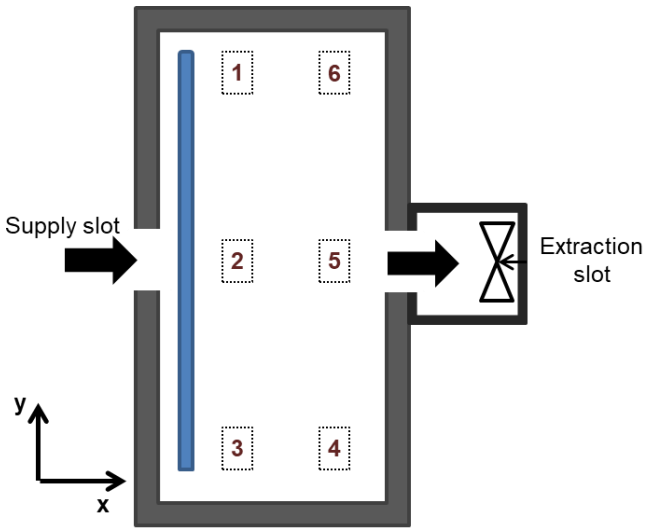

Figure 3.3 - Schematic of the experimental set-up with the location of the columns of thermocouples.

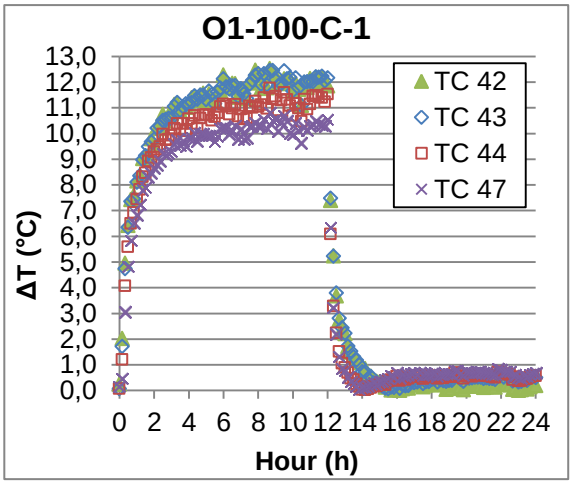

Figure 3.4 - Evolution of the difference between the temperature of the air and the temperature of the laboratory measured by four thermocouples of column n°4, during the second day of case O1-100-C-1.

Figure 3.4 confirms that using the C type of SC causes higher ΔT values in the plenum than in the occupation zone, during the HP. This is due to the buoyancy phenomenon. For example, TC 47, which is placed at the lowest height in the reduced scale model, achieves lower values of ΔT. This type of figure will be used to compare the different cases of SC type in the next section.

In order to analyze the air temperatures inside the room from a different point of view, Figure 3.5 displays the values of ΔT obtained by all the TCs measuring the temperature of the air inside the room. These data were taken 2 hours after the electrical resistance is turned on, so at the beginning of the HP. As the chart legend indicates, each column of TCs is represented by a symbol. Note that as explained before, TCs with their second digit being 1, 2 and 3 are placed above the SC represented here by the horizontal dashed line.

Figure 3.5 shows that the SC gap ensures a relatively homogeneous temperature profile in the occupation zone because the TCs below the SC have ΔT values between $7{,}8$ and $10{,}5°C$. Above the SC, the variation in ΔT is larger, ranging from $8{,}2$ to $13{,}6°C$. Again, it can be noticed that, in the plenum, the second column reveals lower ΔT values, probably because it heats more slowly due to its location in front of the air inlet opening.

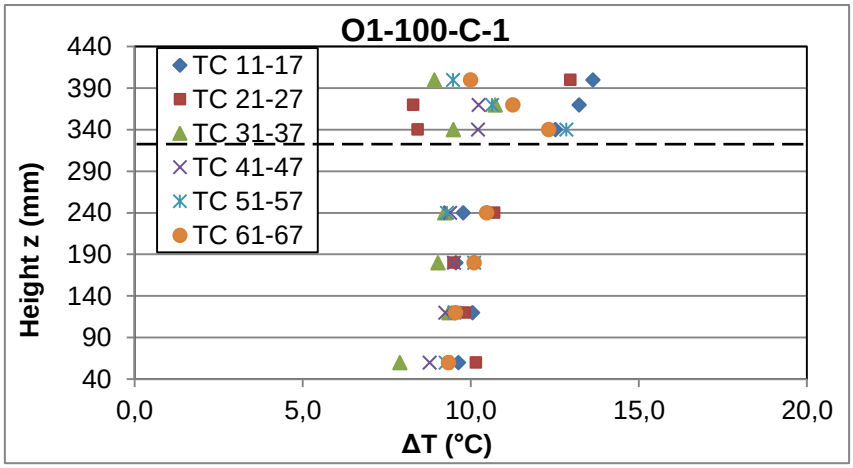

Figure 3.5 - Difference between the temperature of the air and the temperature of the laboratory for the experiment O1-100-C-1, 2 hours after the electrical resistance is switched on (data from the second day). The horizontal dashed line indicates the position of the SC.

Note that the choice of acquiring the values of ΔT 2 hours after the electrical resistance is turned on was based on several arguments. First, it is connected with the observation of the measured heat fluxes at the lower surface of the slab, which will be discussed later. In fact, when the electrical resistance is turned on and starts to heat the enclosure, the heat fluxes decrease sharply and attain approximately steady values 2 hours after. Secondly, it is possible to see in Figure 3.1, that as already mentioned, this moment corresponds to a marked decrease of the slope of the ΔT profile for TC 64, as well as in other similar profiles shown above in Figures 3.2 and 3.4. Thirdly, the TC reading the evolution of the temperature of the resistance confirms that after 2 hours of heating, the transient state is over and the steady state is approaching, see Figure 3.6.

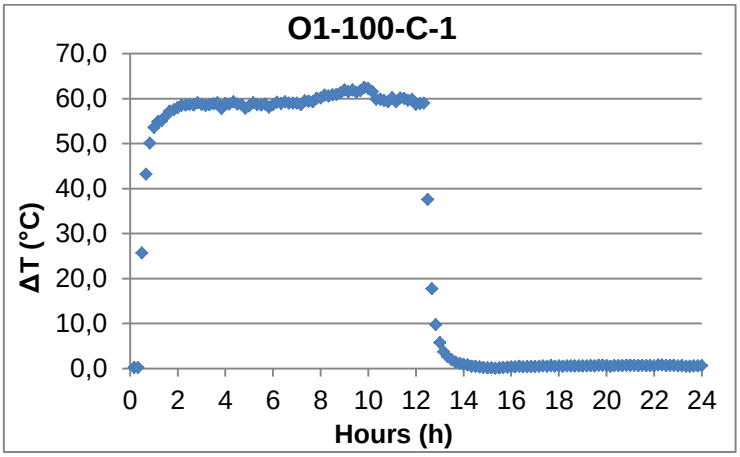

Figure 3.6 - Evolution of the difference between the temperature of the resistance and the temperature of the laboratory measured by a thermocouple during the second day of the experiment O1-100-C-1.

Another possibility to treat the results is to plot in the same graph the data retrieved from the six TCs placed at the same height. For example, Figure 3.7 represents the evolution of the values of ΔT of all the TCs with their second digit being 1, i.e., the TCs closest to the slab. Here, only the period

from 11 to 14 hours of the second day of the test O1-100-C-1 is displayed in Figure 3.7. This zoom enables to take a closer look at the end of the HP and the transition to the beginning of the CP. Here, TCs from columns n°1 and 2 reach the higher ΔT values during the HP and then the lower ones during the CP, together with the TC from column n°5, which means that they cool down faster than the others.

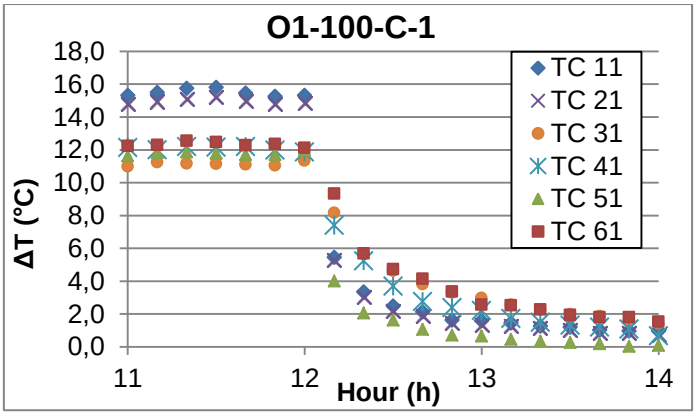

Figure 3.7 - Zoom in the evolution of the difference between the temperature of the air temperatures from TCs 1 positioned in the six columns and the temperature of the laboratory, during the second day of the experiment O1-100-C-1.

Similarly, it can be noted that TCs with their second digit being 4, 5, 6 or 7 cool homogeneously in the model because there is no noticeable difference between the six columns for the same height. For example, in Figure 3.8, there is no significant disparity in the values of ΔT from the TCs with their second digit being 4, of all the six columns, neither during the HP nor during the CP. So, for the case O1-100-C-1, the occupation zone cools down evenly according to the height where the TCs are located, whereas in the plenum, two TCs placed at the same height can have different cooling rates, as seen in Figure 3.7. In addition, in Figure 3.7, the TCs 1 from columns n°3 and 4 show lower values of ΔT than the other TCs at the same height. This can be explained by the fact that the electrical resistance is not centered in the room. It is closer to the wall on the side of column n°1. In other words, the reduced scale model is unsymmetrical.

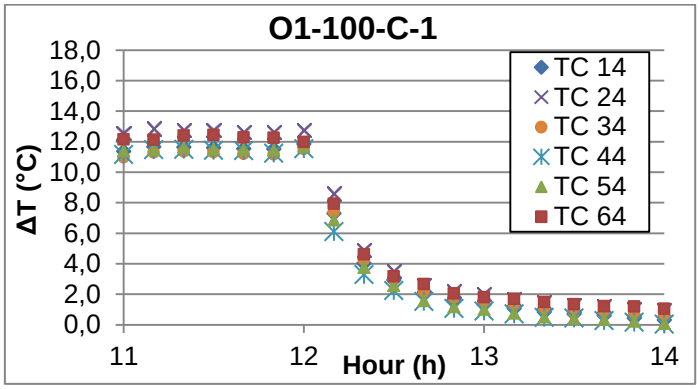

Figure 3.8 - Zoom in the evolution of the difference between the temperature of the air temperatures from TCs 4 positioned in the six columns and the temperature of the laboratory, during the second day of the experiment O1-100-C-1.

In order to evaluate more accurately the effectiveness of the night cooling strategy in terms of the influence of the different peripheral gaps, the difference between the average air temperatures achieved at the end of the HP and at the end of the CP is calculated for each case using the definition given by Lança et al. [37]:

$$\Delta\bar{T}_{HC} = \sum_{k=1}^{3}\sum_{i=1}^{10}\frac{\Delta T_{ik}}{30} - \sum_{k=1}^{3}\sum_{j=1}^{10}\frac{\Delta T_{jk}}{30} \tag{3.1}$$

where subscript k denotes the day under consideration, and subscripts i and j identify measurements in the heating and cooling periods, respectively. The summations extend for the three days of every experiment and account for the last ten TC readings during the heating and cooling periods, which correspond to the first and second terms on the right side of the equation. TC 64 was again chosen to compare the results. For the test considered here, O1-100-C-1, Equation (3.1) gives $\Delta\bar{T}_{HC} = 11{,}55°C$. This means that between the end of the HP and the end of the CP, the difference between of the air temperature measured by TC 64 and the laboratory temperature decreased by about $11{,}55°C$. This tool will be useful to compare the results of the cases using different types of SC, in the next sections.

To analyze the CP, Figure 3.9 displays the values of ΔT obtained by all the TCs measuring the temperature of the air inside the room, but this time the data were taken 30 minutes after the fan is turned on, i.e., at the beginning of the CP.

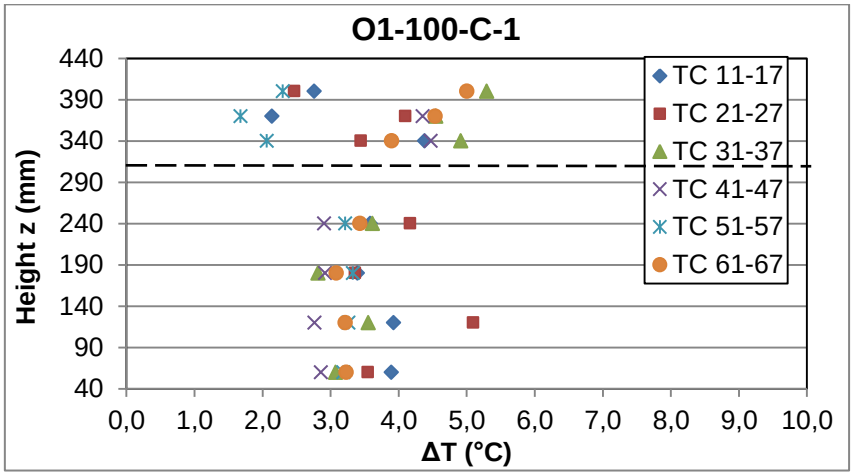

Figure 3.9 - Difference between the temperature of the air and the temperature of the laboratory at 30 minutes after the beginning of the cooling period for all the thermocouples. The horizontal dashed line indicates the position of the SC.

The comparison of the two Figures 3.5 and 3.9 (i.e. the one for HP and the one for CP) enables to tell that NV induces less homogenized temperature profiles than the buoyancy flow, occurring during daytime. In fact, Figure 3.9 depicts a large range of values of ΔT extending from $1{,}6°C$ read by TC 52 to $5{,}3°C$ reported by TC 31. It was expected that the TCs placed above the SC cool down faster than the others because the opening is situated above the SC. However, as Figure 3.9 shows, it is not

always the case and each column has a different profile. Once again, it is possible to say that TCs 21, 22, 23, 51, 52 and 53, cool down relatively fast because they directly benefit from the air flow. Concerning the TCs positioned above the SC, it can be noticed that the ones closer to the slab, i.e., which have 1 as their second digit in their reference number, always register higher values of ΔT than the two others in the same column. For example, TC 61 measures a value of ΔT of $5°C$, 30 minutes after the beginning of the CP, while TC 62 assesses $4{,}54°C$, and TC 63 reads $3{,}89°C$. This may be because the slab, that stored the heat during daytime, is now releasing it thanks to the NV, and heating the TCs closer to it. Note that this phenomenon is visible in all the columns with the exception of column n°2.

3.1.3. Slab temperatures

It is important to keep track of the temperature of the slab. In fact, it represents the thermal mass of the building, so its ability to buffer heat during the day, and release it at a later time, has to be validated. For that purpose, the evolution of the difference between the temperature of the slab and the temperature of the laboratory during the second day of the experiment O1-100-C-1 is plotted in Figure 3.10, for two different TCs, S8 and S17, described in chapter 2. The results are again shown for a heating power of $100\ W$, and for a 7,5% x 10% peripheral gap.

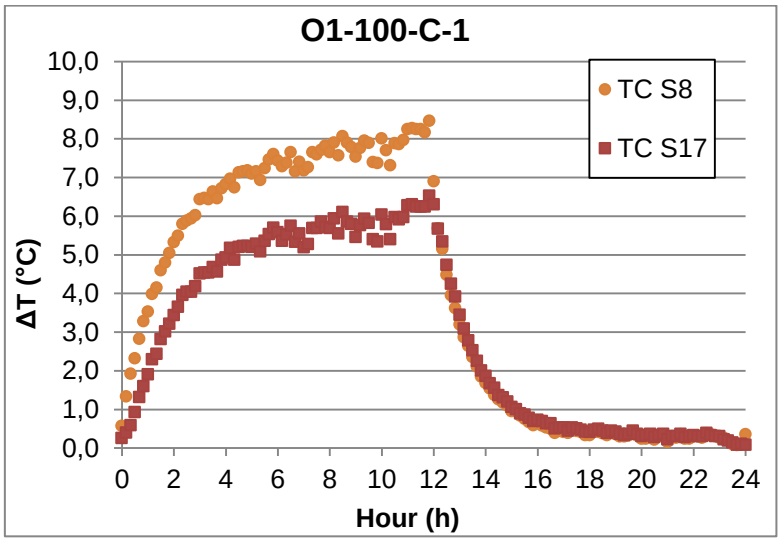

Figure 3.10 - Evolution of the difference between the temperature of the slab and the temperature of the laboratory for two thermocouples located at $x = L_x/2$ and $y = L_y/2$ and placed at the lower surface of the slab (S8) and in its interior (S17), for the test O1-100-C-1.

Firstly, just like for the air temperatures, the maximum temperatures are achieved by the end of the heating cycle. Secondly, as expected, Figure 3.10 depicts lower temperatures in the interior of the slab than at its inner surface, during the HP, with a difference between the peak temperatures measured by S8 and S17 of $2°C$. Finally, at the end of the CP, the two TCs display differences of

temperatures close to $0°C$. This means that the slab is now at the same temperature than the laboratory. So, it has been efficiently cooled down by the ambient air passing through the model at nighttime. Moreover, the slab core temperature drops by $6{,}5°C$ in only 6 hours of night cooling operation. Consequently, it proves once again that NV is a suitable strategy in this case.

Concerning the analysis of the CP, a zoom in the precedent results, showing only the last hour of the HP and the first part of the CP in Figure 3.11, confirms that, as expected, the air flow entering in the plenum attains first the inner surface of the slab. As a matter of fact, during the first 10 minutes of the CP, the ΔT value of TC S1 decreases from $8{,}5$ to $6{,}8°C$, whereas ΔT value of TC S2 stagnates around $6{,}3°C$. Nevertheless, during the rest of the CP, there is no significant difference in the cooling rates of those two TCs, despite the fact that the temperature of the slab core is always slightly lower than the inner surface.

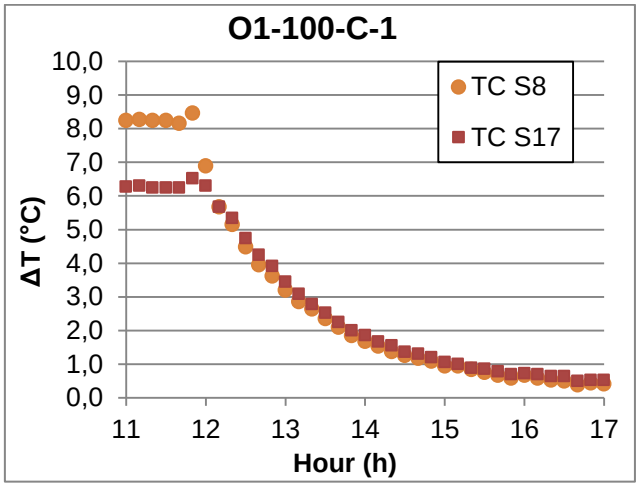

Figure 3.11 - Evolution of the difference between the temperature of the slab and the temperature of the laboratory for two thermocouples located at $x = L_x/2$ and $y = L_y/2$ and placed at the lower surface of the slab (S8) and in its interior (S17), for the period 11 to 17 hours of the second day of the test O1-100-C-1.

Other TCs placed inside the slab, at different y and z coordinates, are used to analyze how the slab is heated by the plume created by the electrical resistance. Their exact position in the slab is presented in Figure 2.9, in chapter 2. Figure 3.12 reveals that TCs attached to the middle of the slab, which are TCs 23, 17 and 20, attain higher ΔT values than the ones located on the sides. In fact, from the electrical resistance emanates an upwards convective flow called thermal plume. The differences in the ΔT values read by the TCs in the slab core are probably due to higher peripheral losses of the slab. Moreover, it can also be noticed that it exists an edge effects of the thermal resistance. In other words, the plume is diluted at the borders because of the gaps between the side walls and the ends of the resistance. Actually, the latter does not extend from one side of the room to another, since it is only 1 meter long, so the sides of the model do not benefit from as much heat as the middle part. So, the thermal plume seems unsymmetrical, and results in the uneven thermal heating of the slab. What is

more, the shape of the thermal plume and the air velocity are due to the pressure differences generated by the temperature differences, caused by the heat source, i.e., the buoyancy-induced flow.

In addition, Figure 3.12 shows that the temperatures at the inner surface of the slab at $x = L_x/2$ are quite homogeneous. In fact, whatever their position along the y axis, the peak temperature reaches $8°C$. This observation is not consistent with the effect of the thermal plume depicted above. However, it demonstrates the thermal capacity of the concrete slab because it is able to absorb heat during the day. As a matter of fact, once the TCs placed inside the slab are considered, a marked diminution is observed with the ΔT values decreasing from $8°C$ to 5 or $6°C$.

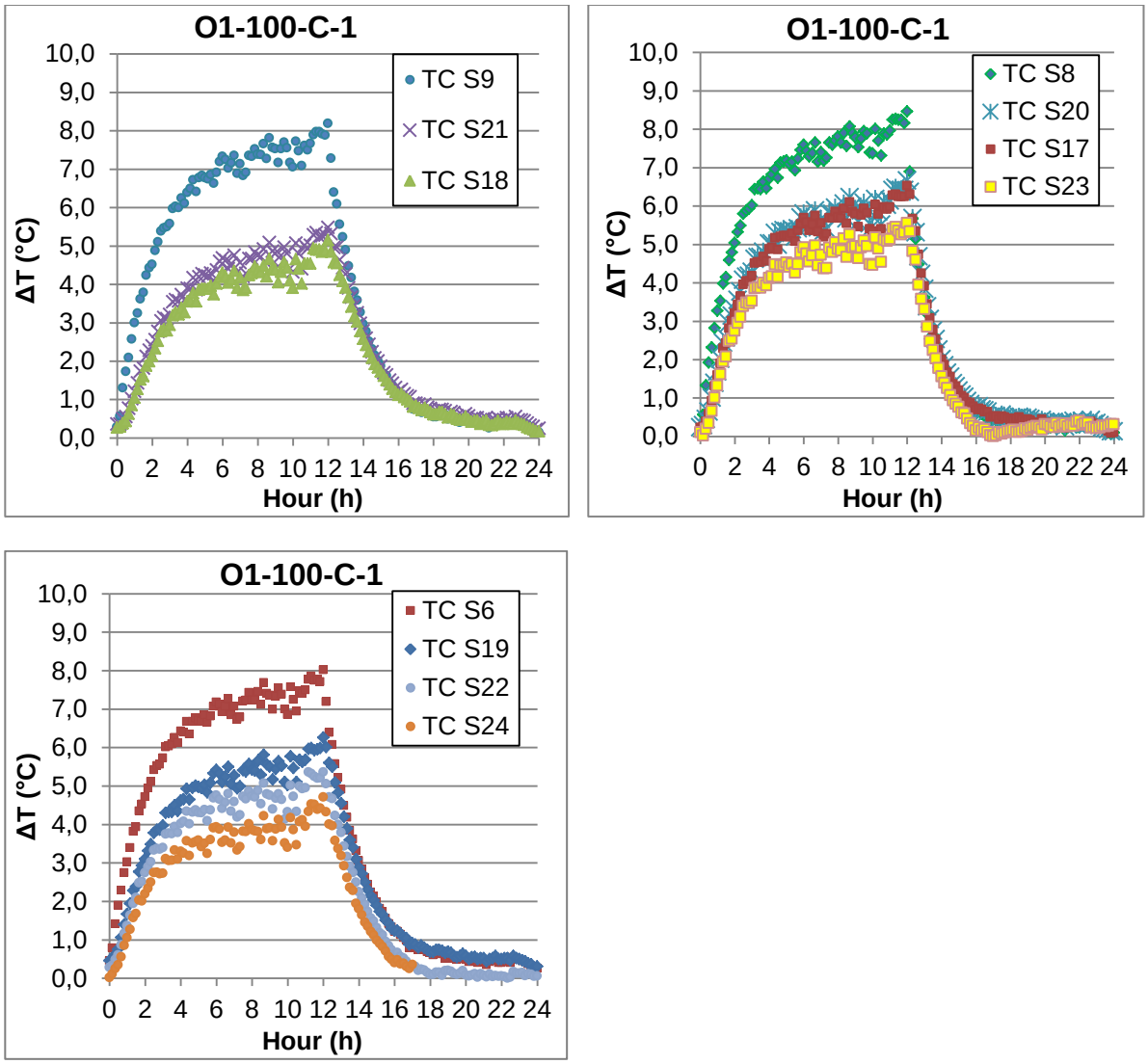

Figure 3.12 - Evolution of the difference between the temperature of the slab and the temperature of the laboratory for TCs placed inside the slab and at its surface, during the second day of the test O1-100-C-1.

To better understand the heating of the slab, Figure 3.13 plots two graphs. The first one shows ΔT values of three TCs having different positions along the x axis: TC S4 is placed at $x = L_x/4$, TC S9

is at $x = L_x/2$ and TC S14 at $x = 3L_x/4$ (see Figure 2.8, in chapter 2). As expected, TC S4, which is the closest to the electrical resistance, reaches higher temperatures. This shows that the thermal plume rises from the electrical resistance to the slab, after passing through the peripheral gap. After reaching the top of the enclosure, it spreads horizontally and progressively heats the slab following the x-axis but with a decaying intensity. That is why, TC S9 and S14 display lower values of ΔT than TC S4. The thermal plume transfers its heat to the slab. The second graph in Figure 3.13 also shows TCs situated at the inner surface of the slab, but this time, they have the same x coordinate, i.e., $x = 3L_x/4$, and different positions along the y axis. During the HP, the TCs giving the highest values of ΔT are, in order, TCs S12, S13 and S14. This can be explained by the fact that the thermal plume is expected to be more concentrated in the middle of the reduced model, because, as already said previously, stronger convective heat transfer is caused by the electrical resistance. Also, TC S11 reads higher temperatures than TC S15, because the electrical resistance is closer to the wall which is near to TC S11. Concerning the CP, TC S13 is clearly cooling faster than the others. As a matter of fact, it is located at $y = L_y/2$, i.e., just in front of the air outlet opening.

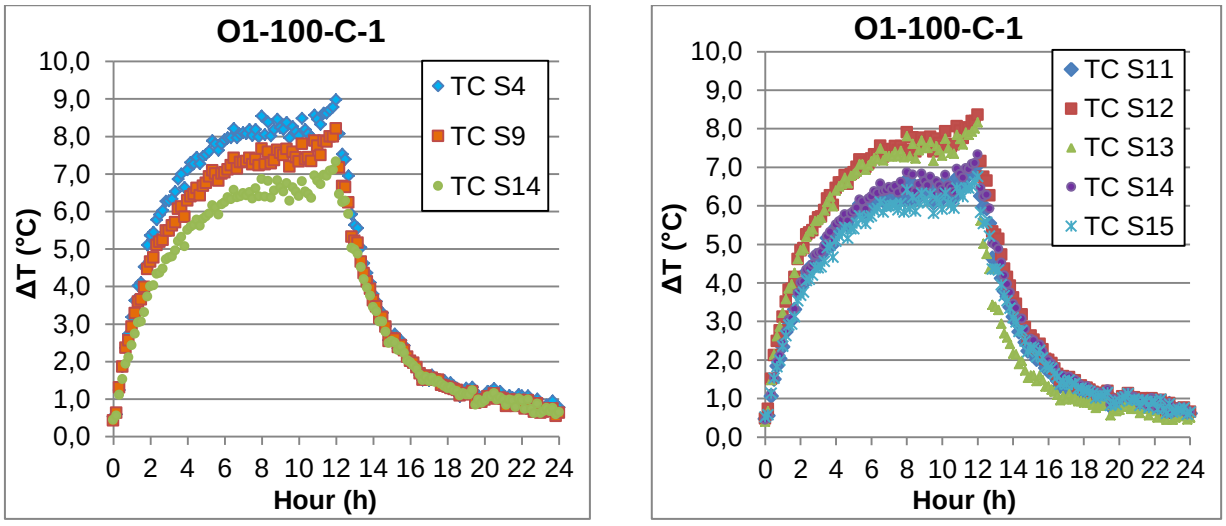

Figure 3.13 - Evolution of the difference between the temperature of the inner surface of the slab and the temperature of the laboratory for three thermocouples, during the second day of the test O1-100-C-1.

3.1.4. Heat fluxes

As already described in chapter 2, two heat flux sensors, F1 and F2, measured the heat flux transferred by conduction through the slab. Since F1 is located next to the supply slot, it is just above the heat load and, as a consequence, it registers higher heat fluxes than sensor F2, during both the heating and the cooling periods. Thus, Figure 3.14 only presents the results obtained with F1. Again, only the measurements from the second day are considered for this analysis.

In Figure 3.14, the HP and the CP are quite distinct. At the beginning of the HP, the heat flux measured by F1 decreases during almost 2 hours, before reaching a steady state. Also, during the entire HP, i.e., from instant “0” to “12”, the values of the heat flux are negative in the chart meaning that heat is transferred from the interior of the model to the slab. Then, as soon as the fan is turned on and the electrical resistance stops heating the model, a sudden peak is visible in the heat flux profile, along with a change of sign. A forced convection heat transfer mechanism is now taking place. So, during the CP, i.e., from instant “12” to “24”, all the values are positive because heat is transmitted from the slab to the enclosure. In fact, heat was stored in the slab during the day and it is now removed by the NV. Note that there are losses through the walls and the slab from the model to the laboratory. Moreover, the same way it has been said that a steady state is reached 2 hours after the beginning of the HP, it can be noted that 4 hours after the beginning of the CP marks a decrease of the slope of the heat fluxes. Indeed, during the first 4 hours of the CP, the heat flux falls down abruptly by $65\ W/m^2$, whereas it decreases by $7\ W/m^2$ during the 8 following hours.

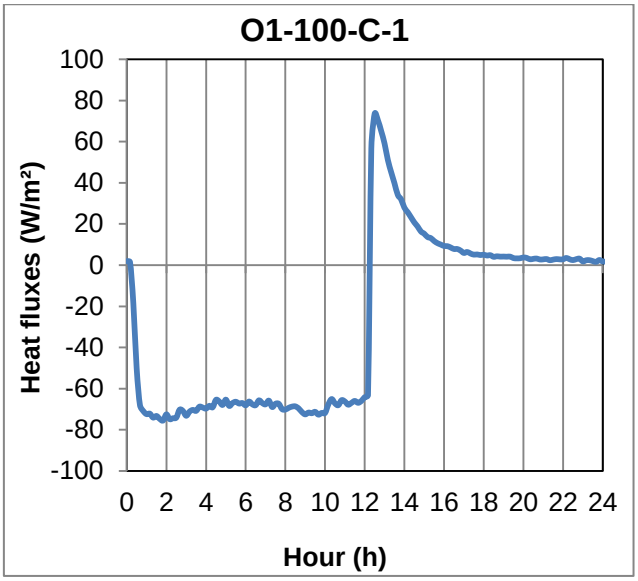

Figure 3.14 - Heat fluxes measured at ($x = 150\ mm, y = L_y/2$) during the second day of the test O1-100-C-1.

Finally, the heat fluxes are close to $0\ W/m^2$ at the end of the CP. This indicates that no more heat exchange is occurring between the slab and the enclosure. In other words, all the heat stored by the slab during the HP has been removed by the NV. This observation is in agreement with the measured values of ΔT of approximately $0°C$ during the last hours of the CP, as shown in Figures 3.2, 3.4 and 3.12. In addition, this is achieved with even lower velocities than the one used by Lança et al. [37]. So, the mean air speed of $1{,}1\ m/s$ is high enough to cause an intense convective heat exchange, which also demonstrates an efficient cooling mechanism of the slab. However, it is unclear if the heat flux would also be negligible at the end of the CP in a full scale compartment with such a low air velocity at nighttime.

3.2. Comparison between different cases

The results of the sixteen cases, with the openings located above the SC, are presented and compared in this paragraph. It may be recalled that two mean air velocities ($1{,}1$ and $2{,}05\ m/s$), two heat loads (62 and $100\ W$), and four different configurations of SC (SC without gap, SC with 2,5% x 2.5% and 7,5% x 10% gaps, as well as no SC) are considered.

3.2.1. Influence of the peripheral gap between the SC and the walls

One of the aims of the present work is to assess the influence of the peripheral gap of the SC on the effectiveness of the NV with a SC. So, this section underlines the differences obtained when the type of SC is changed.

3.2.1.1. Air temperatures during the HP

In order to easily compare the results of the present work with that of Lança et al. [37], the same type of graphs that has been used is plotted in Figure 3.15, which shows results for all the tests with a heat load of $100W$(see in Appendix C, Figure C.1, for the results from tests with $62W$).

In Figure 3.15, the cases D, without SC, show thermal stratification during the HP, since the temperature increases with the height, from the floor to the slab. TCs 1 have the higher ΔT values around $9{,}4$ to $14°C$. The results from the cases A, with complete SC, also reveal thermal stratification, but, this time, from the floor to the SC. As a matter of fact, in those cases only the occupation zone is heated by the electrical resistance, so, the area receiving the thermal plume is smaller and the temperatures achieved below the SC are generally higher. Consequently, the higher ΔT values are displayed by TCs 4, which are located just below the SC, and are around $14{,}2$ and $16°C$, for example for the case O1-100-A-1. Regarding the TCs situated above the SC in cases A, they receive heat that has been transferred through the SC, so they give lower ΔT values down to $5{,}6°C$. From a holistic view, i.e. putting aside the anomalies (TCs that measured temperatures too different from the others), during the HP, the cases A have higher values of ΔT in the occupation zone, whereas for the cases D it is the opposite, the higher values are measured in the plenum. In addition, the relevant results for the cases D, matching with the analysis from Lança et al. [37], show that the anomalies obtained in the other tests, such as TCs 32 and 62 in cases A, are due to the SC. For example, it is possible that the SC was not well centered on the room or that the cardboard used for the SC was bent at its borders by handling it. In such cases, the air would not circulate according to its expected air flow pattern leading to inconsistencies in the retrieved temperatures during the experiments. To sum up, the SC configuration has a huge influence in the air temperatures of the reduced scale model, during the HP. It can also be noticed that for all the tests, with the exception of cases A, column n°1 achieves slightly higher temperatures than those from column n°3, above the SC. For example, in the case

O1-100-B-2, TC 11 reaches $12{,}7°C$ while TC 31 approaches $9{,}6°C$. As already said in the previous section, this can be explained by the fact that the electrical resistance is not centered in the room.

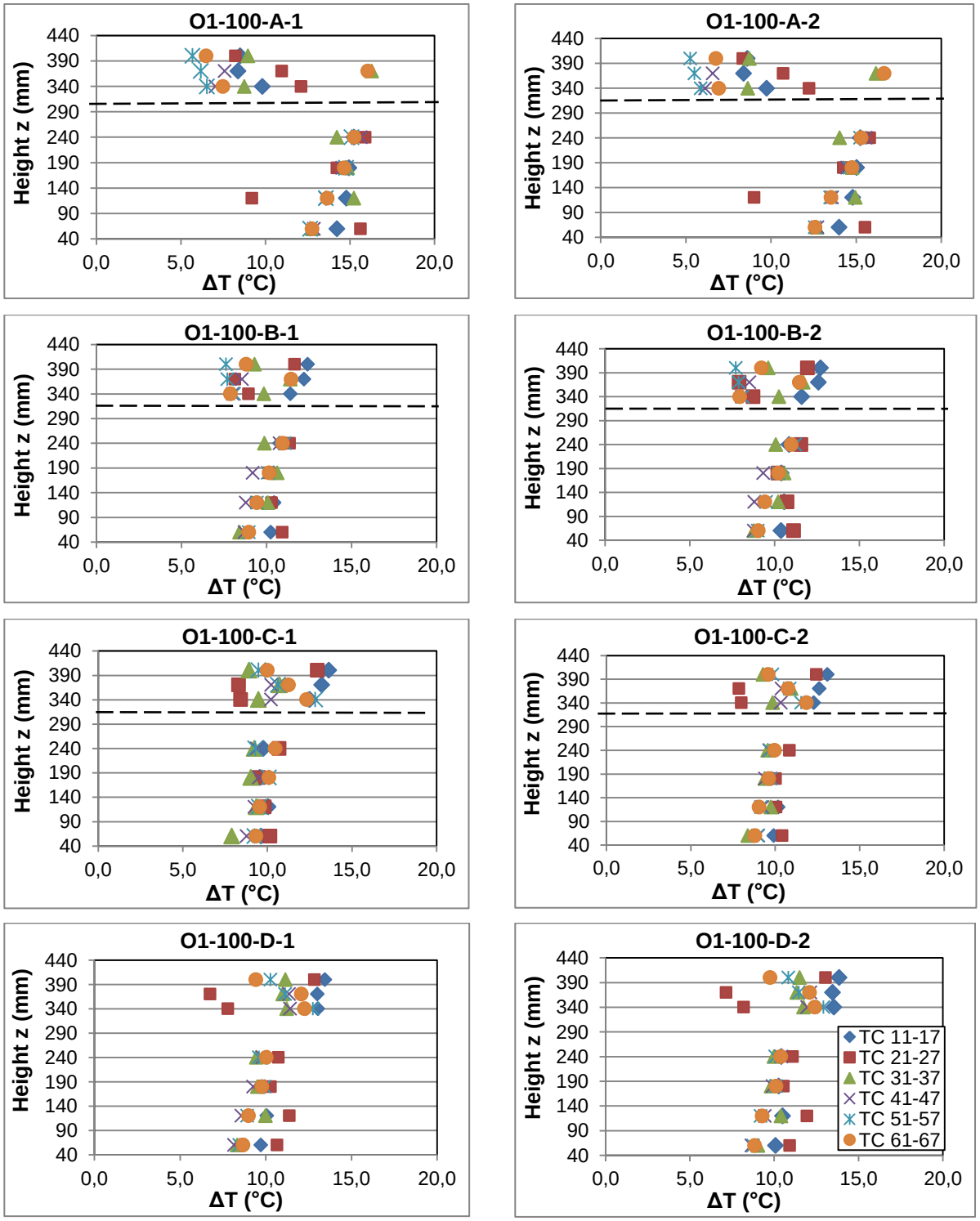

Figure 3.15 - Difference between the temperature of the air and the temperature of the laboratory from all the experiments with $100\ W$, data retrieved the second day, 2 hours after the electrical resistance is switched on. The horizontal dashed line indicates the position of the SC.

Another way to evaluate the influence of the peripheral gap during the experiments is to consider only four TCs, all placed in the same column. Column n°4 is chosen because it is not positioned in front of an opening for the ambient air. Two out of the four TCs are situated in the plenum and the other two are in the occupation zone. Figures 3.16 and 3.17 present the results for all the conducted tests.

Looking at the cases D presented in these figures, the thermal stratification is clearly visible with the highest temperatures, around $9°C$ for the $62W$ cases and $14°C$ for the $100W$ cases, achieved by the TCs located at the highest levels. In other words, the temperature increases with the height while the electrical resistance transfers heat to the whole enclosure (the occupation zone and the plenum). Regarding the opposite configuration, cases A, with a complete SC, the order of the TCs is inverted: now the warmest area is the occupation zone and the coolest one is the plenum. As already said, the hottest temperature is higher in these cases, around $12°C$ instead of $9°C$ for the cases with the lowest heat load and around $18°C$ instead of $14°C$ for the others, because the heated zone is smaller.

Regarding the configurations in between those extremum cases, which have peripheral gaps, the behavior is contrasted. The smallest gap with $100W$ is similar to the complete SC one, because TC 44 shows the highest value of ΔT. But its values is lower, meaning that warm air is passing through the peripheral gap which can be also seen by the plenum temperatures being slightly higher than in cases A. The other difference with cases A, is that TCs 42 and 43 are now as hot as TC 47 for the tests with $100W$ and ever hotter than TC 47 for the tests with $62W$. This is in agreement with the conclusion made by Lança et al. [37] saying that this configuration is the transition gap. In other words, the use of the SC with the smallest gaps allows the warm air to pass through the gap and reach the slab. Also, in the cases with the biggest peripheral gaps, the TCs have the same order than in cases without SC, i.e., the lower the TC is located, the lower its value of ΔT. However, with peripheral gaps the temperatures are much more homogenized. In addition, the value of ΔT achieved by TC 44, located at a human's head height, is a bit lower with a SC with bigger gaps than without SC.

The most important thing to notice in Figures 3.16 and 3.17 is that TC 44 is reaching higher values of temperatures with a complete SC than with SC with peripheral gaps, $3°C$ more when the heat load is $62W$ and $4°C$ when it is set to $100W$.

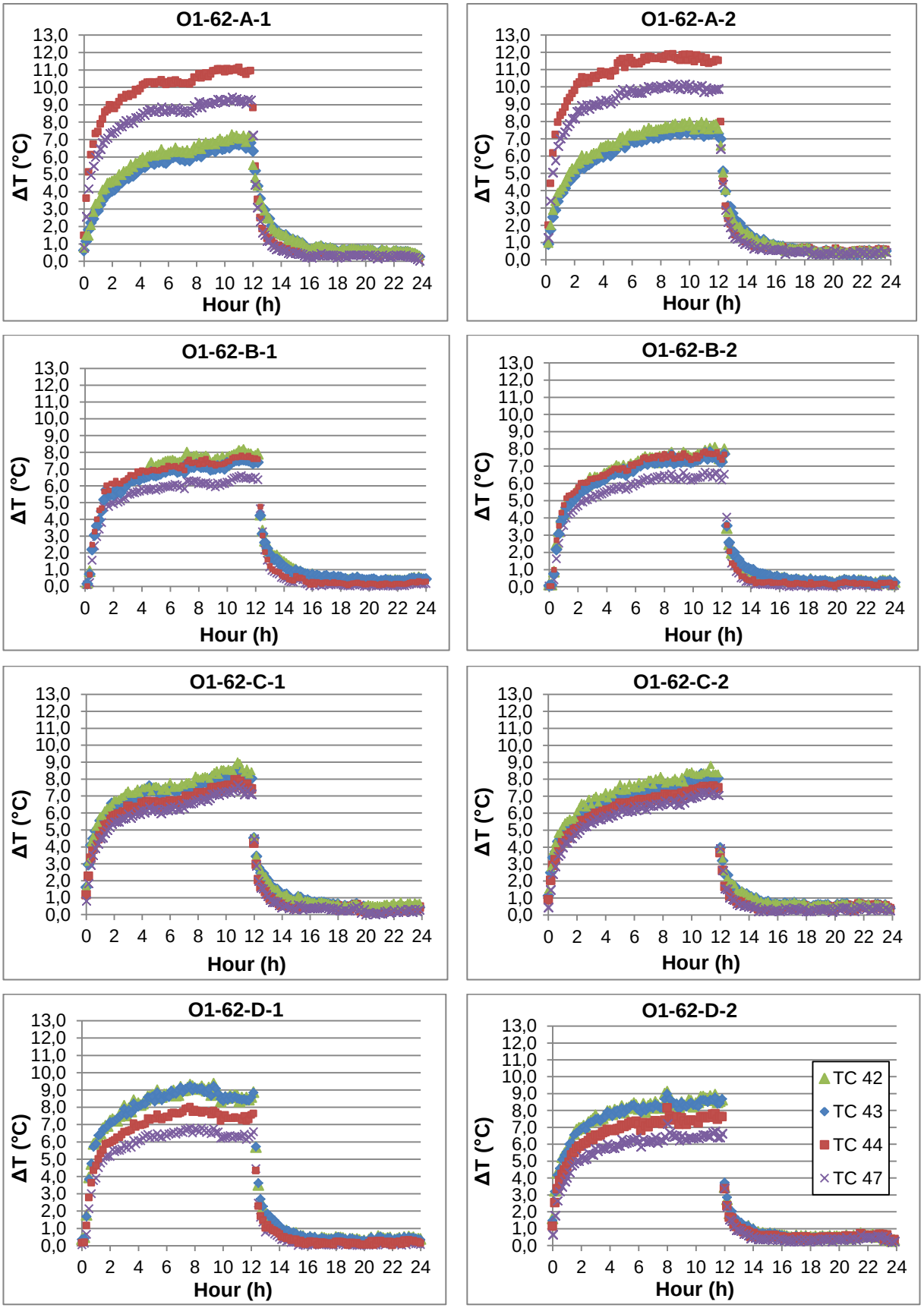

Figure 3.16 - Evolution of the difference between the temperature of the air and the temperature of the laboratory measured by four thermocouples of column n°4, during the second day of the eight tests with 62 W.

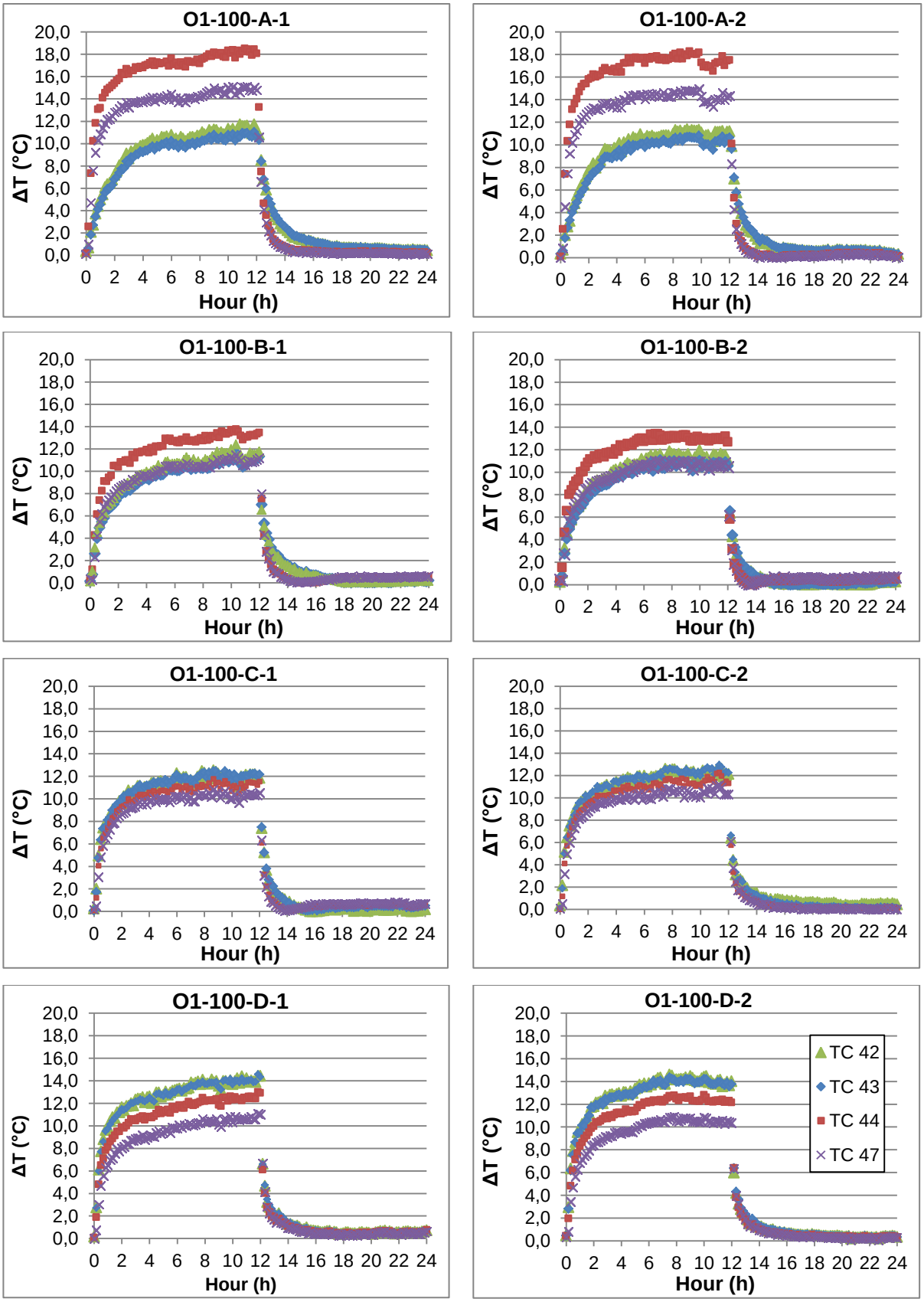

Figure 3.17 - Evolution of the difference between the temperature of the air and the temperature of the laboratory measured by four thermocouples of column n°4, during the second day of the eight tests with 100 W.

3.2.1.2. Air temperatures during the CP

To begin with, examining Figures 3.16 and 3.17 it can be noted that the air temperatures are much more uniform in all the enclosure during the CP than during the HP, for all tests. For example, in the latter Figures, the case O1-100-A-2 depicts a temperature difference between TC 43 and TC 44 of $8°C$ during 10 hours of the HP, against only $2°C$ during 2 hours of the CP. Consequently, it is harder to distinguish the curves from one another when the model is being cooled down by the fan, i.e., the CP is harder to comprehend. In fact, looking at the results for the tests conducted with $100W$ in Figure 3.18, there is no significant difference between the temperatures profiles from the different tests. In other words, no cooling pattern corresponding to each of the SC configurations can be identified during the CP. (See Appendix C, Figure C.2, for the results from tests with $62W$.) However, it can be noticed that, in general, the cooling seems to be more effective when there are gaps between the SC and the walls, because after the same amount of time being swept off by the airflow, the TCs give lower values of ΔT for these configurations. For example, in the cases with the SC types B, C or D the cooling is much more homogenized than for the cases with a complete SC with all the values of ΔT ranging until $4{,}2°C$ for test O1-100-C-2, 30 minutes after the beginning of the CP, while test O1-100-A-2 achieves values until $5{,}8°C$. So, the cooling air circulates more freely when there are peripheral gaps and even more in the absence of SC.

Again in relation to Figure 3.18, it is relevant to remark that, in all the cases, columns n°2 and 5 cool down faster above the SC, while the others see their values of ΔT decreasing more rapidly below the SC. This was expected because columns n°2 and 5 have their TCs above the SC being located in the middle of the reduced scale model, which is the main path of the air flow. Moreover, column n°1 often cools faster in the plenum than in the occupation zone. So, it also benefits from the cool wind. On the contrary, column n°3 always has lower temperatures below the SC than above it during the CP. Two possible explanations were found. Because the upper part of column n°3 is closer to the inlet wall and is situated at a corner of the model, it probably receives less cool air, or warm air coming from below is rising because of the density difference. It must be acknowledged that during the cooling phase the flow fields are difficult to predict because of the many phenomena occurring at the same time (stack effect, wind-induced ventilation, anomalies on the shape of the SC or its position in the model etc.). Also, in all the tested configurations of SC, temperatures of column n°4 decay faster below the SC. So, its upper part is not receiving directly the cool air because it is located on one side of the room and the TCs below the SC benefit from the air that passed through the peripheral gap between the SC and the side wall. Similarly, column n°6 generally cools down faster in the occupation zone. In short, the influence of the type of SC is less pronounced and visible during the cooling phase than during the heating one.

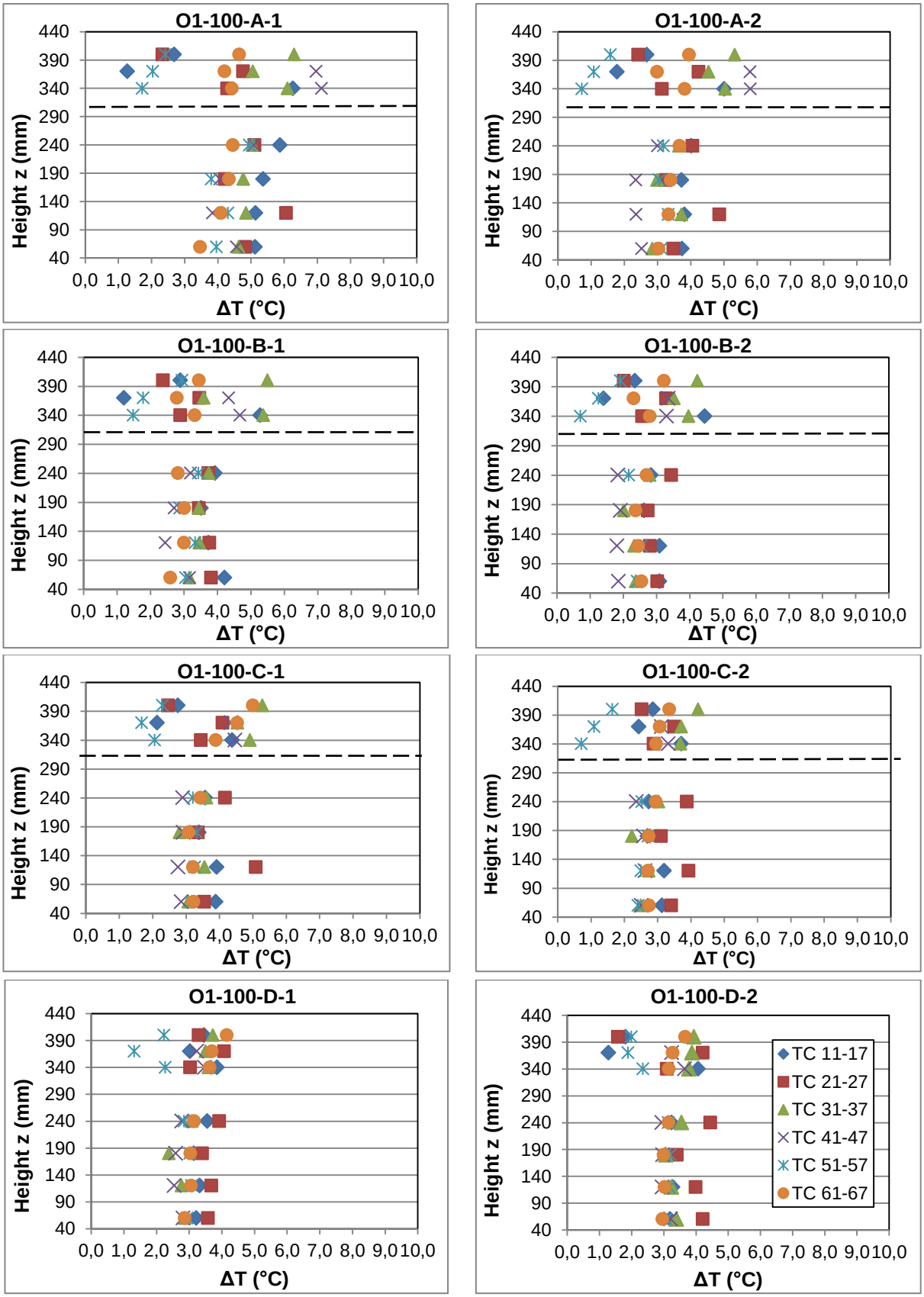

Figure 3.18 - Difference between the temperature of the air and the temperature of the laboratory at 30 minutes after the beginning of the CP for all the TCs of all the tests with 100 W. The horizontal dashed line indicates the position of the SC.

To evaluate the effectiveness of the night cooling strategy in terms of the influence of the different peripheral gaps, Figure 3.19 gathers the results of the computation of the difference between the average air temperatures achieved at the end of the HP and at the end of the CP for the sixteen cases, which was determine using Equation (3.1).

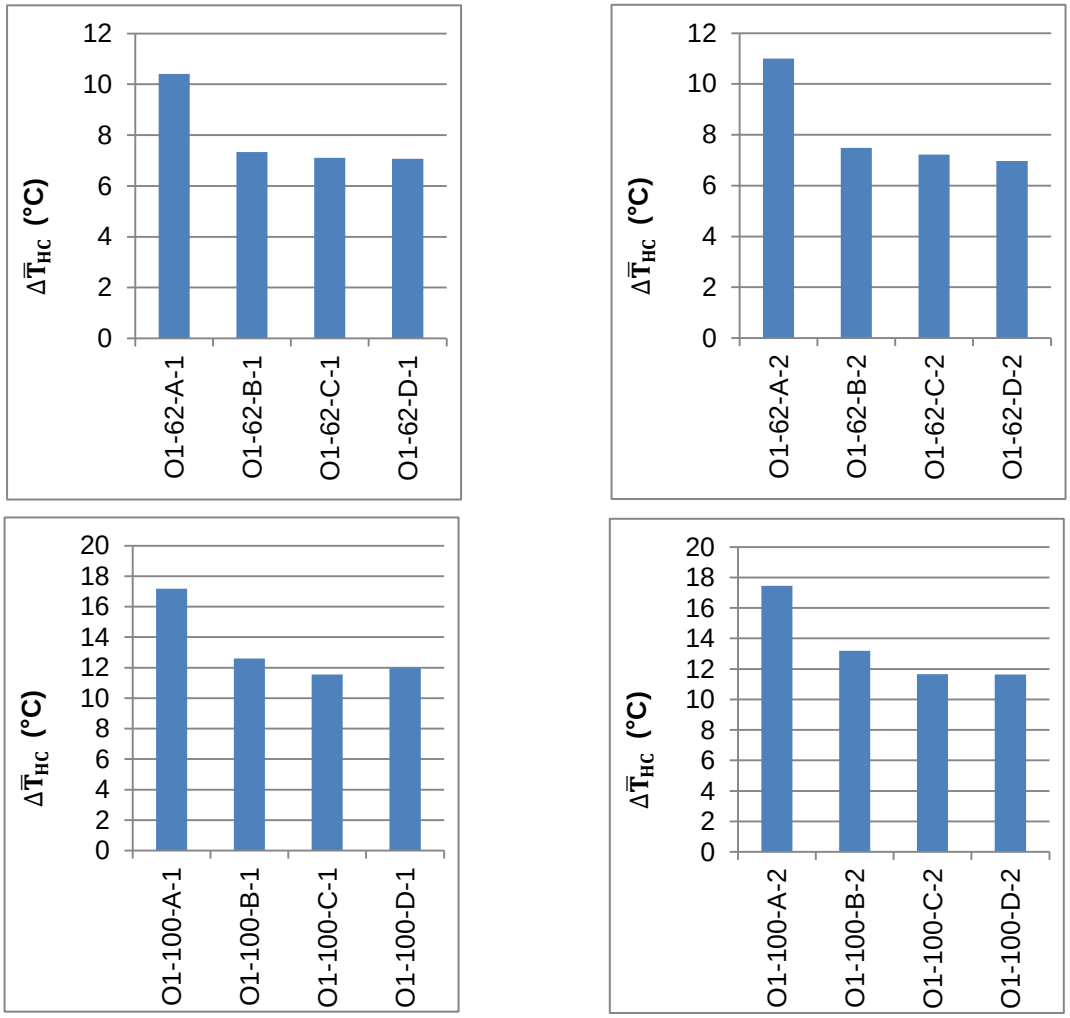

Figure 3.19 - $\Delta\bar{T}_{HC}$ Difference between the average temperatures achieved at the end of the heating and cooling periods for thermocouple 64 for all the tests.

The overall view of the charts in Figure 3.19 reveals that the variation of the temperature difference is larger for the cases with a complete SC than for the cases with SC not fully covering the slab. Taking the tests with a heat load of $100\,W$ and the air velocity 2 as examples, $\Delta\bar{T}_{HC}$ decreases significantly from $17{,}4°C$ without a gap to $13{,}2°C$ for the smallest gap. There is a corresponding decrease from $11°C$ to $7{,}5°C$ for the tests using $62\,W$ and velocity 2 again. In this respect, and in accordance with the results from Lança et al. [37], it is the proof that the gap between the SC and the side walls attenuates the peak temperatures, in the reduced scale model of the office. In fact, this feature enables the air to flow through the gap between the plenum and the occupation zone. It is also in line with the results reported above. In addition, as Lança et al. [37] noticed, even wider gaps, for a fixed heating power, yield smaller variations of $\Delta\bar{T}_{HC}$, in comparison with those mentioned above.

Actually, this further decrease of $\Delta\bar{T}_{HC}$ ranges around $0{,}27°C$ for tests with $62\,W$ and around $1{,}5°C$ for $100\,W$ with velocity 2, when the size of the gap increases from 2,5% x 2,5% to 7,5% x 10%. Between the two extreme cases (from the case A, complete SC, to the case D, without a SC), the decrease of $\Delta\bar{T}_{HC}$ is significant ranging from $4°C$ for $62\,W$ to $5{,}8°C$ for $100\,W$, when the velocity 2 is employed. Therefore, the results suggest once again that there is a critical gap size above which the air temperature field remains approximately the same. This is consistent with the results presented in Figures 3.16 and 3.17, and with Lança et al. [37] conclusions.

3.2.1.3. Slab temperatures

The graphs in Figures 3.20 and 3.21 illustrate that case A, which has a complete SC, differs a lot, during the HP, from the others with always lower slab temperatures, with a difference up to 1 and $2°C$ for the cases with 62 and $100W$ respectively. This can be explained by the fact that the complete SC reduces the heat transfer from the occupation zone to the plenum. So, less heat attains the slab, and the latter reaches lower temperatures.

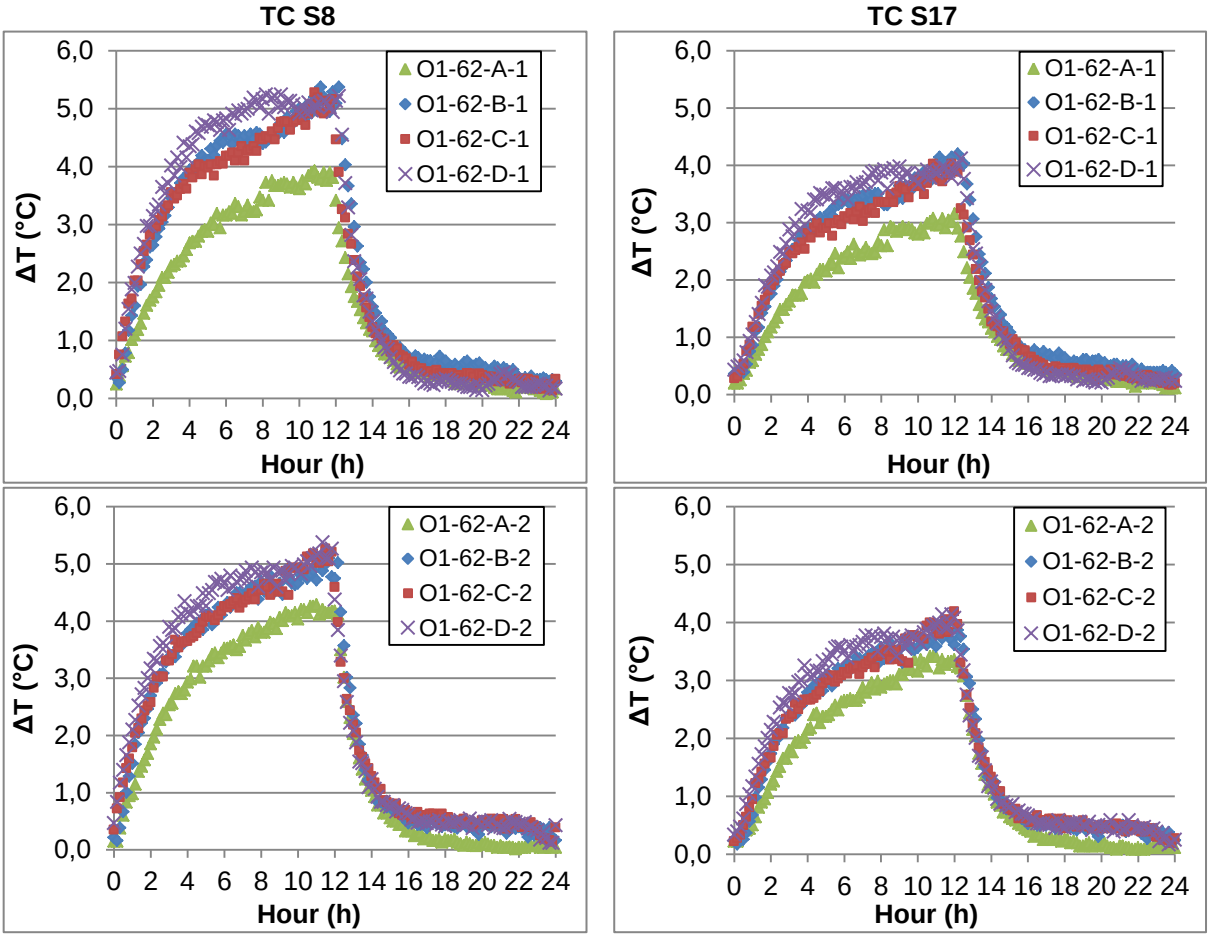

Figure 3.20 - Evolution of the difference between the temperature of the slab and the temperature of the laboratory for two thermocouples located at $x = L_x/2$ and $y = L_y/2$, and placed at the lower surface of the slab (S8) and in its interior (S17), for the tests with $62\,W$.

Concerning the slab temperatures, the smallest gap of 2,5% x 2,5% and the case without SC give similar results. This is in agreement with the heat fluxes analysis because higher heat fluxes are reported when SCs with gaps are used, as it will be discussed in the following section and this is expected to raise the slab internal temperatures. In fact, the heat produced by the electrical resistance rises and pass through the SC gaps before reaching the upper part of the model and warming the slab. Consequently, it demonstrates the ability of the slab to accumulate heat in these scenarios. Concerning the CP, graphs from Figures 3.20 and 3.21 do not show significant differences between the different configurations of SC: the slab temperatures are really close and the cooling rates are very similar. However, when the slab is fully covered, it always displays slightly lower temperatures than in the other cases.

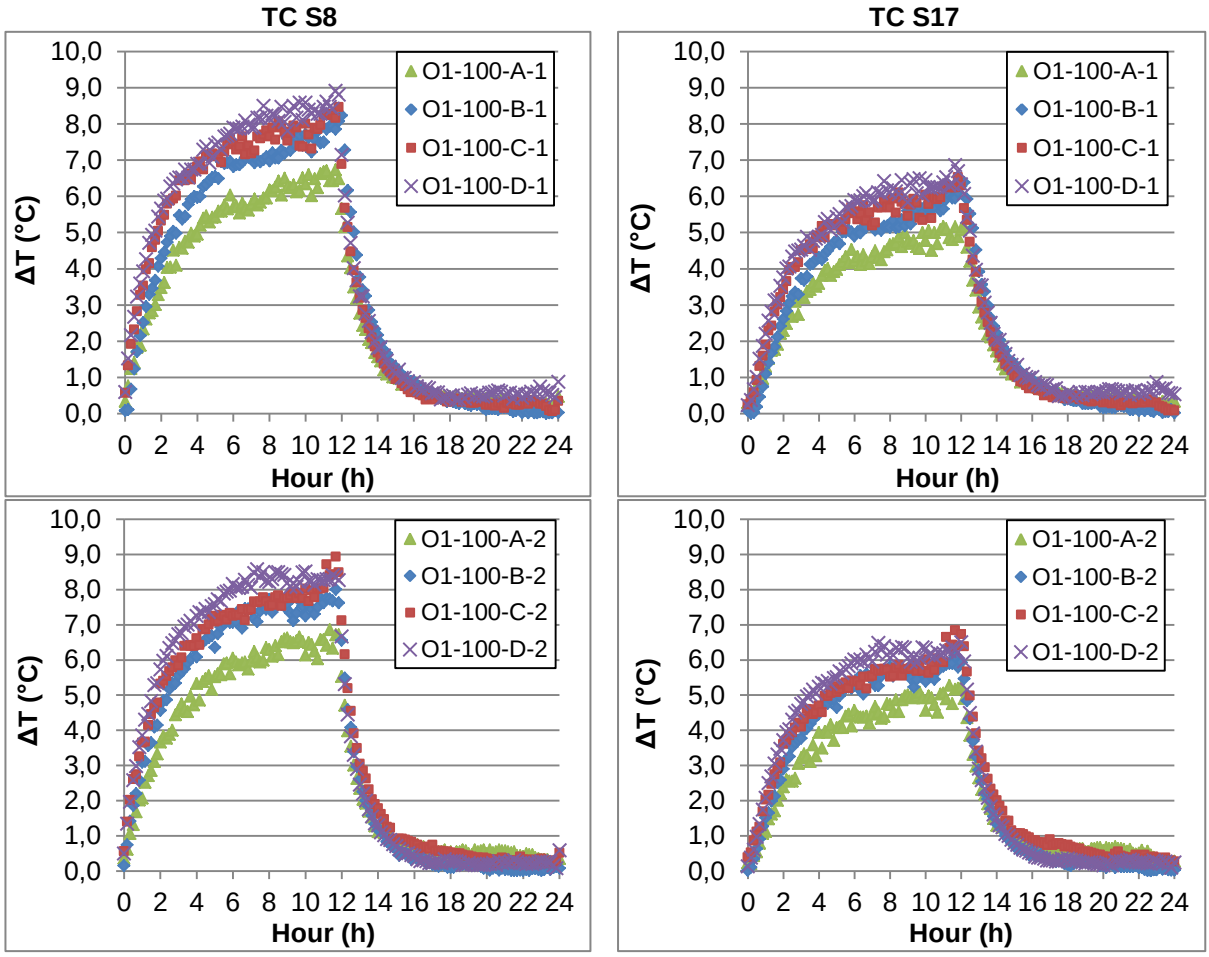

Figure 3.21 - Evolution of the difference between the temperature of the slab and the temperature of the laboratory for two thermocouples located at $x = L_x/2$ and $y = L_y/2$, and placed at the lower surface of the slab (S8) and in its interior (S17), for the tests with $100\ W$.

3.2.1.4. Heat fluxes

To begin with, the graphs in Figure 3.22 reveal that the trend of the heat fluxes curve is the same whatever the type of SC used, and it is the one described in the previous section. In fact, only the values reached during the steady state and the peak at the beginning of the CP are different. Moreover, during the HP, the bigger the gaps between the SC and the walls are, the higher the maximum heat flux in absolute values is reached. For example, for the case O1-100-A-2 (SC with no gap, the electrical resistance is supplied by a power of $100\,W$ and the mean velocity is $2{,}04\,m/s$) the steady state attains $-45\,W/m^2$, whereas higher heat fluxes in absolute value, around $-70\,W/m^2$ and $-80\,W/m^2$, are measured for the cases O1-100-C-2 (with the widest gap) and O1-100-D-2 (without SC) respectively. So, during the HP, the heat flux values obtained by the tests with the SC with gaps and without SC are really close, while the one coming from the test with a full SC are much lower. This is in agreement with the analysis of the temperatures because the larger the gaps are, the higher the heat flux transferred by conduction through the slab, and the higher the slab temperatures during the HP, see Figures 3.20 and 3.21. So, as expected, bigger gaps increase the heat transfer between the occupation zone and the plenum.

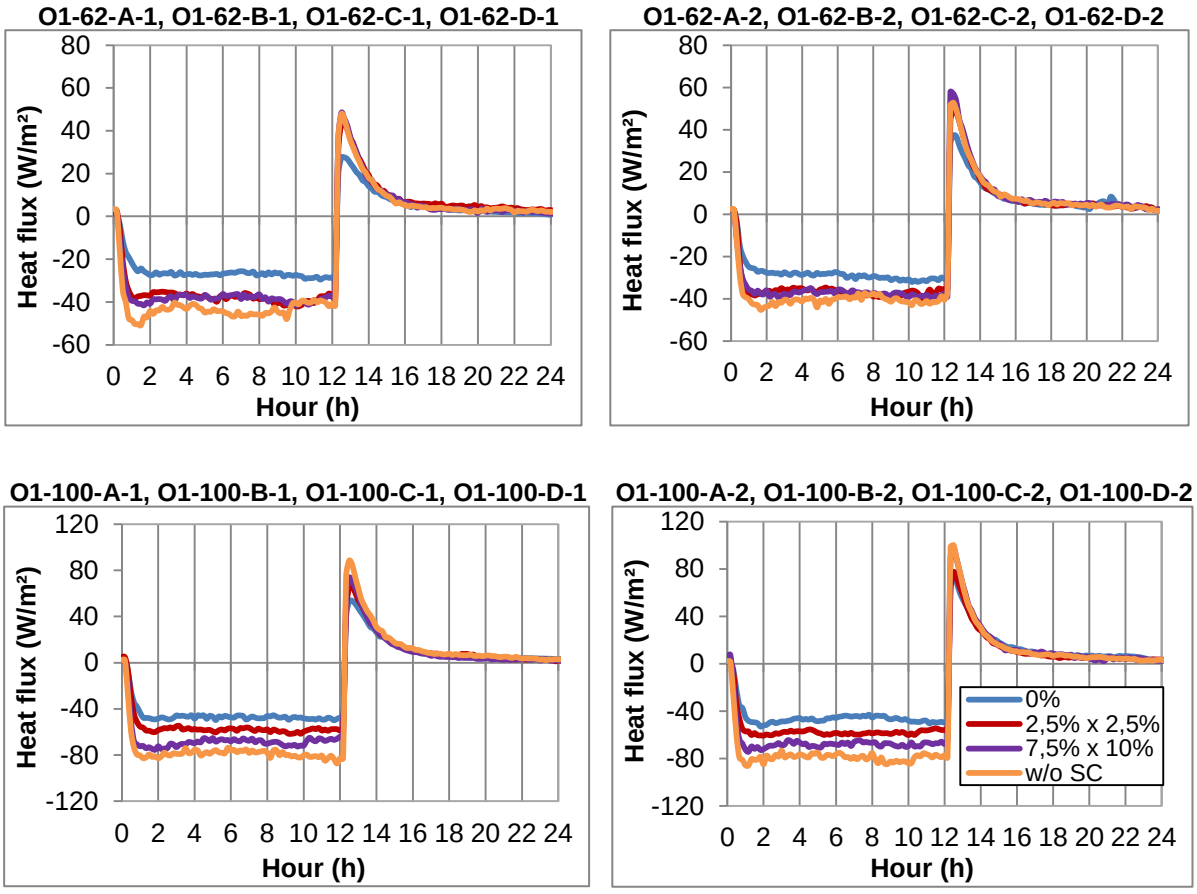

Figure 3.22 - Heat fluxes measured at ($x = 150\,mm, y = L_y/2$) for all test cases.

3.2.2. Influence of the heat load during daytime

In the present thesis, tests were conducted with two different powers supplying the electrical resistance, from 8 a.m. to 8 p.m., which are 62 and $100\,W$. This paragraph points out how the heat load parameter influences the tests.

Comparing values of ΔT from the same TC confirmed that, as anticipated, higher heating power of the electrical resistance yields greater values of ΔT. For example, for the cases without SC and using velocity 1, TC 44 reaches $8°C$ when it is heated by $62\,W$, and $13°C$ for $100\,W$, see Figure 3.16 and Figure 3.17. However, in these figures, the curves have the same tendency for the same SC configuration and different heat load. This corroborates the conclusion made by Lança et al. [37] saying that, despite the quantitative differences, there are no obvious qualitative differences between the plots for different heating powers when the gap of the SC is the same. The exceptions are the cases with the smallest gap since when the heat load is $62W$, TC 44 has similar temperatures to those of TCs 42 and 43, whereas for $100W$ TC 44 has temperatures $2°C$ higher than the others. Those mixed results are probably due to the fact that this gap is known as the transition one.

Observing the values of ΔT from all the TCs in Figure 3.15 and Figure C.1 in Appendix C confirms again that higher temperatures in the enclosure are achieved, as expected, with higher heat loads. As a matter of fact, the maximum temperature achieved in the enclosure after 2 hours of heating changes from $8{,}16$ to $13{,}45°C$ when the heat load increases from 62 to $100\,W$, for the test without SC and using velocity 1.

Similarly, Figures 3.20 and 3.21 show that the slab core heats up more when the heat load is higher since TC S17 reaches $3°C$ in case O1-62-A-1, and $5°C$ in case O1-100-A-1.

In addition, Figure 3.22 shows that the higher the power provided to the electrical resistance is, the higher the heat flux transferred by conduction through the slab. For example, during the HP, the maximum heat flux in absolute value attained in the tests made with $62W$ is $50\,W/m^2$, whereas when the power of $100W$ is used, the heat flux reaches $80\,W/m^2$.

3.2.3. Influence of the air speed during nighttime

During the experiments, two different air speeds generated by the fan are used to cool down the enclosure, from 8 p.m. to 8 a.m. As already mentioned, their mean values are $1{,}1$ and $2{,}04\ m/s$. This section highlights the most important differences and similarities obtained while performing NV with those two air speeds.

First of all, it is possible to observe in Figure 3.15 that, as expected, there are no obvious qualitative differences between the plots for different air speeds when the gap of the SC is the same. In fact, the fan is only turned on during the CP so the air speed does not influence the temperature during the HP. The charts shown in Figure 3.19 are in line with this remark because there are no major differences between the cases using velocities 1 and 2.

However, Figure 3.18 shows that for the cases with the smallest gap of SC and $100W$, TCs placed in the occupation zone display values of ΔT ranging between $3{,}5$ to $5°C$ when velocity 1 is employed, while they extend from $1{,}8$ to $3{,}4°C$ when velocity 2 is used, 30 minutes after the beginning of the cooling phase. A corresponding decrease is also visible in Figure C.2 in Appendix C, below the SC the TCs from test O1-62-B-1 display values of ΔT between $3{,}2$ and $4{,}4°C$ while the ones from O1-62-B-2 show lower values between $1{,}4$ and $2{,}4°C$.

Concerning the tests without SC the difference obtained with the two velocities is smaller or insignificant. Actually, the influence of the air speed is more visible in the cases where there is a gap between the SC and the side walls. In the results from the tests with a complete SC and $100W$, there is an average difference of about $1°C$ in the values of ΔT in the occupation room, between the two velocities. This is surprising because as the opening is located above the SC, a larger difference in the temperatures of the TCs in the plenum was expected.

In general, the analysis of Figures 3.16 and 3.17 shows that with both velocities, and regardless of the other test parameters, all the TCs give values of ΔT below $1°C$ after 4 hours of NV. So, the night cooling strategy is efficient. However, the difference between the duration of time taken by the TCs to reach values close to zero is too small to be significant, when comparing the use of velocity 1 or 2.

Concerning the heat fluxes, Lança et al. [37] measured a heat flux peak of about $120\ W/m^2$ for a heating power of $100\ W$, achieved during the transition between the HP to the CP. However, for the same heating power, the tests result here in lower peaks values of about $75\ W/m^2$ when velocity 1 is employed, and $100\ W/m^2$ for velocity 2. So, it seems that the heat flux peaks increase when the air speed used during the NV increases. This is confirmed by the three tests made with a heating load of $62\ W$, the same SC configuration, and three different velocities, presented in Figure 3.23. The heat flux peak reaches $40{,}4$, $49{,}7$ and $62{,}3\ W/m^2$ when the mean velocity employed is respectively

1,4, 2,1 and $4\,m/s$. So, the higher the velocity of the air passing through the enclosure is, the more efficient the heat transfer from the slab to the interior of the how model. In addition, Figure 3.23 also shows that the results of heat fluxes are consistent for the HP, with about $-40\,W/m^2$ in the cases with a B-type SC for the tests made with $62\,W$, regardless of the air speed used during the CP.

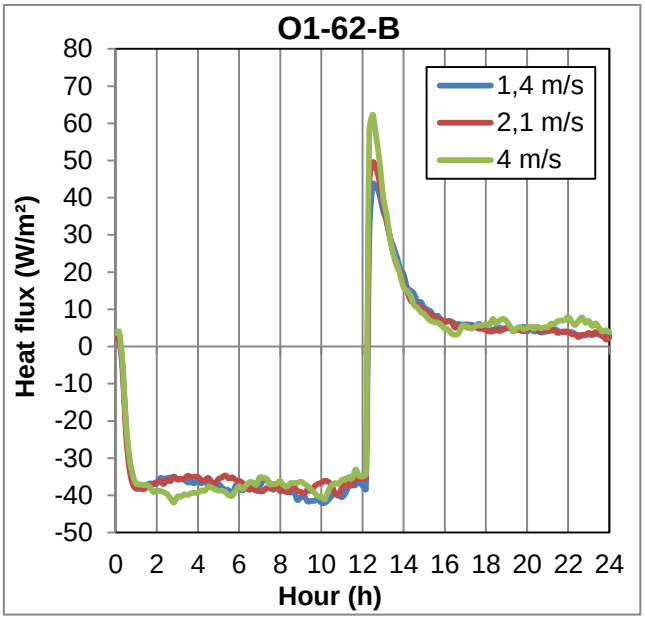

Figure 3.23 - Heat fluxes measured at $(x = 150mm, y = L_y/2)$ for three cases with a heat load of $62\,W$, a gap of 2,5% x 2,5%, and three different velocities.

3.3. Discussion

Now that the results of all the tests have been presented, this section interprets them and explains the physical processes involved.

In general, the tests conducted by Lança et al. [37] correspond to the ones of this thesis carried out with the same parameters. For example, Figure 3.24 shows the heat fluxes measured for all test cases with the air openings above the SC and $100W$ from [37] and from the present work. It can be seen that, comparing each type of SC, the values during the HP are analogous. In both works, the maximum heat flux obtained, during the HP, reaches higher absolute values in experiments without SC, about $80\,W/m^2$, than with a full SC, between 45 and $60\,W/m^2$.

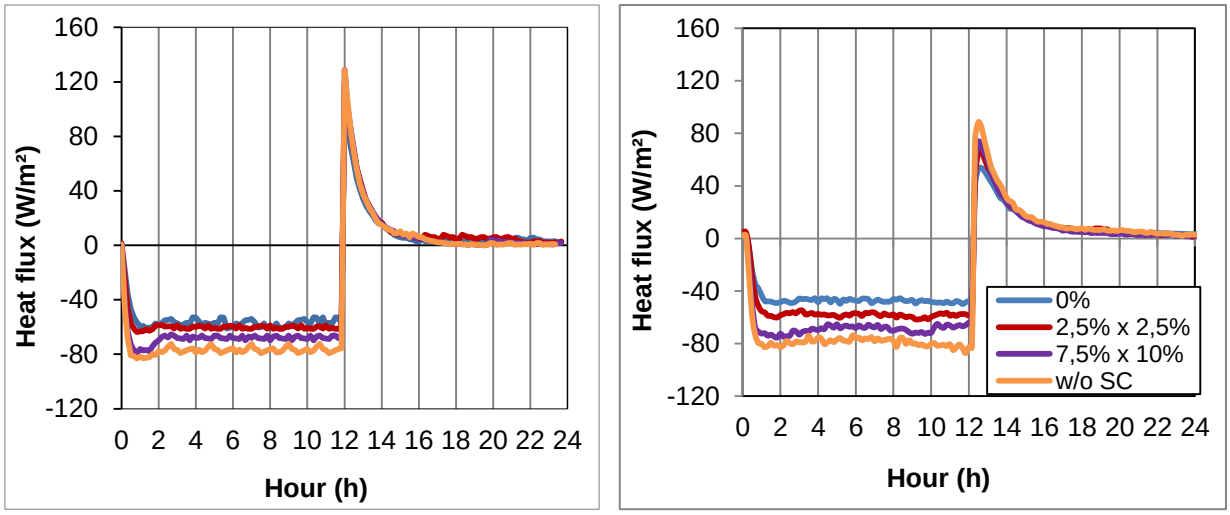

(a) (b)

Figure 3.24 - Heat fluxes measured at ($x = 150mm, y = L_y/2$) for test cases with the air openings above the SC and 100W. (a) Results from Lança et al. [37]. (b) Results from the present work, with velocity 1.

Also, the tool used to evaluate the effectiveness of the night cooling strategy in terms of the influence of the different peripheral gaps gives comparable values for Lança et al. [37] experiments and the ones conducted in this thesis. Indeed, in Figure 3.25 it can be seen that, for both works, the difference between the average temperatures achieved at the end of the heating and cooling periods for TC 64 is about $17°C$ when there is a full SC, and between $11{,}5$ and $14°C$ when the SC is not complete. This is in agreement with the results of Geros et al. [20], because the effectiveness of coupling NV and thermal mass is observed in indoor temperature profiles of the following day, with the attenuation of indoor peak temperatures.

Furthermore, the evolution of the difference between the temperature of the air and the temperature of the laboratory measured by the four same TCs, during experiments made with the same parameters, have very similar results, during the HP, see Figure 3.26. As a matter of fact, TC 64 reaches higher temperatures than the others, around $14°C$, and TC 52 reads the lowest temperatures, around $11°C$, in both works. To a certain extent, the coherence of the analysis of the HP from the present work with the one made in [37] serves to support and confirm the results. Thus, the results obtained for the CP are considered relevant.

Moreover, when one parameter (type of SC, heat load or air velocity) is changed, the data is consistent. For example, in Figure 3.22, the trend of the heat flux curve is the same for all the combination of the parameters. In addition, between the tests with a heat load of $62W$ and those with $100W$ there are only quantitative differences but no qualitative differences, when the gap of the SC is the same, see Figures 3.20 and 3.21. In the latter figures, results obtained with velocities 1 and 2 are also similar. For those reasons, it is possible to say that the results are reliable.

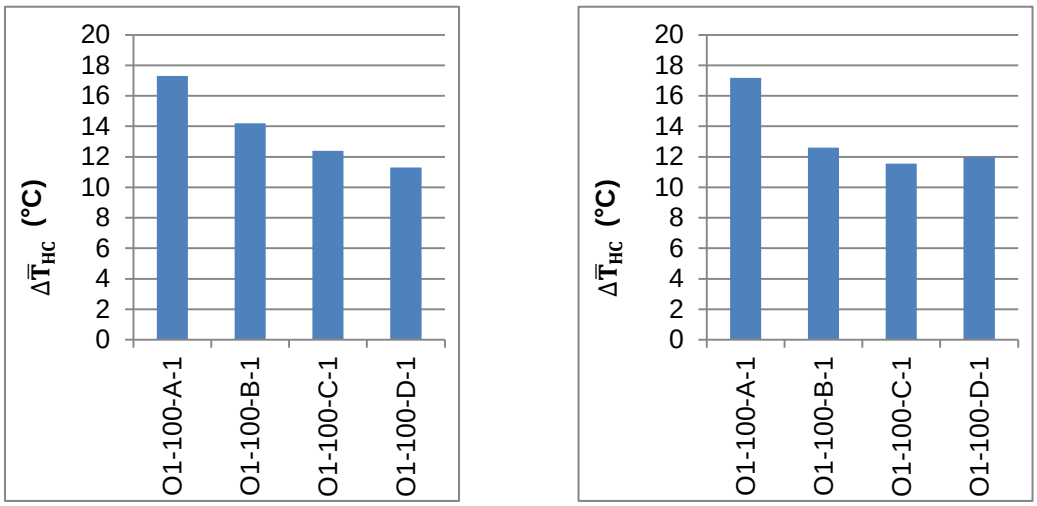

(a) (b)

Figure 3.25 - Difference between the average temperatures achieved at the end of the heating and cooling periods for thermocouple n°64 and for cases with openings above the SC with $100W$. (a) Results from Lança et al. [37]. (b) Results from the present work, with velocity 1.

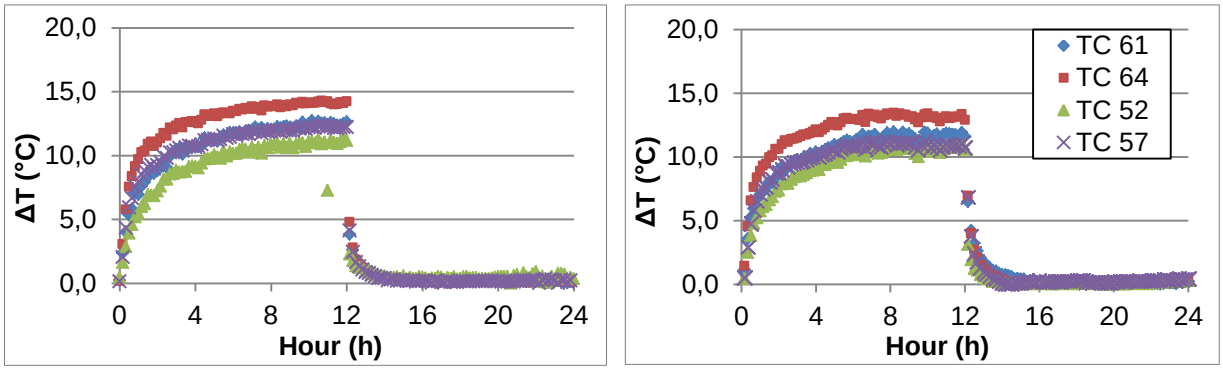

(a) (b)

Figure 3.26 - Evolution of the difference between the temperature of the air and the temperature of the laboratory measured by four thermocouples for one experiment with the openings above the SC, a heat load of $100W$, and a SC with 2,5% x 2,5% gaps. (a) Results from Lança et al. [37]. (b) Results from this thesis with velocity 2.

Concerning the HP, the thermal plume is originated by the electrical resistance and entrains air around it. Then, it takes this warm air to the plenum, and diffuses it along the slab. Inside the plume, the temperature of the air decreases with the increasing of the height. The contrast between the use of the different SC configurations is that the complete SC induces a thermal stratification in the occupation zone only, while the SCs with gaps allow the warm air to pass through it, and lead to the stack effect in the reduced scale model. Consequently, the same observation as that of Lança et al. [37] is made: the peripheral gap of the SC allows the heat generated in the occupation zone to be partially used to heat up the plenum and the slab. Indeed, Figure 3.20 shows that the temperatures of the slab in the HP are higher when a gap is present (O1-100-B-1 and O1-100-C-1) than in the case of a complete SC (O1-100-A-1 and 2). As a result of the previous observation, the air

temperature in the occupation zone during the HP is lower when the SC presents a peripheral gap with the side walls. This trend is visible in Figures 3.16 and 3.17, which show that the temperatures below the SC in cases O1-100-A-1 and O1-100-A-2, as well as in the cases O1-62-A-1 and O1-62-A2, are consistently higher than in the other cases. The precedent observation is in line with the work of Domínguez et al. [30] because it was found that the smaller the gaps are, i.e., the bigger the CCR (Ceiling Coverage Ratio) is, the lower the convective heat exchange between the occupation zone and the plenum is. This is identified as a cause in the reduction of the cooling performance.

During the initial period of the CP, the air temperature above the SC is higher when there is no gap or there is a small gap, than when there is no SC. This is demonstrated in Figure 3.18, which shows that even though the air openings are placed above the SC, the cooling process is more efficient and homogenized when the SC has a peripheral gap. The incoming air flow passes through it and reaches all the zones of the room more easily.

In addition, in all the tested configurations, the columns n°2 and 5 always cool faster in the plenum than in the occupation zone for all the tests, and among the TCs attached to the lower surface of the slab, the temperatures of the ones situated at $y = L_y/2$ decrease faster than the ones that are not located in the middle of the reduced scale model. This means that the flow field of the incoming cool air is really concentrated in the upper centered part of the enclosure, even in the absence of SC.

Even though the difference between the tests conducted in this thesis using the different two velocities are not very important, the comparison with the results from Lança et al. [37], where higher air speeds were employed, show that higher velocities increase the convective heat exchange with the slab. In fact, more stored heat is transmitted from the slab to the enclosure, as evidenced by the higher heat flux retrieved in the experiments of Lança et al. [37], just after the start of the operation of the fan, in Figure 3.24. In other words, higher heat transfer coefficients are found during the CP because forced convection occurs with higher air speed. Consequently, this NV technique takes advantage of the thermal inertia of the slab.

Moreover, it can be acknowledged that the NV strategy is efficient in all of the sixteen cases because at the end of the CP the ΔT values of the air temperatures, the slab temperatures and the heat flux values are close to $0\ °C$ or W/m^2. This means that the enclosure has the same temperature as the outside air. So, the thermal mass, which buffered the heat released in the model during the day, released all of it during the night.

4. Conclusions and Future Work

4.1. Conclusions

The goal of this experimental study was to confirm previous results obtained during the HP originated by a flow driven by buoyancy forces and to investigate the CP caused by building ventilation driven by mechanical forces. The ultimate purpose was to evaluate the effectiveness of the NV coupled with thermal mass, using four design scenarios for the SC, in a reduced scale model of an office, with the aim of improving thermal comfort. In addition to evaluating the influence of the peripheral gap between the SC and the side walls, the effect of two other parameters, which are the heat load and the air speed, were examined through the results of the sixteen different test cases carried out.

Comparisons were made between the experimental results obtained by Lança et al. [37] and the ones of the present work, for the HP of 12 hours. Analyzing the results from both works, for the same test configurations, there are no significant qualitative nor quantitative differences in terms of heat fluxes and temperatures. Indeed, the curves have the same trends and reach the same values. Because the results for the HP in the present work are coherent with the ones from Lança et al. [37], then the outcomes for the CP are considered reliable.

The efficiency of night cooling was tested. It was found that the slab core temperature drops by $6{,}5°C$ in only 6 hours of night cooling operation, for the case with the larger peripheral gap, the higher heat load, and the lower air velocity. This demonstrates how this technique is effective. Moreover, NV depends directly on heat load released by the electrical resistance during daytime, the air flow rate during the nighttime, and the size of the peripheral gaps. The results indicate that the smaller the gaps are, the lower the convective heat exchange between the occupation zone and the plenum is. This is identified as a cause in the reduction of the cooling performance. As a result of the previous observation, wider gaps between the SC and the walls contribute to involve the slab in the passive technique of cooling. The effectiveness of coupling NV and thermal mass is observed in indoor temperature profiles of the following day, with the attenuation of indoor peak temperatures.

It was also found that the areas closer to the supply and exhaust air openings cool down faster than the others in all the tested configurations. Consequently, even when there is no SC, the air flow is largely concentrated in the upper centered part of the reduced scale model, with higher velocities. However, it has been found that SCs with peripheral gaps induce a more homogeneous cooling than the complete SC. Indeed, gaps between the SC and the side walls allow the air flow to reach all the zones of the reduced scale model.

To sum up, this thesis succeeded in better understanding the heating of the slab and the thermal plume characteristics during the HP, but also in apprehending the air flow fields during the CP.

As a consequence of all the previous conclusions, this work corroborates that the NV technique is a solution to reduce the energy consumption of buildings, and more precisely the energy requirements of HVAC systems, while maintaining an acceptable indoor environment. Moreover, modern office buildings can be designed to be ventilated more efficiently with architectural elements, such as a SC with peripheral gaps. Indeed, it allows mixing between the air below and above it and so enhances the cooling capacity.

4.2. Future Work

The results obtained in this thesis can be a base for future developments. Some topics that could give continuation to this work are:

- Conduct experiences with a SC with peripheral gaps smaller than the smallest one used for the present thesis and with even bigger gaps to find the ones that induce a different behavior.
- Carry out experiments with lower velocities.
- In the present work, only one localized point heat source exists. Nevertheless, in a real ventilated office building there may have more heat sources with various heat loads, shapes and areas. Therefore, tests should be conducted with different heat sources.
- Experiments on real scale structures should be made to confirm the ventilation performance found with the reduced scale model. For example, it would be important to verify if the heat flux and the slab temperatures would also be negligible at the end of the CP in a full scale compartment. However, this can be time consuming and difficult to modify the parameters. Therefore, it is often desirable to use CFD or a reduced scale model.
- Further work is needed to evaluate accurately the pattern of the airflow during the cooling phase. For example, anemometers can be added in the occupation zone to measure the air velocity and better understand this phenomenon.

5. References

[1] L. Pérez-Lombard, J. Ortiz, and C. Pout, “A review on buildings energy consumption information”, *Energy and Buildings*, 40(3), 394–398, 2008.

[2] M. Kolokotroni and A. Aronis, “Cooling-energy reduction in air-conditioned office by using night ventilation”, *Appl. Energy*, 63, 241–253, 1999.

[3] Adene, Agência para a Energia, “Energy Efficiency trends and policies in Portugal”, National Report for the ODYSSEE-MURE Project Planning and Studies Department, 2016, Retrieved from http://www.odyssee-mure.eu/publications/national-reports/energy-efficiency-portugal.pdf, Accessed date: March 13th, 2019.

[4] U.S. Energy Information Administration, “2012 Commercial Buildings Energy Consumption Survey: Energy Usage Summary”, 2016, Retrieved from https://www.eia.gov/consumption/commercial/reports/2012/energyusage/, Accessed date: March 15th, 2019.

[5] P. Guo, S. Wang, B. Xu, Q. Men, and Y. Wang, “Reduced-scale experimental model and numerical investigations to buoyance-driven natural ventilation in a large space building”, *Building and Environment*, 145, 24–32, 2018.

[6] E. Solgi, Z. Hamedani, R. Fernando, H. Skate, and N. E. Orji, “A literature review of night ventilation strategies in buildings”, *Energy and Buildings*, 173, 337–352, 2018.

[7] Y. Al Horr, M. Arif, A. Kaushik, A. Mazroei, M. Katafygiotou, and E. Elsarrag, “Occupant productivity and office indoor environment quality: A review of the literature”, *Building and Environment*, 105, 369–389, 2016.

[8] Z. Zhai, , H. Mankibi, M. El, and Stathopoulos, N. “Review of natural ventilation models”, *Energy Procedia,* 78, 2700 – 2705, 2015.

[9] H. Breesch and A. Janssens, “Reliable Design of Natural Night Ventilation Using Building Simulation”, *Ashrae Journal*, *10th Thermal Performance of the Exterior Envelopes of Whole Buildings Conference,* 1–14, 2007.

[10] L. Zhigang, “Characteristics of Buoyancy Driven Natural Ventilation through Horizontal Openings”, *PhD Thesis*, Aalborg University, Denmark, 2007.

[11] W. J. Fisk, D. Black and G. Brunner, “Changing ventilation rates in U.S. offices: Implications for health, work performance, energy, and associated economics”, *Building and Environment*, 47(1), 368–372, 2012.

[12] P. Blondeau, M. Spérandio, and F. Allard, “Night ventilation for building cooling in summer”, *Solar Energy*, 61(5), 327–335, 1997.

[13] P.F. Linden, “The Fluid Mechanics of Natural Ventilation”, *Annual Review of Fluid Mechanics*, 31(1), 201–238, 1999.

[14] S. Leenknegt, R. Wagemakers, W. Bosschaerts, and D. Saelens, “Numerical sensitivity study of transient surface convection during night cooling”, *Energy & Buildings*, 53, 85–95, 2012.

[15] Q. Chen, “Ventilation performance prediction for buildings: A method overview and recent applications”, *Building and Environment*, 44(4), 848–858, 2009.

[16] C. Walker, G. Tan, L. Glicksman, “Reduced-scale building model and numerical investigations to buoyancy-driven natural ventilation”, *Energy and Buildings*, 43(9), 2404–2413, 2011.

[17] D. Etheridge, M. Sandberg, “Building Ventilation: Theory and Measurement”, *John Wiley & Sons Ltd.*, England, 607-626, 1996.

[18] R. Li, A. Pitts, and Y. Li, “Buoyancy-driven natural ventilation of a room with large openings”, *Proceedings: Building Simulation*, 984–991, 2007.

[19] K. Imessad, L. Derradji, N.Ait Messaoudene, F. Mokhtari, A. Chenak, R. Kharchi, “Impact of passive cooling techniques on energy demand for residential buildings in a Mediterranean climate” *Renewable Energy*, 71, 589–597, 2014.

[20] V. Geros, M. Santamouris, A. Tsangrasoulis, and G. Guarracino, “Experimental evaluation of night ventilation phenomena”, *Energy and Buildings*, *29*, 141–154, 2002.

[21] E. Shaviv, A. Yezioro, I. G. Capeluto, “Thermal mass and night ventilation as passive cooling design strategy”, *Renewable Energy*, 24, 445–452, 2001.

[22] N. Artmann, H. Manz, and P. Heiselberg, “Parameter study on performance of building cooling by night-time ventilation”, *Renewable Energy*, 33, 2589–2598, 2008.

[23] S. A. Kalogirou, G. Florides, and S. Tassou, “Energy analysis of buildings employing thermal mass in Cyprus”, *Renewable Energy*, 27, 353–368, 2002.
[24] J. Landsman, G. Brager, and M. Doctor-Pingel, “Performance, prediction, optimization, and user behavior of night ventilation”, *Energy and Buildings*, 166, 60–72, 2018.

[25] R. de dear, G. S Brager, “Developing an adaptive model of thermal comfort and preference”, *UC Berkeley: Center for the Built Environment*, 1998, Retrieved from https://escholarship.org/uc/item/4qq2p9c6, Accessed date: April 4th, 2019.

[26] M. J. Ren and J. A. Wright, “A Ventilated Slab Thermal Storage System Model, *Building and Environment*, 33(1), 43–52, 1998.

[27] C. Jimenez-Bescos, “An evaluation on the effect of night ventilation on thermal mass to reduce overheating in future climate scenarios”, *Energy Procedia*, 122, 1045–1050, 2017.

[28] J. Pfafferott, S. Herkel, and M. Wambsganß, “Design, monitoring and evaluation of a low energy office building with passive cooling by night ventilation”, *Energy and Buildings*, 36, 455–465, 2004.

[29] R. Høseggen, H. M. Mathisen, and S. O. Hanssen, “The effect of suspended ceilings on energy performance and thermal comfort”. *Energy and Buildings*, 41, 234–245, 2009.

[30] L. Domínguez, O. Kazanci, N. Rage and B. Olesen, “Experimental and numerical study of the effects of acoustic sound absorbers on the cooling performance of Thermally Active Building Systems”, *Building and Environment*, 116, 108–120, 2017.

[31] K. Jantana and J. Pukdum, “Experimental investigation on heat gain reduction using a vinyl perforated ceiling”, *Energy Procedia*, 138, 586–591, 2017.

[32] W. Wu, N. Yoon, Z. Tong, Y. Chen, Y. Lv, T. Ærenlund, and J. Benner, “Diffuse ceiling ventilation for buildings: A review of fundamental theories and research methodologies”, *Journal of Cleaner Production*, 211, 1600–1619, 2019.

[33] C. A. Hviid and S. Svendsen, “Experimental study of perforated suspended ceilings as diffuse ventilation air inlets”, *Energy and Buildings*, 56, 160–168, 2013.

[34] M. Koschenz and B. Lehmann, “Development of a thermally activated ceiling panel with PCM for application in lightweight and retrofitted buildings”, *Energy and Buildings*, 36, 567–578, 2004.

[35] J.-W. Jeong and S. A. Mumma, “Practical cooling capacity estimation model for a suspended metal ceiling radiant cooling panel”, *Building and Environment*, 42, 3176–3185, 2007.

[36] H. Weinläder, W. Körner and B. Strieder, “A ventilated cooling ceiling with integrated latent heat storage - Monitoring results”, *Energy and Buildings*, 82, 65–72, 2014.

[37] M. Lança, P. J. Coelho and J. Viegas, "Enhancement of heat transfer in office buildings during night cooling − reduced scale experimentation", *Building and Environment*, 148, 653-667, 2018.

[38] K. Noto, K. Teamoto and T. Nakajima, "Spectra and critical Grashof numbers for turbulent transition in a thermal plume”, J. Thermophys. *Heat Tran.,* 13, 82–90, 1999.

[39] P.E. Dimotakis, "The mixing transition in turbulent flows", *Journal of Fluid Mechanics*, 409, 69–98, 2000.

[40] N. Artmann, R. Vonbank and R. Jensen, "Temperature Measurements Using Type K Thermocouples and the Fluke Helios Plus 2287A Data Logger", *DCE Technical Report* No. 052, Aalborg University, Denmark, 2008.

[41] ISO-JCGM 100:2008, “Evaluation of measurement data - Guide to the expression of uncertainty in measurement”, Joint Committee for Guides in Metrology of the International Bureau of Weights and Measures*, International Organization for Standardization Geneva ISBN*, *50*, 134, 2008, Retrieved from https://doi.org/10.1373/clinchem.2003.030528, Accessed date: March 11th, 2019.

6. Appendix

A. Appendix A

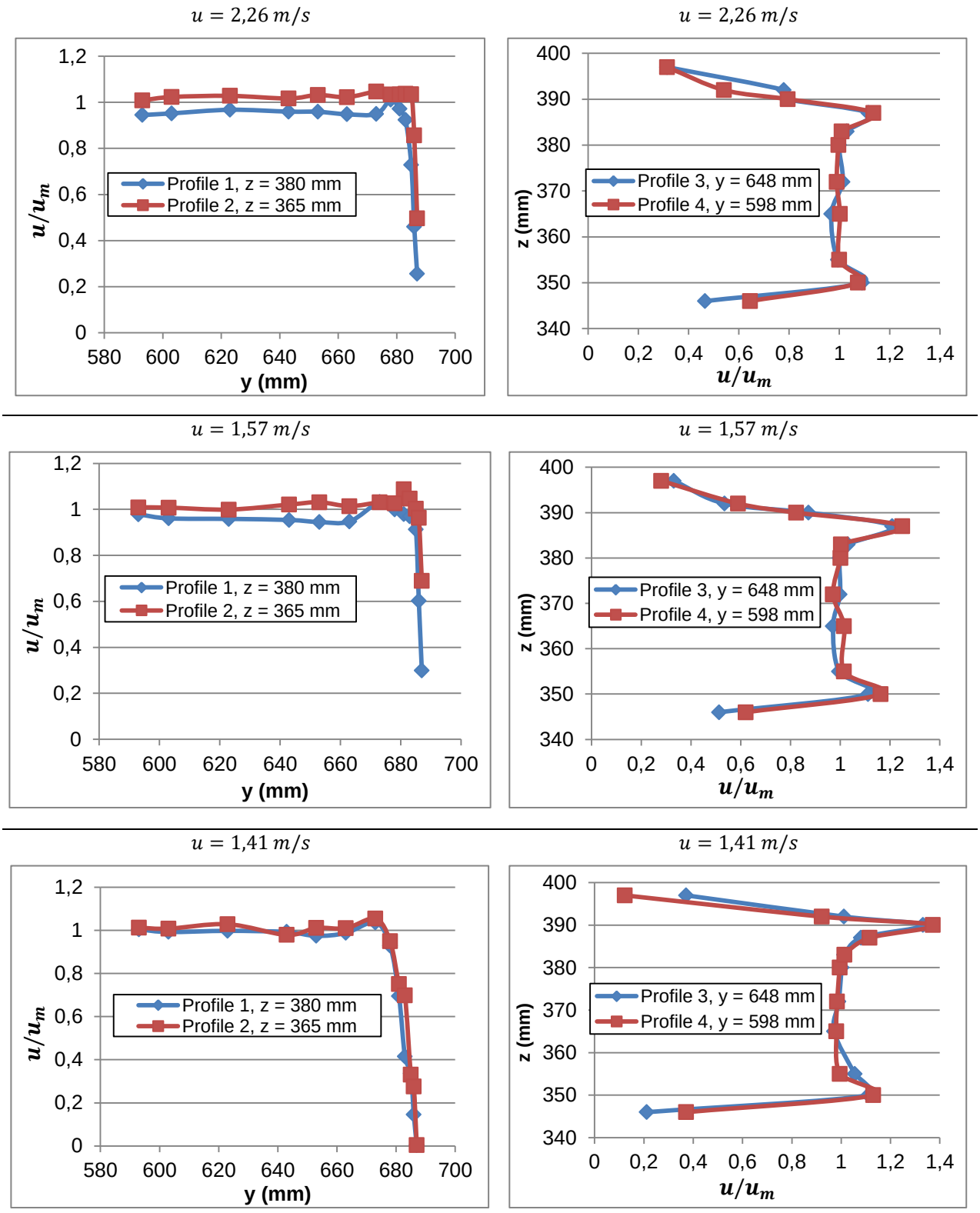

Figure A.1 - Measured nondimensional velocity profiles at the extraction slot for three requested velocities.

B. Appendix B

Table B.1 - Calibration certificates of the instrumentation used in this thesis.

Certificate number	Institute	Calibrated equipment	Date
0445/2017-UMA	UMA / LNEC – EM[2]	Hot wire anemometer with digital indicator Airflow; TA5	04/10/2017
395/2019-UMA	LNEC Testing and Metrology / Applied Metrology Laboratory	T type thermocouple	12/06/2019
396/2019-UMA			
397/2019-UMA			
398/2019-UMA			
399/2019-UMA			
400/2019-UMA			
401/2019-UMA			
402/2019-UMA			
403/2019-UMA			
404/2019-UMA			
405/2019-UMA			
406/2019-UMA			
407/2019-UMA			
408/2019-UMA			
409/2019-UMA			
410/2019-UMA			
411/2019-UMA			
412/2019-UMA			
413/2019-UMA			
414/2019-UMA			
415/2019-UMA			
416/2019-UMA			
417/2019-UMA			
418/2019-UMA			
419/2019-UMA			
420/2019-UMA			
421/2019-UMA			
422/2019-UMA			
423/2019-UMA			
424/2019-UMA			
425/2019-UMA			
426/2019-UMA			

[2] EM: Ensaios e Metrologia
UMA: Unidade de Metrologia Aplicada

Certificate number	Institute	Calibrated equipment	Date
427/2019-UMA	LNEC Testing and Metrology / Applied Metrology Laboratory	T type thermocouple	12/06/2019
428/2019-UMA			
429/2019-UMA			
430/2019-UMA			
431/2019-UMA			
432/2019-UMA			
433/2019-UMA			
434/2019-UMA			
435/2019-UMA			
436/2019-UMA			
437/2019-UMA			
438/2019-UMA			
439/2019-UMA			
440/2019-UMA			
441/2019-UMA			
442/2019-UMA			
443/2019-UMA			
444/2019-UMA			
445/2019-UMA			
446/2019-UMA			
447/2019-UMA			
448/2019-UMA			
449/2019-UMA			
450/2019-UMA			
451/2019-UMA			
452/2019-UMA			
453/2019-UMA			
454/2019-UMA			
455/2019-UMA			
576/2019-UMA			
458/2019-UMA			
459/2019-UMA			
460/2019-UMA			
461/2019-UMA			
462/2019-UMA			
463/2019-UMA			
464/2019-UMA			
465/2019-UMA			
466/2019-UMA			
467/2019-UMA			

C. Appendix C

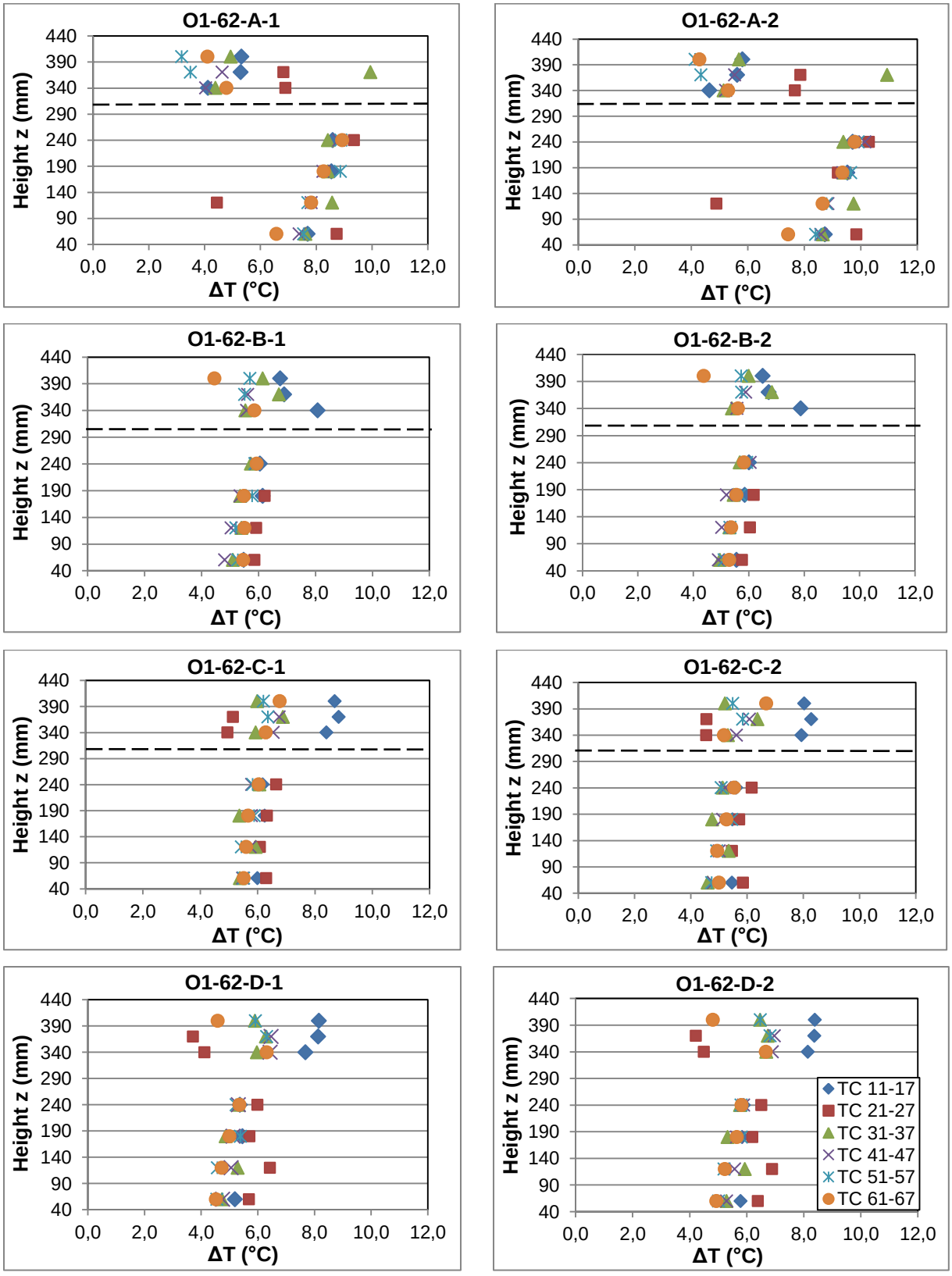

Figure C.1 - Difference between the temperature of the air and the temperature of the laboratory from all the experiments with 62W, data retrieved the second day, 2 hours after the electrical resistance is switched on. The horizontal dashed line indicates the position of the SC.

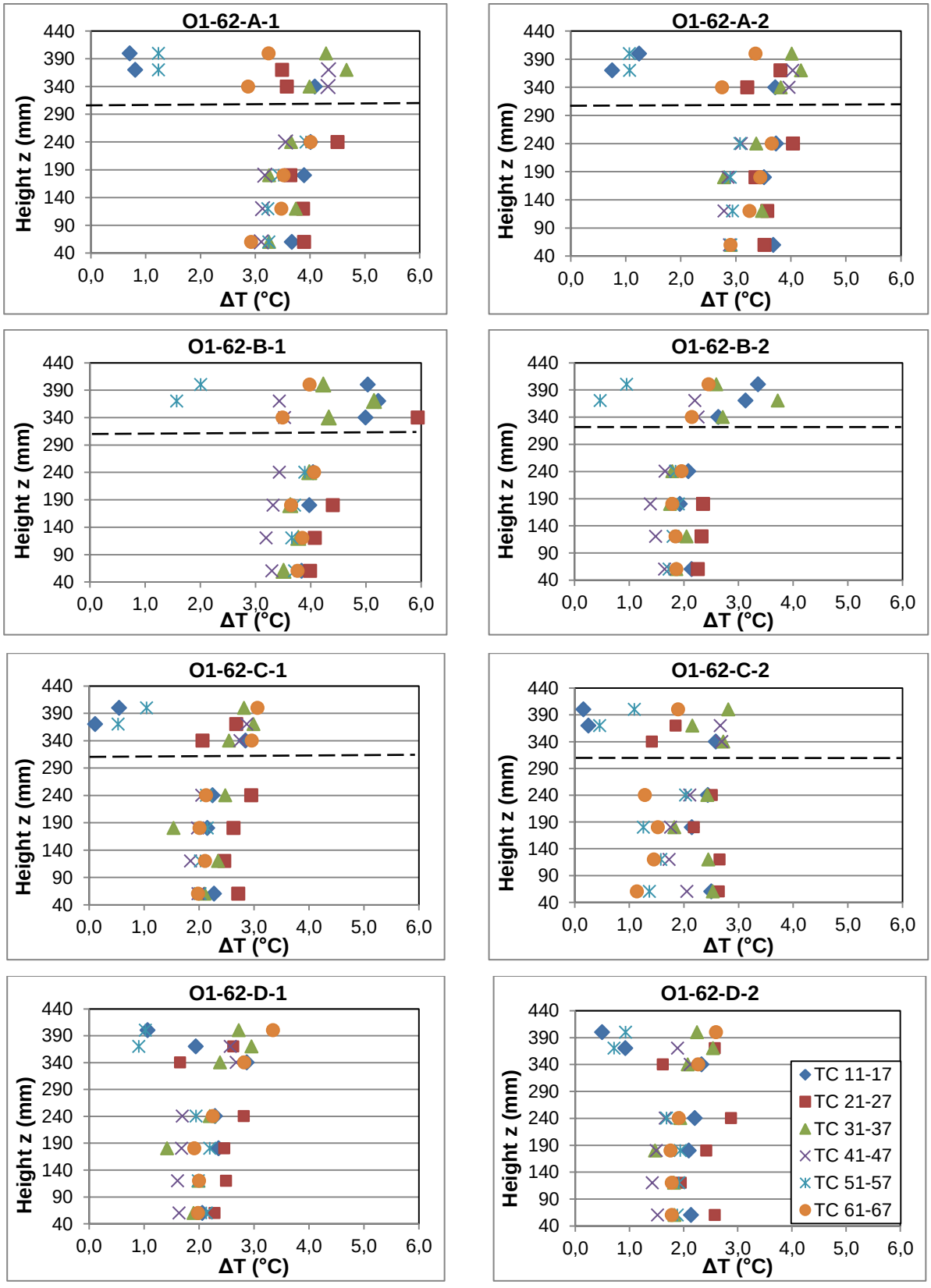

Figure C.2 - Difference between the temperature of the air and the temperature of the laboratory at 30 minutes after the beginning of the CP for all the TCs of all the tests with 62 W. The horizontal dashed line indicates the position of the SC.